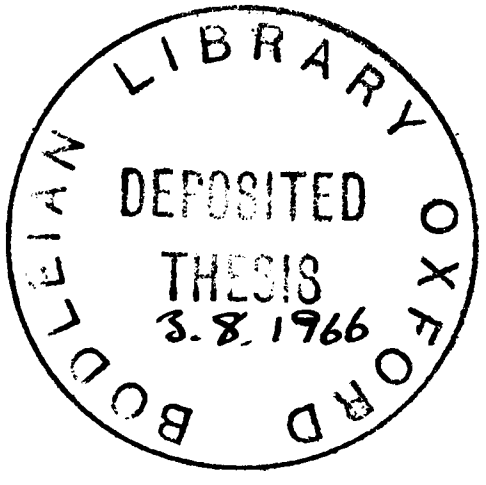
COLLECTIVE PROPERTIES OF MEDIUM WEIGHT NUCLEI

J. J. Simpson

A thesis submitted for the Degree of

Doctor of Philosophy in the University of Oxford.



Merton College,

Oxford.

January 1966.

C O N T E N T S

	Page
Acknowledgements	
Abstract	1
CHAPTER 1. INTRODUCTION	1
CHAPTER 2. THEORY	6
2.1. Coulomb Excitation Theory	6
2.1. 1. Criteria for Semi-Classical Approximation	6
2.1. 2. Electric Interaction	8
2.1. 3. Excitation Cross-Sections	9
2.1. 4. Symmetrization of Cross-Sections	12
2.1. 5. Projectile Energy Restrictions	14
2.1. 6. Angular Distribution of Gamma Rays	16
2.1. 7. Experimental Excitation Probability	17
2.1. 8. Multiple Excitation; Second Order Perturbation Theory	18
2.1. 9. The "Reorientation" Effect	20
2.1.10. Virtual El Excitation of Giant Dipole Resonance	22
2.1.11. Multiple Excitation; Schrodinger Equation Method	23
2.2. Nuclear Theories	26
2.2. 1. Phenomenological Models	26

Page

2.2. 2. Microscopic Models 27

2.2. 3. Treatment of Pairing Forces 28

2.2. 4. Collective Motion 32

2.2. 5. Quadrupole-Quadrupole Force 33

2.2. 6. Numerical Calculations 35

2.2. 7. Quasi-Particle Interactions 37

CHAPTER 3. EXPERIMENTAL METHODS 40

3.1. Ti^{50}, Cr^{52}, Fe^{54} 40

3.1. 1. Beam Energy 40

3.1. 2. Targets 41

3.1. 3. Magnetic Spectrograph 43

3.1. 4. The Experiment 45

3.1. 5. Transfer Reactions 51

3.2. $Ce^{140,142}$, $Nd^{142-148}$, $Sm^{144,148,150}$, Nd^{143}. 51

3.2. 1. Oxygen Beams 52

3.2. 2. Targets 52

3.2. 3. Detectors 53

3.2. 4. The Experiment 53

3.3. The "Reorientation" Effect; Cd^{114}, Sm^{148}, Sm^{150} 57

3.3. 1. Sulphur Beams 58

3.3. 2. Targets 60

		Page
	3.3. 3. Detectors	62
	3.3. 4. The Experiment	62
CHAPTER 4.	EXPERIMENTAL RESULTS	64
4.1.	Ti^{50}, Cr^{52} and Fe^{54}	64
	4.1. 1. Experimental Probabilities	64
	4.1. 2. Charge State Correction	67
	4.1. 3. Calculated Probabilities	69
4.2.	$Ce^{140,142}$, $Nd^{142-148}$, $Sm^{144,148,150}$, Nd^{143}.	72
	4.2. 1. Experimental Probabilities	72
	4.2. 2. Determination of the Photopeak	73
	4.2. 3. Absorption Correction	74
	4.2. 4. Efficiency Correction	76
	4.2. 5. Angular Distribution of Gamma Rays	76
	4.2. 6. Calculated Probabilities	80
	4.2. 7. Results	81
4.3.	"Reorientation Effect" Cd^{114}, Sm^{148}, Sm^{150}	83
	4.3. 1. Experimental Probabilities	83
	4.3. 2. Cadmium Target	86
	4.3. 3. Experimental Results	86
	4.3. 4. Calculated Probabilities	88
	4.3. 5. Quadrupole Moments; Perturbation Theory	90

Page

4.3. 6. Quadrupole Moments; Schrodinger Equation Solution 91

CHAPTER 5. DISCUSSION OF RESULTS 97

5.1. Electric Quadrupole Transition Strengths 98

5.1. 1. Final B(E2) Values 98

5.1. 2. Pairing Force Calculations 103

5.1. 3. B(E2) Value of Nd^{143} 108

5.1. 4. Systematics of B(E2) Values 108

5.1. 5. Summary 110

5.1. 6. The Nuclear Radius Parameter 111

5.1. 7. Inelastic Scattering above Coulomb Barrier 112

5.2 Electric Quadrupole Moments of Excited States 112

5.2. 1. Quadrupole Moments; Cd^{114}, Sm^{148}, Sm^{150} 114

5.2. 2. The Asymmetric Rotor Model 118

5.2. 3. Modified Phonon Model 121

5.3 Conclusions 125

References 129

ACKNOWLEDGEMENTS

Many people have assisted me throughout the course of this work. I should particularly like to thank Dr. D. Eccleshall of the Atomic Weapons Research Establishment, Aldermaston for his guidance and encouragement. My thanks are also extended to my supervisor Dr. N.W. Tanner for many stimulating discussions.

I am grateful to Professor D.H. Wilkinson, F.R.S. for extending the facilities of the Nuclear Physics Laboratory, Oxford, and to Professor K.W. Allen and Dr. H.E. Hulme for the research facilities of the Superintendency of Nuclear Research at Aldermaston.

I should like to thank Mr. M.J.L. Yates for much assistance throughout this work; Dr. J.A. Cookson for help in the magnetic analysis experiments; and Dr. N.J. Freeman for the production of the mass-separated targets. I am indebted to Dr. A.C. Douglas for theoretical computations of the reorientation effect.

I should also like to thank the experimental and technical staff at Aldermaston for much willing help; in particular Mr. M.A. Brown, Mr. P.J. Nind, Mr. S. Waller, Mrs. J. Redding, and Mr. D. Akers and Mr. R. Bell and the

operations staff of the tandem generator for efficient operation and much persistence in obtaining sulphur ions. I am grateful to Mrs. E. Browne for patiently typing this thesis.

Finally, I wish to thank the Royal Commission for the Exhibition of 1851 for a scholarship.

ABSTRACT

A study has been made of collective quadrupole phenomena in some medium weight nuclei. The nuclei studied are ones which are not understandable in terms of rotations of a symmetrically deformed nucleus.

Two types of electric quadrupole phenomena have been determined, the electric quadrupole transition strength between the ground state and first excited state and the electric quadrupole moment of the first excited 2^+ state in even nuclei.

The method of Coulomb excitation, employing oxygen beams up to 45 MeV and sulphur beams up to 55 MeV from a tandem Van de Graaff generator, has been used, and the Coulomb excitation cross-section has been determined in two ways. One method was the magnetic analysis of the scattered oxygen ions from the target with a consequent determination of the excitation probability directly from the number of inelastic ions detected; the other method was the measurement of the number of deexcitation gamma rays in coincidence with the heavy ions detected at backward angles near 180°.

The electric quadrupole transition strengths have been determined in a few single-closed shell nuclei and some of

their isotopic neighbours. The upward reduced transition strengths, B(E2), for the ground to first excited state transition, in units of e^2b^2, are as follows : Ti^{50}, 0.024 ± 0.002; Cr^{52}, 0.048 ± 0.002; Fe^{54}, 0.051 ± 0.002; Ce^{140}, 0.27 ± 0.04; Ce^{142}, 0.42 ± 0.01; Nd^{142}, 0.42 ± 0.05; Nd^{143}, 0.047 ± 0.013; Nd^{144}, 0.44 ± 0.02; Nd^{146}, 0.65 ± 0.01; Nd^{148}, 0.96 ± 0.02; Sm^{144}, 0.25 ± 0.04; Sm^{148}, 0.79 ± 0.02; Sm^{150}, 1.34 ± 0.06. The errors quoted on the Ce, Nd and Sm nuclei are relative errors and a 10% error should be added in quadrature to them to get absolute errors. A comparison of the B(E2) values with a pairing plus quadrupole force theory shows that the theory is quite successful for the single-closed shell nuclei, but for nuclei with only a few particles outside the closed shell, the theory grossly overestimates the transition strengths.

The electric quadrupole moment of the first 2^+ state in Cd^{114}, in Sm^{148} and in Sm^{150} has been deduced using the reorientation effect of Coulomb excitation. The excited state quadrupole moment determined is for Cd^{114}, -0.39 ± 0.24 b; for Sm^{148}, -0.78 ± 0.38 b and for Sm^{150}, -1.26 ± 0.23 b. These values are all substantially larger than the quadrupole moment due to a single proton thus emphasizing the collective nature of the low-lying states. The moments

for Sm^{148} and Sm^{150} are of the magnitude expected for a fully deformed nucleus and the sign would imply a prolate shape, but these nuclei do not display rotational energy spectra. The nucleus Cd^{114} which displays one of the best harmonic spectra known would be expected to have no quadrupole moment. Thus the experimental quadrupole moments pose a serious problem about the nature of the lowest states in medium weight nuclei.

C H A P T E R 1

INTRODUCTION

One striking feature which is evident in most medium weight nuclei is the existence of collective motion. This is most convincingly demonstrated in the case of nuclei in the mass 150 to mass 190 region where the low energy excited states display well developed rotational characteristics beautifully explained by Bohr and Mottelson (Boh 52, 53). In the majority of nuclei which do not reveal this rotational structure there is still ample evidence for enhanced electric quadrupole transitions associated with collective effects and in some even-even nuclei there appear to be low energy spectra characteristic of quadrupole surface vibrations about a spherical shape. This latter phenomenon is neither so convincingly demonstrated nor so general as the rotational case (Dar 64) and it is with these spherical nuclei that the present work is chiefly concerned.

In an effort to understand better both low energy properties of spherical nuclei and the phenomenological parameters of the rotational model the approach in recent years has been to begin with the shell model (May 48, 49, 50; Hax 49) and

consider residual interactions between nucleons which have not been completely incorporated into the self-consistent shell model potential. Although this approach is nice conceptually, in practice the computational complexity is enormous unless the residual forces are particularly simple. Fortunately, there appear to be only two dominant components in the residual interaction, a short range pairing force which only operates between nucleons very close to each other and a long range polarizing force.

The pairing force is assumed to be responsible for phenomenon such as the energy gap between the ground state and the first excited intrinsic (single-particle) state in even-even nuclei (Boh 58) and the long range force for collective features. In nuclei with only a few nucleons outside the closed shells of the shell model the pairing force is dominant and contributes to maintaining a spherical shape. The long range force is generally considered to be of quadrupole character because the principal collective phenomena of these nuclei is enhanced electric quadrupole transitions. The approach of including a pairing force and a quadrupole force has been extensively applied by Kisslinger and Sorensen (Kis 60, 63) to most of the nuclei in the mass 50 to mass 200 region and it has had considerable success in determining

energy levels for a large body of nuclei. The predictions of electric quadrupole transitions are not as satisfactory but for these experimental results are fewer and considerably less accurate.

This thesis presents the experimental determination of electric quadrupole phenomena in a large range of medium weight nuclei using the mechanism of heavy ion Coulomb excitation. Two particular types of measurements have been made, the accurate determination of electric quadrupole transition strengths and the direct measurement of the quadrupole moments (magnitude and sign) of the first excited states of spin and parity 2^+ of a few even-even nuclei.

Because the pairing force as it is now formulated is valid only for like nucleons the measurement of the electric quadrupole transition strengths has been confined to single-closed shell nuclei and to some of their isotopic neighbours in which neutrons and protons are filling different major shells. In this way, it is hoped to avoid the complexity of a neutron-proton short range force when interpreting the results (Kis 63). The measurements have been confined to two regions where results are scarce, the N = 28 region and the N = 82 region.

The single-closed shell nuclei Ti^{50}, Cr^{52} and Fe^{54} are

extremely interesting to study for two reasons. Firstly, the pure configuration approach to the calculation of excited state properties of the shell model has had some success in this region in predicting excited state energies and magnetic dipole moments, but it is not known if this success extends to electric quadrupole transitions. Secondly, the pairing force theory was not very successful in the neighbouring nickel region (Z = 28) in predicting the quadrupole transition strengths, and a study of the Ti^{50}, Cr^{52} and Fe^{54} isotones might shed some light on the discrepancies in the Ni isotopes (see Section 5.1).

The stable isotopes of Nd and Sm inhabit another interesting region extending from a closed shell (N = 28) to the deformed region. In fact Sm^{154} exhibits well developed, rotational energy levels. Transition strengths in the single-closed shell nuclei, Ce^{140}, Nd^{142} and Sm^{144} and their isotopic neighbours Ce^{142}, $Nd^{143,144,146,148}$ and $Sm^{148,150}$ have been obtained in the present work and are compared to pairing force theories.

Although the pairing plus quadrupole force theory provides a less arbitrary starting point for the vibrational model than a phenomenological approach, in its simplest form it gives similar properties such as harmonic energy levels.

This harmonic energy structure is never found and in order to aid understanding the nature of the lowest states in spherical nuclei the direct measurement of the quadrupole moments of the first 2^+ states in Cd^{114}, Sm^{148} and Sm^{150} has been made using the "reorientation" effect of Coulomb excitation (Bre 56). The nucleus Cd^{114} presents one of the best examples of a vibrational spectrum and in the harmonic approximation should have no quadrupole moment. The nuclei Sm^{148} and Sm^{150} are in the middle of the extremely interesting (and unexplained) transitional region noted above. A determination of the excited state quadrupole moments of these nuclei is clearly necessary to an understanding of the low energy properties of these nuclei.

Chapter 2 discusses the mechanism of Coulomb excitation, with emphasis on that produced by heavy ions, and pairing force theories. In Chapter 3 are given the details of the measurement of Coulomb excitation cross-sections. Chapter 4 presents the electric quadrupole transition strengths and moments extracted from the experimental results which are then discussed in Chapter 5 with reference to the pairing force theories and some other nuclear models.

C H A P T E R 2

T H E O R Y

2.1. Coulomb Excitation Theory.

Coulomb excitation is the process whereby a nucleus is put into an excited state through the mechanism of the time-dependent electromagnetic interaction between the nucleus and a charged projectile moving near it. In the present work the projectiles which have been used are O^{16} nuclei and S^{32} nuclei, with energies typically in the region of 1 - 3 MeV/amu. With heavy ions of these energies bombarding medium weight nuclei the excitation can be treated in the semi-classical approximation. In this approximation the time-dependent interaction is calculated from the classical motion of the projectile and the excitation of the nucleus caused by this interaction is treated quantum-mechanically. Generally the effect of the interaction is small and the excitation may be calculated using perturbation theory.

2.1. 1. Criteria for Semi-Classical Approximation. The principal criterion for treating the interaction classically

is that the wavelength associated with the projectile is much smaller than the closest distance that the projectile comes to the nucleus; that is, the projectile appears like a classical charged body. The projectile follows a Rutherford orbit and the distance of closest approach is

$$2a = \frac{2 Z_1 Z_2 e^2}{m v^2} \qquad (2.1)$$

where Z_1 and Z_2 are the projectile and nuclear charges respectively, m is the mass of the projectile (or the reduced mass of projectile and nucleus for finite nuclear mass) and v is the velocity of the projectile relative to the nucleus. If $\lambda\!\!\!^{-}$ is the wavelength of the projectile, then the criterion for the validity of the semi-classical approximation is

$$\frac{a}{\lambda\!\!\!^{-}} >> 1. \qquad (2.2)$$

These two equations then reduce to

$$\eta = \frac{Z_1 Z_2 e^2}{\hbar v} >> 1 \qquad (2.3)$$

In addition to the above criterion there should be

the restriction that the projectile motion is insignificantly affected by the excitation of the nucleus; in other words, that the excitation energy is small compared to the projectile energy.

2.1.2. Electric Interaction. The dominant interaction between a point charge projectile Z_1 e with a nucleus having Z_2 point protons can be written as (Ald 56)

$$V = \sum_k \frac{Z_1 e^2}{\bar{r}_p(t) - \bar{r}_k(t)} \qquad (2.4)$$

where $\bar{r}_p(t)$ is the vector distance from the projectile to the centre of the nucleus and $\bar{r}_k(t)$ is the vector distance from the kth nuclear proton to the centre of the nucleus. Defining the angle between $\bar{r}_p(t)$ and $\bar{r}_k(t)$ as θ_{pk}, V can be expanded as a power series (Mar 56)

$$V = \sum_k \sum_\lambda \frac{Z_1 e^2}{r_p(t)} P_\lambda (\cos\theta_{pk}) \left\{\frac{r_k(t)}{r_p(t)}\right\}^\lambda \qquad (2.5)$$

This is the multipole expansion of the interaction V. The first term ($\lambda = 0$) is the elastic scattering term which gives rise to the Rutherford orbit and cross-section $d\sigma_R$,

$$d\sigma_R = \frac{1}{4} \cdot \frac{a^2}{\sin^4(\frac{\theta}{2})} d\Omega_R, \qquad (2.6)$$

for scattering at a centre-of-mass angle θ into a solid angle $d\Omega_R$. The remaining terms of the expansion are the perturbing interactions resulting in excitation of the various electric multipole orders λ.

Interactions with the magnetic field of the projectile can also cause excitations, but these interactions are very weak. Only electric excitations are reported in this work and the theoretical discussion will be confined to them.

2.1. 3. Excitation Cross-Sections. Provided that the orbit of the projectile is not appreciably affected by the excitation the differential cross-section for excitation is (Ald 56)

$$d\sigma = P(\theta)\, d\sigma_R \qquad (2.7)$$

where $P(\theta)$ is the probability of excitation by projectiles scattered into a solid angle $d\Omega_R$ about θ. In terms of the probability amplitudes for excitation from an initial state i to a final state f $P(\theta)$ can be written as

$$P(\theta) = \frac{1}{2I_i+1} \sum_{M_i M_f} \left| b_{if} \right|^2 \qquad (2.8)$$

where I_i is the initial state spin, and M_i and M_f are the

magnetic quantum numbers of the initial and final states.

First-order time-dependent perturbation theory gives (Ald 56)

$$b_{if} = -\frac{i}{\hbar} \int_{-\infty}^{\infty} \langle f \mid H(t) \mid i \rangle \, e^{i\omega t} \, dt \qquad (2.9)$$

where

$$\omega = \frac{\Delta E}{\hbar} = \frac{E_f - E_i}{\hbar} \qquad (2.10)$$

and E_i and E_f are initial and final state energies. The interaction energy H(t) is V of equation (2.5) but with the monopole term ($\lambda = 0$) removed.

When the calculations are carried out the result is that the differential cross-section can be factored into two parts, the one depending essentially on the kinematics of the reaction which can be calculated once and for all and the other which depends on the nuclear matrix elements for the transition, $B(E\lambda)$ (Ald 56). Thus

$$d\sigma_E = \left(\frac{Z_1 e}{\hbar v}\right)^2 a^{-2\lambda + 2} \, B(E\lambda) \, df_{E\lambda}(\theta, \xi) \qquad (2.11)$$

The factor $df_{E\lambda}(\theta \xi)$ is called an excitation function and

depends on the energy of excitation through the parameter ξ, where

$$\xi = \eta \frac{\Delta E}{2E} = \frac{a}{v} \cdot \frac{\Delta E}{\hbar} \qquad (2.12)$$

and E is the projectile energy. The parameter ξ is called an adiabaticity parameter which gives the time that the interaction effectively operates relative to the nuclear period.

The total cross-section can be obtained by integrating $d\sigma_E$ over all angles.

The reduced transition strength of multipole order $E\lambda$, $B(E\lambda)$, is defined by

$$B(E\lambda;\ I_i \rightarrow I_f) = \sum_{M_f\ \mu} \left|\langle I_i\ M_i \mid m(E\lambda,\mu) \mid I_f\ M_f\rangle\right|^2$$

$$= \frac{1}{2I_i + 1} \left|\langle I_i \parallel m(E\lambda) \parallel I_f\rangle\right|^2 \qquad (2.13)$$

where I_f is the final state spin and $m(E\lambda,\mu)$ is an electric multipole moment of the nucleus. It has become traditional to measure the reduced transition probabilities $B(E\lambda)$ in "single particle" units defined as (Ald 56)

$$B(E\lambda)_{sp} = (2\lambda + 1) \frac{e^2}{4\pi} \left(\frac{3}{3+\lambda}\right)^2 R_o^{2\lambda} \qquad (2.14)$$

Throughout the present work the nuclear radius R_o used in calculating $B(E\lambda)_{sp}$ is given by

$$R_o = 1.2\, A^{1/3} \text{ fm.} \qquad (2.15)$$

The factor $(2\lambda + 1)$ has been somewhat arbitrarily introduced and is inappropriate in many cases. For odd nuclei the single-particle unit used in the present work is the Weisskopf unit

$$B(E2)_W = \frac{B(E2)_{sp}}{2\lambda + 1} \qquad (2.16)$$

The excitation functions (for both differential and total cross-sections) have been calculated for a number of the lower multipoles and Biedenharn and Brussard (Bie 65) list the various sources from which they can be obtained.

2.1.4. Symmetrization of Cross-Sections. The expression for the cross-section, equation (2.11), was derived under the assumption that the projectile loses no energy during the excitation process and correspondingly that there is

only one velocity v associated with the reaction. In fact there are two velocities, v_i the initial relative velocity and v_f the final relative velocity after excitation. To make equation (2.11) more generally useful it is desirable to find some orbit intermediate between those given by v_i and v_f which yields a cross-section agreeing most closely with an exact quantum mechanical calculation (see Ald 56; Bru 63). From a consideration of the symmetry of the quantum mechanical expressions Alder et al (Ald 56) propose a symmetrization procedure which involves replacing the velocity v by the geometric mean of v_i and v_f, thus

$$v \longrightarrow (v_i\, v_f)^{\frac{1}{2}} \tag{2.17}$$

and

$$\eta \longrightarrow (\eta_i\, \eta_f)^{\frac{1}{2}} \tag{2.18}$$

A more recent proposal (Bru 63) is to use the following symmetry procedure

$$\eta \longrightarrow \left\{ \frac{2(\eta_i^{\,2} + 1)(\eta_f^{\,2} + 1)}{(\eta_i^{\,2} + 1)^{\frac{1}{2}} + (\eta_f^{\,2} + 1)^{\frac{1}{2}}} \right\}^{\frac{1}{3}} \tag{2.19}$$

In subsection 4.1. 3 it is shown that these two procedures are almost equivalent for large η_1 and consequently the simpler method of equation (2.17) is used through the present work.

The symmetrized differential cross-section then becomes

$$d\sigma_{E\lambda} = \left(\frac{Z_1 e}{\hbar v_1}\right)^2 a^{-2\lambda+2} B(E\lambda) df_{E\lambda}(\theta, \xi) \qquad (2.20)$$

where a and ξ are appropriately symmetrized using the values of v and η given in equations (2.17) and (2.18). Brussard and Biedenharn show that very good agreement between the semi-classical differential E2 cross-section and the exact quantum mechanical calculation is obtained using the symmetrization procedure of equation (2.20) for η_i as small as 1.0 and ξ as large as 0.8. There is at present, however, little experimental evidence that the procedure works equally well for other multipoles.

. . .

2.1. 5. Projectile Energy Restrictions. The requirement that the energy loss to the projectile is small puts a lower limit on the projectile energy. The semi-classical theory shows that the excitation cross-section falls off

exponentially with large ξ. In practice ξ of unity is the upper limit for observing Coulomb excitation.

Generally the upper limit on the bombarding energy is determined by the Coulomb barrier E_B,

$$E_B = 1.44 \frac{Z_1 Z_2}{r_o (A_1^{1/3} + A_2^{1/3})} \left(\frac{A_1 + A_2}{A_2}\right) \text{MeV} \qquad (2.21)$$

if r_o is expressed in fm.
This expression gives the Coulomb barrier in the laboratory coordinate system.

The parameter r_o is derived from the assumption that a nucleus is a uniformly charged sphere of radius R given by

$$R = r_o A^{1/3} \qquad (2.22)$$

Ideally r_o would be the same for all nuclei. In fact it is found that r_o has different values depending on how it is determined, for example, by electron scattering or heavy ion transfer reactions, and also depending on the nucleus. During the present work a value of r_o of 1.76 fm which seems appropriate for Coulomb excitation work has been obtained (subsection 5.1. 6).

The criteria that $\xi \leq 1$ and that the bombarding

energy is less than E_B puts an upper limit on ΔE of the order of 4 MeV for nuclear projectiles.

2.1. 6. Angular Distribution of Gamma Rays. Although the angular distribution of gamma rays following Coulomb excitation has not been measured in the present experiments, a knowledge of their distribution is essential to extract the probability of excitation for scattering at a particular angle from the results of coincidence measurements between backscattered projectiles and gamma rays. It can be shown that provided there is no overlap of the projectile wavefunction and the nuclear wavefunction the distribution of the deexcitation gamma rays following inelastic scattering in a given direction can be obtained from a gamma-gamma correlation in which the first gamma ray has the multipolarity of the excitation process by simply multiplying each term of the latter correlation by a "particle parameter" $a_{kK}^{E\lambda}(\xi, \eta_1, \theta)$ which depends only on the scattering angle θ and the initial and final energies of the projectile (Ald 56; Bie 65). Thus the angular distribution is

$$W(\theta, \theta_\gamma, \phi_\gamma) = \sum_{k,K} a_{kK}^{E\lambda}(\xi, \eta_1, \theta)\, A_k^{(\lambda)}\, D_{K,0}^{k}(\phi_\gamma, \theta_\gamma, 0) \quad (2.23)$$

for k even. The coefficients $A_k^{(\lambda)}$ are standard gamma-gamma

correlation coefficients (Bie 53; Fer 55), $D^{k}_{K,0}(\phi_\gamma,\theta_\gamma,0)$ are elements of rotation matrices where θ_γ is the angle between the incident beam direction and the gamma ray and ϕ_γ is the angle between the planes defined by the incident projectile direction and gamma ray and by the incident projectile and emergent projectile directions. If the counter detecting the emergent projectile is symmetric about the incident beam direction, then ϕ_γ is averaged over and $K = 0$ so that the angular distribution simplifies to

$$W(\theta,\theta_\gamma) = \sum_k a^{E\lambda}_{k0}(\xi, \eta_i, \theta) A^{(\lambda)}_k P_k(\cos\theta_\gamma) \qquad (2.24)$$

The particle parameters $a^{E\lambda}_{kK}$ have been evaluated in the sudden approximation ($\xi = 0$) (Ald 62) and in the classical limit of $\eta_i = \infty$ (Yat 61; Elb 64). A discussion of the particle parameters and angular distributions used in the present work is presented in subsection 4.2. 5.

2.1. 7. Experimental Excitation Probability. The determination of the experimental excitation probability by measuring the inelastic cross-section relative to the elastic cross-section is usually done with the same fixed laboratory scattering angle and solid angle for both

inelastic and elastic scattering. Consequently to extract $B(E\lambda)$ values the measured probability must be compared to the following calculated probability :

$$P = \frac{d\sigma_{E\lambda}(\theta_{E\lambda})/d\Omega_{E\lambda}}{d\sigma_{R}(\theta_{R})/d\Omega_{R}} \qquad (2.25)$$

where $\theta_{E\lambda}$ and θ_{R} are the centre-of-mass inelastic and elastic scattering angles and $d\Omega_{E\lambda}$ and $d\Omega_{R}$ are the respective centre-of-mass solid angles corresponding to the laboratory scattering angle θ_{L} and solid angle $d\Omega_{L}$.

2.1. 8. Multiple Excitation; Second Order Perturbation Theory. The probability for excitation given in equation (2.9) may become large enough with the use of heavy ions that higher order effects, such as double excitation, may become significant. However, the probability may still be much less than one and a second order perturbation expansion may still be accurate.

The transition amplitude to second order can be written as (Ald 56)

$$b_{if}^{(2)} = b_{if} + \sum_{z} b_{izf} \qquad (2.26)$$

where the summation over all the intermediate states z

includes the initial and final states. The first order amplitude is given by equation (2.9) and the second order amplitude is given by

$$b_{izf} = -\frac{1}{\hbar^2}\int_{-\infty}^{\infty} dt \langle f \mid H(t) \mid z \rangle e^{i\omega_{zf}t} \int_{-\infty}^{t} dt' \langle z \mid H(t') \mid i \rangle e^{i\omega_{iz}t'} \qquad (2.27)$$

where

$$\omega_{zf} = \frac{E_f - E_z}{\hbar} \quad \text{and} \quad \omega_{iz} = \frac{E_z - E_i}{\hbar} \qquad (2.28)$$

Using the interaction H(t) of subsection 2.1. 3 the b_{izf} can be calculated in the semi-classical approximation and the excitation cross-section can be separated into three terms

$$d\sigma_{E\lambda} = d\sigma^{(1)}_{E\lambda} + d\sigma^{(1,2)}_{E\lambda} + d\sigma^{(2)}_{E\lambda} \qquad (2.29)$$

The first term is the cross-section given by equation (2.11); the second term is the interference between first and second order transitions; the third term represents only part of the second order cross-section because interference terms between first and third order transitions have been neglected.

2.1. 9. The "Reorientation" Effect. The term $d\sigma^{(1,2)}$ in equation (2.29) might be particularly large when the intermediate state z is one of the magnetic substates of the final state f (Bre 56). An electric quadrupole transition from z to f then results from an interaction between the quadrupole moment of the final state and the divergence of the time-varying electric field at the nucleus caused by the projectile. The quadrupole moment Q is defined in terms of the quadrupole moment operator m(E2,0) by

$$eQ = 4\sqrt{\frac{\pi}{5}} \left\langle JJ \left| m(E2,0) \right| JJ \right\rangle$$

$$= 4\sqrt{\frac{\pi}{5}} \left(\frac{J(2J-1)}{(2J+1)(J+1)(2J+3)} \right)^{\frac{1}{2}} \left\langle J \left\| m(E2) \right\| J \right\rangle \quad (2.30)$$

where J is the spin of the state f.

In analogy with $B(E2)_{sp}$ (subsection 2.1. 3) a single-particle quadrupole moment can be defined for a proton in a single-particle state j (Boh 53)

$$eQ = - \frac{2j - 1}{2(j+1)} \left(\frac{3 R_0^2}{5} \right) \quad (2.31)$$

In this derivation it is assumed that the radial wavefunction for the proton is constant out to the radius of the nucleus,

and zero elsewhere.

The name "reorientation effect" which has been applied to the interference term $d\sigma^{(1,2)}$ when the state z is one of the magnetic substates of state f is somewhat of a misnomer because it implies that the interaction with the quadrupole moment always results in a nuclear spin flip, whereas in fact much of the contribution to $d\sigma^{(1,2)}$ comes from the interaction term $\langle 20 \mid m(E2,0) \mid 20 \rangle$ especially at scattering angles back of 90°. In the limit of 180° scattering of a spin zero projectile on an even-even nucleus only the zero magnetic substate can be populated and yet the "reorientation effect" is a maximum, (see Figure 2.1 and below).

In the present work the differential cross-section with the interference correction is calculated from

$$\left(\frac{d\sigma}{d\Omega}\right)_{E2} = \frac{d\sigma^{(1)}}{d\Omega} \left(1 + \Delta^{(1)} Q \right) \qquad (2.32)$$

where

$$\Delta^{(1)} = \frac{Z_1 e}{4 \hbar v a^2} L(\theta, \xi). \qquad (2.33)$$

$L(\theta, \xi)$ is a function which has been calculated by Douglas (Dou 65) and is shown in Figure 2.1. The functions $\Delta^{(1)}$

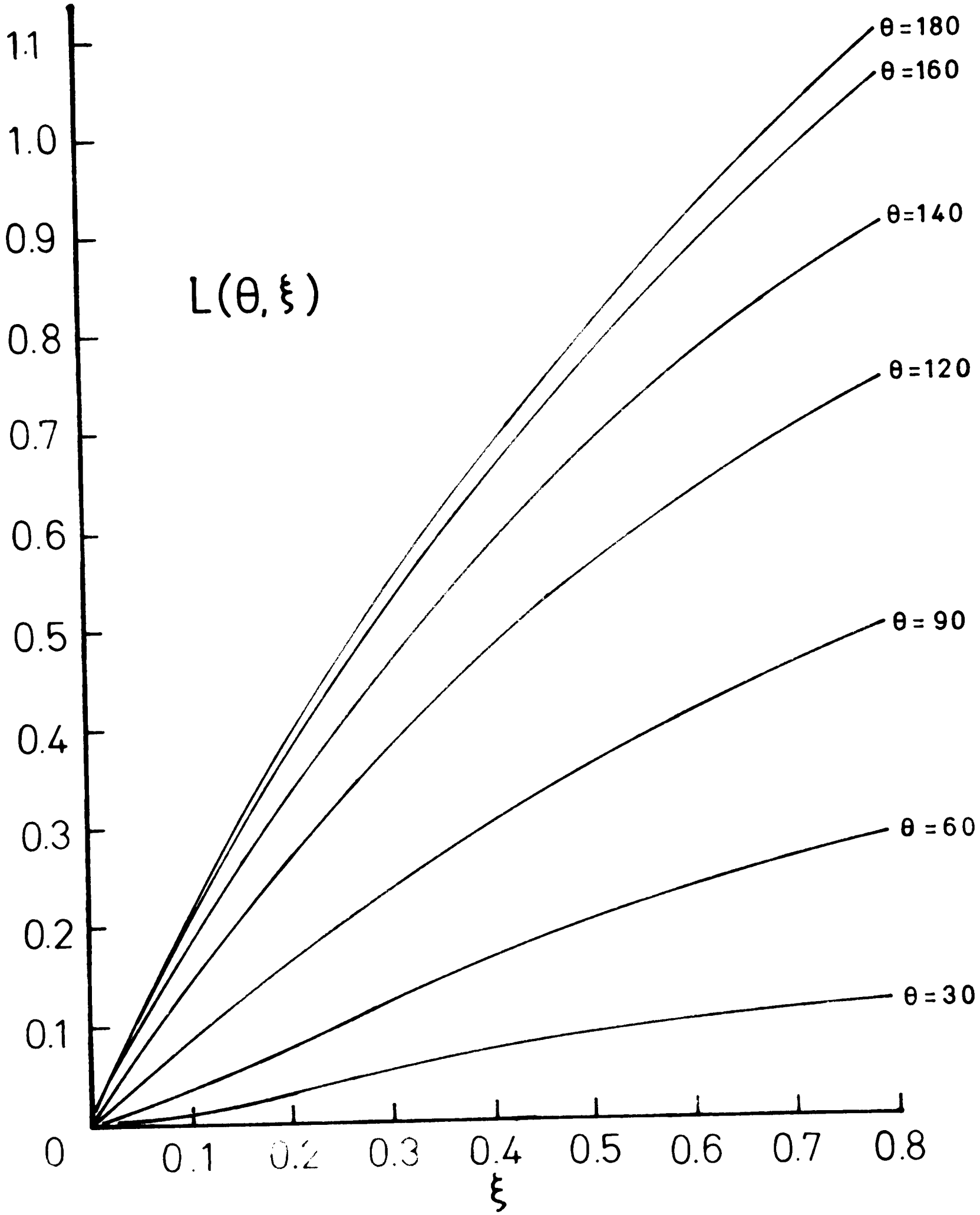

L(θ, ξ)
θ = 180
θ = 160
θ = 140
θ = 120
θ = 90
θ = 60
θ = 30
1.1
1.0
0.9
0.8
0.7
0.6
0.5
0.4
0.3
0.2
0.1
0
0.1
0.2
0.3
0.4
0.5
0.6
0.7
0.8
ξ

Fig. 2.1

are very insensitive to changes in bombarding energy and tb angle near 180°.

The second order term $d\sigma^{(2)}$ of equation (2.29) has been neglected in the present work because it is smaller than the interference term (usually by an order of magnitude) and because other terms of the same magnitude but of unknown sign have been neglected. Although some of these neglected terms have been calculated using perturbation theory and the calculations seem to justify the conclusion that they will decrease $d\sigma^{(2)}$ (Lin 63) a more satisfactory test of the range of validity of the perturbation approach which includes only $d\sigma^{(1,2)}$ is to solve the Schrodinger equation for the interaction between nucleus and projectile (subsections 2.1. 11 and 4.3. 6).

2.1. 10. Virtual El Excitation of Giant Dipole Resonance. Eichler (Eic 64) has suggested that virtual El-El excitation by way of the giant dipole resonance to the first excited 2^{+} state may involve a correction to the first-order Coulomb excitation cross-section to the 2^{+} state which is of the same order of magnitude as the reorientation effect. MacDonald (Mac 64) however has shown that this effect has been overestimated by a factor of twelve in a simple collective model. MacDonald and Douglas (Mac 65) have recently

calculated the effect for a giant dipole resonance made up of numbers of quadrupole phonons coupled to the dipole phonon and the effect is smaller, by a factor of ten, than suggested by Eichler. It has therefore been neglected in the present work.

2.1. 11. Multiple Excitation; Schrodinger Equation Method.

In the case of Coulomb excitation of collective nuclei induced by heavy ions the possibility exists that the excitation probability given by first order perturbation theory may be very large and may even exceed unity. The obvious inadequacy of the theory is then evident. In such cases the nucleus may reach fairly high excited states by way of multiple excitation and the problem of calculating the populations of the final states involves solving the time-dependent Schrodinger equation for the total Hamiltonian of nucleus and interaction.

Because multiple excitation is only feasible for heavy ions the Sommerfeld number η is usually quite large, typically 50, and the regime of classical orbits is clearly valid (subsection 2.1. 1). Consequently the interaction part H(t) of the Hamiltonian is given by equation (2.5) with the monopole term subtracted. The chief difficulty

in solving the Schrodinger equation is that the calculation must be tailored to fit a particular nucleus or nuclear model, and very few nuclei are amenable to solution. Only the probabilities for exciting the levels in a harmonic oscillator nucleus have been calculated for arbitrary ξ and scattering angle θ, and for the rotational model only the solutions for the sudden approximation with $\xi = 0$ for all levels are easily achieved. The results for these two cases, due to Alder and Winther (Ald 60(are not presented here because none of the present work involves multiple excitation in which many states are excited. One aspect of multiple excitation which will be discussed is its use to check the usefulness of perturbation theory for extracting quadrupole moments when the probability of excitation is still small.

The Schrodinger equation for the electric interaction with a nucleus,

$$i\hbar \frac{\partial \psi}{\partial t} = H_T \psi \qquad (2.34)$$

where

$$H_T = H_{nucleus} + H(t), \qquad (2.35)$$

can be rewritten as a set of coupled differential equations for the amplitudes of the eigenstates of the nuclear

Hamiltonian (Ald 60). Thus if

$$H_{\text{Nucleus}} \cdot u_n = E_n u_n \tag{2.36}$$

and $$\psi = \sum_n a_n(t) u_n e^{-i E_n t/\hbar} \tag{2.37}$$

then

$$i \hbar \dot{a}_n(t) = \sum_k \langle n \mid H(t) \mid k \rangle e^{i\frac{(E_n - E_k)t}{\hbar}} a_k(t) \tag{2.38}$$

The solution of this complete set of equations is sought.

If the probability of excitation is kept low, then only a small number of levels are involved and it is possible by numerical techniques to solve equation (2.38). The parameters of the calculation are the energies of the excited states and the static and transition matrix elements of the nucleus. These calculations to date have been performed assuming only quadrupole excitations of up to six excited states (deB 65; Gol 65; Smi 65; Dou 65). One of the problems involved is that the phases of the matrix elements involved are not known without recourse to a specific nucleus model. Another is that the method of symmetrization of the cross-section (subsection 2.1. 4) is not easily

carried out, but this correction is fairly small for large η ($\simeq 2k$).

Some calculations along this line to determine quadrupole moments will be presented in subsection 4.3. 6.

2.2. Nuclear Theories.

2.2. 1. Phenomenological Models. There are two phenomenological models which have been applied with varying degrees of success in medium weight nuclei, the permanently deformed rotator model and the model of quadrupole surface vibrations about an average spherical shape (Boh 52, 53; Dav 58). The symmetric rotator model (Boh 52, 53) has been extremely successful in the nuclei from mass 150 to mass 190 but it will not be discussed here, although the idea of an intrinsic quadrupole moment will be used as a standard of comparison in the discussion on experimental quadrupole moments. The asymmetric rotator model (Dav 58) and the quadrupole vibrator model (Boh 52, 53) have both been used for even-even nuclei with nearly harmonic energy spectra and these nuclei constitute the bulk studied in the present work. The agreement between these models and experiment is far from good (Dar 64) and many refinements

have been added to these models, generally in a phenomenological way. A discussion of the properties of nuclei predicted by these models and some of their refinements will be left to Chapter 5. However, one of the main problems is that as more refinements are incorporated into these phenomenological models more parameters are introduced. Clearly it is desirable to eliminate some of these parameters and the remainder of this chapter deals with recent approaches to do this.

2.2. 2. Microscopic Models. The effort to relate the parameters of the phenomenological models of nuclei to microscopic properties starts with the shell model. The shell model wavefunctions are assumed to be good basis wavefunctions from which to begin the calculation of those properties of nuclei which are considered to result from residual forces between nucleons, forces which have been neglected in the self-consistent shell model potential. Two features make such a calculation exceedingly complex for a general residual force. One is that generally there are a fairly large number of particles outside a major shell; the second is that there is considerable configuration mixing within major shells and even between major shells.

The situation is saved by the realization that there appear to be two dominant contributions to the residual interaction, a pairing force and a long-range polarizing force. The short range pairing force operates between pairs of particles in the same spin state j but coupled to total spin zero, and this force explains the "energy gap" between the ground state and first intrinsic single-particle state observed in even-even nuclei (Boh 58). The long-range polarizing force correlates particle motion and accounts for the observed collective features of nuclei, notably the low-lying 2^+ states and enhanced electric quadrupole transitions found in many even-even nuclei (Bel 59, Kis 60, 63; Bar 60).

2.2. 3. Treatment of Pairing Forces. The solution of the problem of pairing forces between like nucleons has been treated extensively in the literature of the last few years and consequently will only be briefly sketched here (Bel 59; Kis 60; Lan 64).

A short range force between two nucleons is most effective when the nucleons are in the same orbit and consequently are often close together. Because of this a pairing force is introduced which has constant matrix elements

between pairs of like particles in the states $|j\ m\rangle$ and $|j\text{-}m\rangle$ coupled to zero total angular momentum and which has zero matrix elements between all other pairs. In the formalism of annihilation and creation operators the nuclear Hamiltonian becomes

$$H = \sum (\varepsilon_j - \lambda) a^+_{jm}\, a_{jm} - \frac{1}{4} G \sum_{\substack{jj' \\ mm}} a^+_{j'm'}\, a^+_{j'-m'}\, a_{j-m}\, a_{jm} \tag{2.39}$$

Here ε_j is the single-particle energy of a nucleon in a shell model state j, λ is an arbitrary reference energy and G is the strength of the pairing interaction. It is now convenient to introduce a state $|\tilde{0}\rangle$ in which all the lowest single-particle levels $j_1, j_2, \ldots j_n$ are filled, thus

$$|\tilde{0}\rangle = a^+_{j_1 m_1} \ldots a^+_{j_1 -m_1}\, a^+_{j_2 m_2} \ldots\ldots a^+_{j_n -m_n} |0\rangle \tag{2.40}$$

$$= \prod_{j,m>0} (U_j + V_j\, a^+_{jm}\, a^+_{jm})|0\rangle$$

where

$$a_{j_i m_i} |0\rangle = 0 \tag{2.41}$$

for all j_i. New operators which operate on $|\tilde{0}\rangle$ in the same way in which a^+_{jm} and a_{jm} operate on $|0\rangle$ are then

defined as (Bog 58; Val 58)

$$b^{+}_{jm} = U_j a^{+}_{jm} - V_j a_{j-m}$$
$$b^{+}_{j-m} = U_j a^{+}_{j-m} + V_j a^{+}_{jm} \qquad (2.42)$$

where U_j and V_j account for the fact that the pairing force can act to scatter pairs of particles from (normally) occupied to unoccupied orbitals. These new operators, which are a linear combinations of shell model particle and hole creation and annihilation operators, are called quasi-particle creation and annihilation operators, and the state $|\tilde{0}\rangle$ is the quasi-particle vacuum state. The substitution of these operators into equation (2.39) results in the Hamiltonian taking the form (Lan 64)

$$H = H_{00} + H_{11} + H_{20} + H_{int} . \qquad (2.43)$$

H_{00} is the expectation value of H in the quasi-particle vacuum state $|\tilde{0}\rangle$. H_{11} is the Hamiltonian of a set of independent quasi-particles. H_{20} describes the interaction between a two-quasi-particle state and a zero-quasi-particle state and can be made to vanish by a proper choice of U_j

and V_j. This procedure is equivalent to minimizing the ground state energy (Lan 64). With the neglect of H_{int} which contains higher order interaction terms between quasi-particles equation (2.43) represents the Hamiltonian of a set of independent quasiparticles which, however, no longer commutes with the particle number operator. Thus eigenstates of H are mixtures of states of different numbers of particles. To choose the state most closely resembling the real state the formerly arbitrary parameter λ is adjusted to make the average number of particles in the state equal to the real number.

For an even number N of particles the ground state is the quasi-particle vacuum with energy

$$E_N = \sum_j (2j + 1) \tilde{\varepsilon}_j v^2_j - \frac{\Delta^2}{G} \qquad (2.44)$$

where

$$\tilde{\varepsilon}_j = \varepsilon_j - G v^2_j \qquad (2.45)$$

and

$$\Delta = G \sum_j u_j v_j \qquad (2.46)$$

The quantity Δ is called the gap parameter and gives the extent to which the pairing force scatters particles

from the occupied to the unoccupied states.

The first excited state of the even system results when a pair of particles coupled to spin zero is broken and the two particles occupy orbitals j_1 and j_2. The energy of excitation is

$$E_x = e_{j1} + e_{j2} \tag{2.47}$$

where e_{j1} is the quasi-particle energy

$$e_{j1} = \sqrt{(\tilde{\varepsilon}_{j1} - \lambda)^2 + \Delta^2} \tag{2.48}$$

Since $\tilde{\varepsilon}_{j1}$ is of the same order as λ, there is then an energy gap of 2 in the even system.

For an odd number of nucleons, the lowest states will be different one quasi-particle states and there will be no gap.

2.2.4. Collective Motion. Although the short range pairing force accounts for the different type of energy spectra observed in even-even and odd nuclei, in the form discussed above it will not produce a spectrum within the energy gap having the characteristics of a quadrupole vibrator which seems to exist in even-even nuclei with a

few nucleons beyond a closed shell. It might be supposed that interactions between quasi-particle states could account for these vibrational-type states.

Interactions between quasi-particles can be treated in several ways. One method is to introduce into the Hamiltonian a long-range quadrupole force between pairs of particles (Kis 60; 63). Another method is to use a more general type of short range force than the pairing force and include the terms of H_{int} which were previously neglected (Rho 65).

2.2.5. Quadrupole-Quadrupole Force. Because the dominant feature of the low excited states of even-even nuclei are quadrupole excitations, Kisslinger and Sorensen add a quadrupole-quadrupole force without exchange properties to the Hamiltonian (equation (2.39)) of the form

$$H_Q = \frac{-X}{2} \sum Q_m(j_1 j_3) Q_{-m}(j_2 j_4)\, a^+_{j_1 m_1}\, a^+_{j_2 m_2}\, a_{j_3 m_3}\, a_{j_4 m_4} \qquad (2.49)$$

where X is the strength of the force and

$$Q_m(j_1 j_3) = \langle j_1 m_1 \,|\, r^2\, Y_{2m} \,|\, j_3 m_3 \rangle \qquad (2.50)$$

In terms of quasi-particle operators the total Hamiltonian

becomes

$$H = \sum_j e_j \, b^+_{jm} \, b_{jm} - H' \qquad (2.51)$$

and H' contains terms in four quasi-particle operators.

Because the spectrum of some even-even nuclei is like a harmonic oscillator spectrum it might be expected that an operator 0^+ could be found which would satisfy the commutation relation

$$[H, O^+_{JM}] = \omega_J \, O^+_{JM} \qquad (2.52)$$

and because the quadrupole force operates between pairs of quasi-particles these 0^+ operators might be composed of quasi-particle pair creation and destruction operators

$$A^+_{JM} = b^+_{j_1 m_1} \; b^+_{j_2 m_2} \qquad (2.53)$$

where $j_1 m_1$ and $j_2 m_2$ are coupled to JM. Although the commutation relations $[H, A^+]$ and $[H, A]$ contain terms in A^+, A and higher order terms like A^+A^+ the approximation of making the operators O^+ a linear combination of A^+ and A is then made. This is called the linearization of the equations of motion or the random phase approximation.

(Bayman (Bay 64) shows that this approximation is equivalent to making the A^+ and A operators into boson operators. For a critical discussion of the whole basis of using the linearization method for nuclei see Lane (Lan 64)).

The secular equation from the equation of motion (equation (2.52)) is then solved for the energies ω_J. The eigenstates of H are of the form

$$\left|\tilde{\tilde{0}}\right\rangle \ , \ O^+_{JM} \left|\tilde{\tilde{0}}\right\rangle \ , \ \text{etc.} \qquad (2.54)$$

where

$$O_{JM} \left|\tilde{\tilde{0}}\right\rangle = 0 \qquad (2.55)$$

The above procedure generates harmonic oscillator spectra, with a 0^+, 2^+, 4^+ triplet at twice the energy of the first excited 2^+ state. The energy of the triplet is often at about the same energy as the intrinsic quasiparticle states. In their first paper (Kis 60) Kisslinger and Sorensen used a different but less useful procedure to deal with collective levels and this will not be discussed here.

2.2. 6. Numerical Calculations. The pairing plus quadrupole force model has been used extensively by Kisslinger and Sorensen to calculate the properties of the low energy

excited states of single closed shell nuclei and neighbouring nuclei (Kis 60; 63). Although the above treatment of pairing forces will not work for a neutron-proton interaction, the nuclei which are studied are those in which the protons and neutrons are filling different major shells and they argue that the short range neutron-proton force can then be neglected. They thus have two pairing force parameters G_p and G_n. They also conclude that the long range quadrupole force acting between a neutron and a proton must be of approximately the same strength as between like nucleons and they thus have three quadrupole force strengths X_p, X_n and X_{np}.

For the calculations the single-particle energies ε_j are required and these energies constitute one of the major uncertainties. The choice of the best force parameters depends to some extent on the single-particle energies and they find that choosing $G_p = G_n$ and $X_p = X_n = X_{np}$ gives results which are as good as for any other choice considering the uncertainties in the ε_j's.

The pairing force strength G is chosen in a particular region of nuclei from a study of the odd-even mass differences and the energy gap and is typically of the order of 23/A MeV. The quadrupole force strength X is then

obtained by fitting the energy of the first 2^+ level in the region of interest.

They also predict B(E2) values for the ground to first excited state transitions (see also Sor 64) but unfortunately these calculations involve another parameter, an effective charge for the proton and neutron. This effective charge accounts for the interaction between the valence nucleons and the core which has not been completely accounted for by the residual interaction, and varies considerably with the number of single particle configurations taken into account. For the configurations used in Kis 63, an effective charge of 2e for protons and e for neutrons is used.

2.2. 7. Quasi-Particle Interactions. Another approach to the treatment of the collective levels is to consider more fully the quasi-particle interaction term H_{int} in the Hamiltonian which has been approximated by the quadrupole force. The approach of Rho (Rho 65) is to consider a more general type of residual force with finite range and consider all components of the force. The pairing and quadrupole interaction strengths are no longer independent variables.

As the quasi-particle interaction only the two quasi-

particle scattering term (designated H_{22}) is kept. Thus the Hamiltonian of the system can be written as

$$H' = H - H_{00} = H_{11} + H_{22}. \qquad (2.56)$$

The H_{22} matrix is diagonalized with the quasi-particle wavefunctions which are eigenstates of H_{11}. The eigenvalues of H_{22} give the excitation spectrum for various J.

With a general force Rho shows that to get coherent addition of all the quasi-particle components making up the first 2^+ state ($^e j_1 + {}^e j_2$) must be greater than $\hbar\omega_2$ and the force parameters must be chosen so that the off-diagonal elements of the H_{22} matrix are attractive.

The ground state is a pure quasi-particle vacuum. Rho also estimates the effect of ground state correlations on the B(E2; $0 \rightarrow 2$) strengths by treating another interaction term H_{40} which couples states differing by four quasi-particles by perturbation methods.

The calculations have been done for the N = 82 nuclei and they do not produce harmonic-like spectra which is encouraging because the level structure in the best studied nucleus Ce^{140} is far from harmonic. The calculations also produce enhanced B(E2) values for the ground to first 2^+ state transition, inhibited cross-over transitions to the

second 2^+ state, and generally inhibited transitions from the 4^+ state to the first 2^+ state. These properties are qualitatively in good agreement with the limited experimental evidence in these nuclei.

C H A P T E R 3

EXPERIMENTAL METHODS

The experimental work reported here was performed using oxygen and sulphur ion beams from the tandem Van de Graaff generator at A.W.R.E., Aldermaston.

3.1. Ti^{50}, Cr^{52}, Fe^{54}.

The single-closed shell nuclei Ti^{50}, Cr^{52} and Fe^{54} (N = 28) were Coulomb excited with beams of charge five O^{16} ions with well-defined energies from 31 MeV to 41 MeV, and ions scattered through 90° were analysed in an 180° double-focussing magnet and detected with nuclear emulsions. By this means it was possible to resolve inelastically and elastically scattered ions.

3.1. 1. Beam Energy. The ion beam from the tandem generator is first passed through a 90° analysing magnet before impinging on the target. This magnet was calibrated by scattering 10 MeV protons from a thin Pb^{208} target ($\approx$ 50 $\mu g/cm^2$) and analysing the scattered protons in the 180° magnetic spectrograph which has a known calibration

(Coh 61; Coo 64). Some experiments were done at another date when no proton calibration was made but it was possible to conclude from the O^{16} ion spectra observed in the spectrograph that the calibration was different by less than 0.14%. Consequently the proton calibration was used throughout to determine the O^{16} beam energies.

The beam was collimated by a 0.1 inch diameter hole in a 0.001 inch gold foil placed nine inches in front of the target.

3.1. 2. Targets. In order to resolve an inelastic oxygen group corresponding to an excitation energy of 1.4 MeV in a target nucleus in the mass 50 region, it is necessary to have very thin targets to minimise energy spread caused by the high rate of energy loss for O^{16} ions. For example, at 30 MeV the stopping power is 3 keV-cm^2/μg in nickel. (Boo 65). The targets should also be highly enriched to avoid scattering from neighbouring isotopes and if they are not self-supporting, it is an advantage to have them on a backing of an element of a lower mass than the projectile. It is then possible to choose a scattering angle at which oxygen ions will not scatter from the backing.

The present targets were made by directly depositing

the isotope from a mass separator at Aldermaston on various backings. Thin formvar and high purity graphite were both found to be unsuitable as backings, the former because it tended to break in the beam (possibly because of electrical stresses) and the latter because it produced a long tail on the low energy side of the elastic O^{16} group. The long tail may have been a result of surface irregularities of the graphite. Successful targets were achieved by depositing the isotopes on thin carbon films. To prevent breaking the film when making the deposition the 50 keV positive ions from the mass separator were retarded by a 49 kV potential at the collection end. The diameter of the deposited isotopes was about 0.35 cm.

The thickness of the target and carbon backing was measured using an α-particle thickness gauge (Ram 59). In this technique the change of the range in air of the α-particles from a well-collimated Po^{210} source when the target is interposed between source and detector is measured. Using air equivalents for the elements as tabulated in (Ram 59), the targets were found to have surface densities of approximately 20 $\mu g/cm^2$ and the carbon backings of 50 $\mu g/cm^2$. The measurements on each target were repeated several times and there was a variation in the thickness of

up to 30% from the mean. This variation probably reflects target or backing non-uniformities.

3.1. 3. Magnetic Spectrograph. The 180° double-focussing magnet used in this work is described in detail by Cohen et al (Coh 61) and Cookson and Wankling (Coo 64). However a few modifications were needed to make it usable for heavy ion detection. A rectangular slit was placed at the entrance to the magnet to cut down the horizontal width to one-third its usual size; i.e., the solid angle of acceptance was 0.0026 sr, made up of $^{2}/_{3}^{\circ}$ horizontal width and 13° vertical height. Thus scattered particles were detected in the angle $(90 \pm \frac{1}{3})^{\circ}$, and this $\frac{2}{3}^{\circ}$ angular spread gives rise to an energy spread in the scattered beam of about 135 keV (0.7%) for 35 MeV O^{16} ions scattered from Fe^{54}.

Preliminary investigation revealed a long tail on the low energy side of the elastic peak even when using targets on carbon foil backings. It was thought that the rather poor vacuum in the magnet vacuum chamber (approximately 0.5 torr measured at the detection end) resulted in collisions in which the ions changed charge states. To improve the vacuum a liquid nitrogen cold trap which cooled a large flat copper plate inside the "dustbin" (the receptacle

at the detection end housing the nuclear emulsion plates) was installed. This reduced the pressure measured in the "dustbin" to less than 0.01 torr with a consequent decrease in the background due to the elastic tail by a factor of six.

To aid positioning the scattered ion groups on the nuclear emulsions and to measure the relative charge state populations of the ions a Au-Si surface barrier detector was situated on the image plane of the spectrograph at the low energy end of the emulsion. This counter was about one inch in diameter and was covered with a 0.003 inch aluminium foil with a 0.25 inch wide slit, the length of which extended across the counter perpendicular to the plane of motion of the ions. The width of this slit was approximately equal to one quarter of the full width at half height of an O^{16} elastic group.

The nuclear emulsions used to detect the O^{16} ions were Ilford K-1 plates which are sensitive to heavily ionising particles. The tracks left by the O^{16} ions are of the order of 12 μm in length. Two plates fit into the plate holder and because of the double-focussing property of the magnet two experimental runs can be recorded on each plate. Thus four exposures could be made before letting the magnet up to air.

3.1. 4. The Experiment. The targets were placed at an angle of 45° to the beam and reflecting to the spectrograph (i.e., the scattered particles did not pass through the carbon backing). This reflecting position was found to give the best resolution. As an example, for 35.6 MeV O^{16} ions scattered from Fe^{54} the resolution in the reflecting position was 250 keV (1.25%) full width at half maximum (FWHM) and 320 keV FWHM in the transmitting position. Also, the transmitting position produced a long tail on the low energy side of the elastic group which was sufficient to obscure the inelastic group, which was about 1% of the elastic.

The choice of 90° as the scattering angle was somewhat arbitrary. From this angle backwards O^{16} ions are not scattered from elements lighter than mass 16. The spectrograph can be positioned as far around as 130° to the incident beam direction and Table 3.1 lists a comparison of 90° and 125° scattering for 35 MeV O^{16} ions on Cr^{52}. P is the probability for Coulomb excitation of the 1.43 MeV level and $d\sigma_{E2}/d\Omega$ is the electric quadrupole excitation cross-section (see Section 2.1). E is the energy of the elastically scattered ions and $\Delta E/E$ is the fractional energy difference between the inelastic and elastic ions.

T A B L E 3.1

A comparison of 90° and 125° scattering of 35 MeV O^{16} ions from Cr^{52}.

	90°	125°
P	1.23%	1.65%
$d\sigma_{\Omega 2}/d\Omega$	1.88 mb	1.43 mb
E	18.5 Mev	12.8 MeV
$\Delta E/E$	5.8%	7.0%
$dE/d\theta$	0.21 MeV/ $^{\circ}$	0.12 MeV/ $^{\circ}$

The ratio $dE/d\theta$ gives the kinematic energy spread per degree of angle.

It can be seen from the table that there are advantages and disadvantages to the choice of 90° as the scattering angle. The advantages are the higher excitation cross-section and the higher scattered energy. The nuclear emulsions accept an energy range of 9.8% of the mean energy

but because these plates are usually dirty at the ends, because it is difficult to position the groups exactly where desired on the plates, and because of the poor resolution for heavy ions the smaller $\Delta E/E$ at 90° permits the detection of both the inelastic and elastic group on the same plate at the same time. However, it may be an advantage to use scattering at 125° in the case of heavier target nuclei with lower energy excited states.

In order to choose beam energies safely below the Coulomb barrier, the ratio of yields of the O^{16} ions elastically scattered at 30° and 85.8° was measured. Two Au-Si surface barrier detectors in the target chamber were used to detect the scattered ions simultaneously and the spectra were stored in two multichannel pulse height analysers. The counter at 30° was 2.4 inches from the target and was collimated by a circular aperture 0.08 inches in diameter. The other counter was 2.3 inches from the target and was collimated by an aperture 0.025 inches wide and 0.375 inches long.

Figure 3.1 displays the ratio of the yield of O^{16} ions in the 30° counter to that in the counter at 85.8°. This ratio also includes the small contribution from the inelastically scattered ions which were not resolved from the

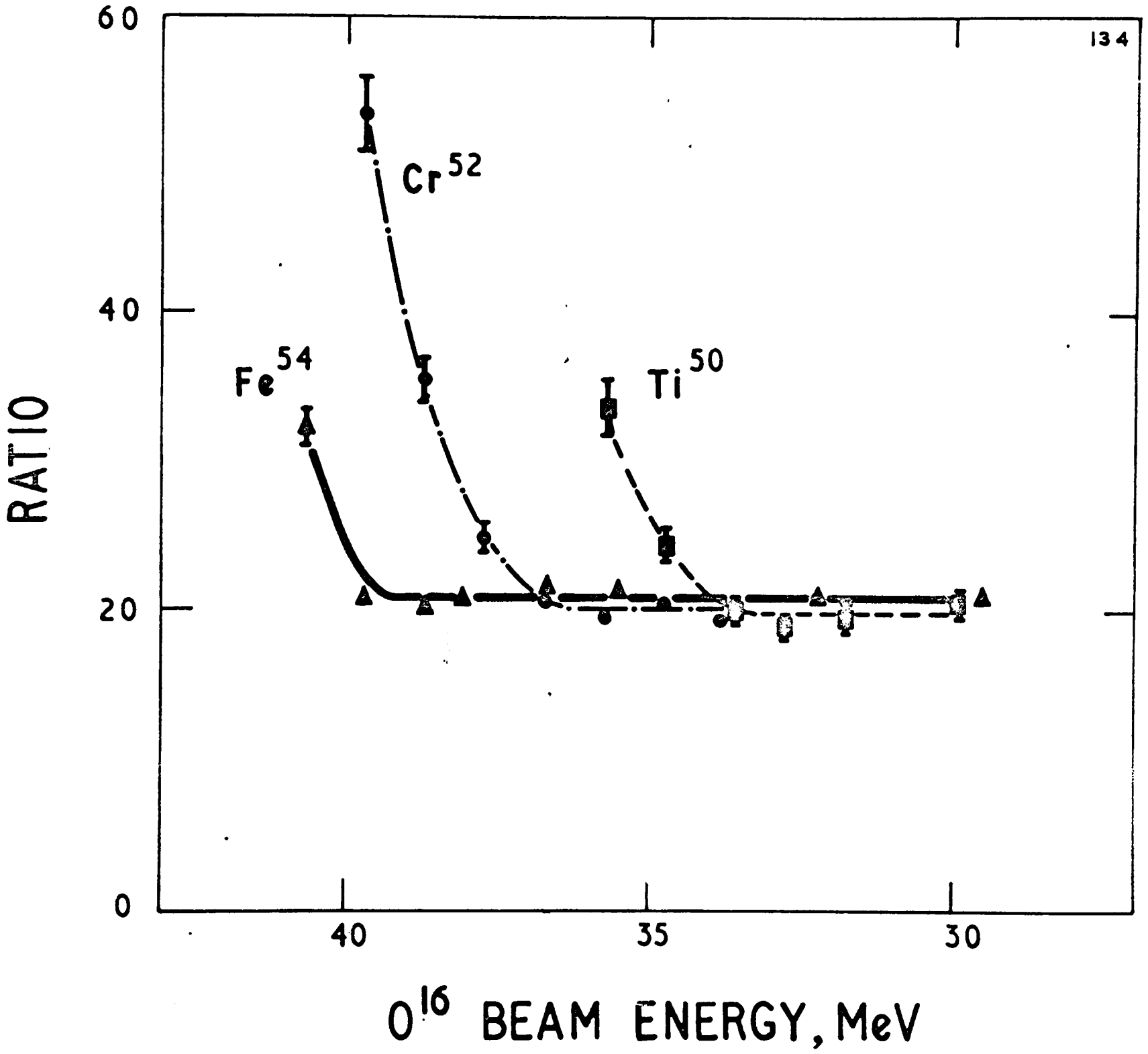


Fig. 3.1

elastically scattered ions. In the figure it may be noticed that the constant part of the Fe^{54} curve lies somewhat higher than the corresponding parts of the Ti^{50} and Cr^{52} curves. The difference is not only too large but also in the wrong direction to be explained by centre-of-mass corrections to the Rutherford cross-section in the laboratory. The probable explanation is that a shift in the beam position on the target (or alternatively, a difference in the position of the thickest part of the target) from one target to another can seriously affect the yield detected in the 30° detector while leaving the number of particles scattered into the 85.8° detector relatively unchanged. For example, in the present geometry a shift in the beam spot of 0.04 inches would give a relative change in the ratio of about 18%.

The solid-state counter on the image plane of the spectrograph was used to determine the best charge states of the scattered ions with which to do the experiments. This counter (and the two in the target chamber) had about 50-100 volts bias applied. The pulses from the counter were passed through a discriminator to reject α-particle pulses from such reactions as $O^{16} + C^{12} \rightarrow \alpha + Mg^{24}$. The reason that such discrimination is possible is that

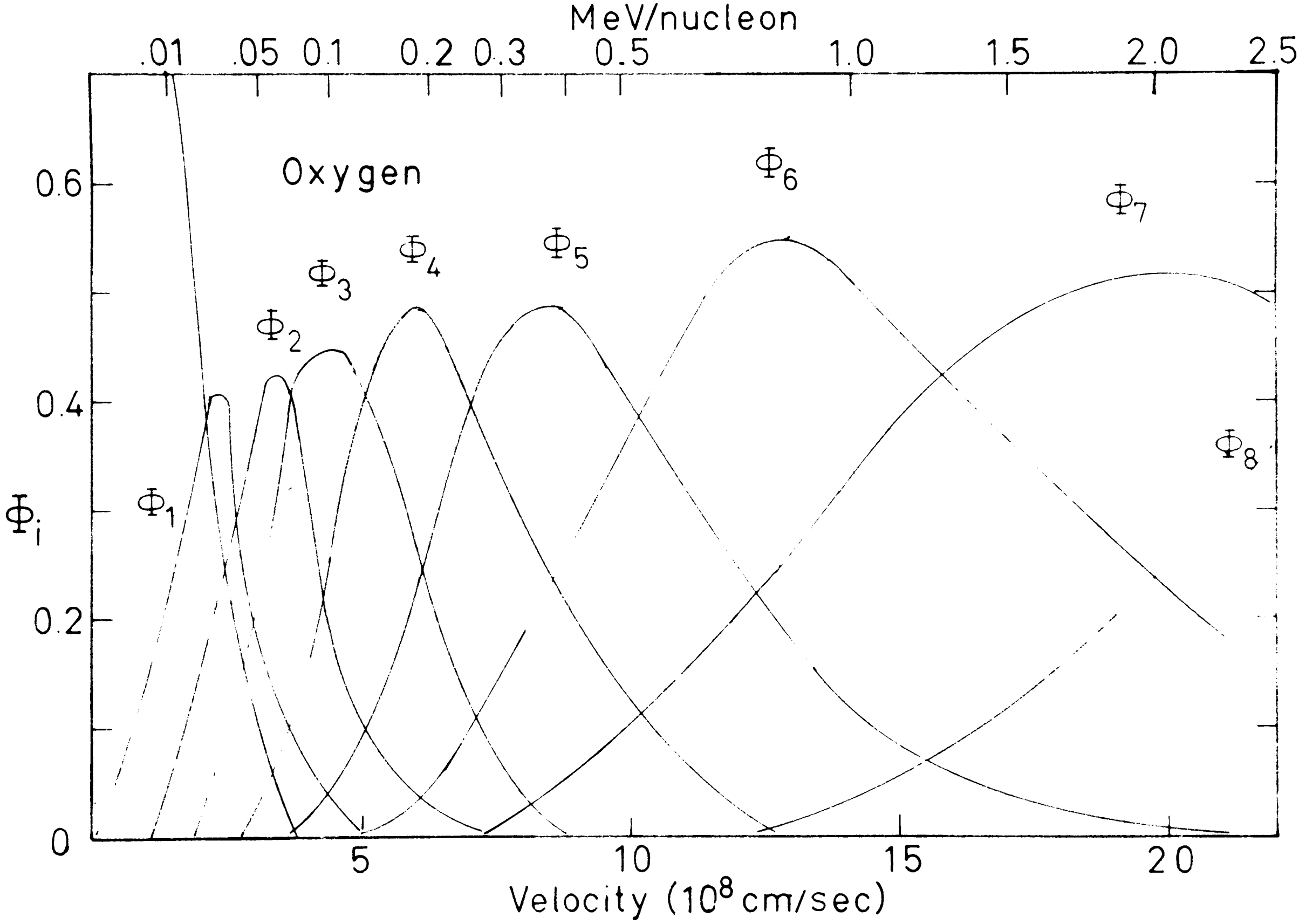
only very low energy α-particles will be bent around the magnet at fields appropriate for the analysis of the O^{16} ions. Table 3.2 lists the charge state distribution for 35.6 MeV O^{16} ions scattered from the Fe^{54} target. Zaidins (Zai 64)

T A B L E 3.2

The charge state populations for 19.3 MeV O^{16} ions emerging from the target.

Charge state	Relative Population	
	Experimental	Zaidins
5	0.08 ± 0.01	0.07
6	0.50 ± 0.03	0.44
7	0.34 ± 0.02	0.41
8	0.08 ± 0.01	0.07

has compiled curves of equilibrium charge state populations as a function of ion velocity for ions up to neon. Figure 3.2 gives his curves of the O^{16} charge state distributions and Table 3.2 also gives the relative populations obtained


MeV/nucleon
.01
.05
0.1
0.2
0.3
0.5
1.0
1.5
2.0
2.5
Oxygen
Φ_1
Φ_2
Φ_3
Φ_4
Φ_5
Φ_6
Φ_7
Φ_8
Φ_i
0
0.2
0.4
0.6
5
10
15
20
Velocity (10^8 cm/sec)

from these curves for 19.3 MeV ions (an ion velocity of 15.5×10^8 cm/sec). This energy is the 90^o scattered energy of the 35.6 MeV incident beam. The agreement is satisfactory considering that no great pains were made to make accurate charge state populations measurements. Further implications of Zaidins' curves will be discussed in subsection 4.1. 2.

Charge states 6^+ and 7^+ were used in the experiments. By a suitable choice of magnet field it was possible in the case of Cr^{52} and Fe^{54} to record both the inelastic and elastic groups on the nuclear emulsion at the same time. In the case of Ti^{50} a different procedure was followed. Because $\Delta E/E$ for Ti^{50} is as large as 7.3% it was felt that it would be safer to record the elastic and inelastic groups separately on different plates. Each run was monitored by recording the spectrum observed in the semiconductor detector at 85.8^o in the target chamber.

To investigate the solid angle variation of the spectrograph over the length of the nuclear emulsion plate a 10 MeV proton beam scattered from a 50 $\mu g/cm^2$ Pb^{208} target on a carbon backing was recorded at different positions on the plate by varying the magnet field. The time of the run at each field setting was monitored by a similar arrangement

to that used for the Ti^{50} experiments, with the exception that the monitor counts were only scaled. The variation of the solid angle was found to be zero to an accuracy of 2%.

3.1.5. Transfer Reactions. A possible reaction mechanism which may occur is the transfer to the target or pickup from the target of a nucleon or α-particle cluster by the O^{16} ions. It turns out that in general only one of the possibilities which are available through this mechanism will have the correct momentum to be bent around the magnet for the selection of the 6^+ or 7^+ O^{16} charge state. There are very few measurements of this type of reaction for heavy ions below the Coulomb barrier available (Tot 63) and no sign of any groups which could be associated with this type of reaction were observed. Below the Coulomb barrier this type of reaction will be strongest for backward angle scattering.

3.2. $Ce^{140,142}$, $Nd^{142-148}$, $Sm^{144,148,150}$, Nd^{143}.

The even-even nuclei $Ce^{140,142}$, $Nd^{142,148}$ and $Sm^{144,148,150}$, and the odd nucleus Nd^{143} were Coulomb excited using charge five and charge six O^{16} ions of energies from 31 MeV to 45 MeV. The probability for excitation was determined by measuring the yield of gamma rays in coincidence with backscattered O^{16} ions (Ecc 62). These

ions were detected in an annular semi-conductor counter placed near 180° to the incident beam direction such that the beam passed through the hole in the counter. Gamma rays were detected in a 3 inch by 3 inch NaI(Tl) crystal at 45° to the incident beam direction. The gamma ray spectrum was recorded in fast-slow coincidence with the backscattered ions.

3.2. 1. Oxygen Beams. Charge five and charge six O^{16} beams from the tandem accelerator were passed through the 90° analysing magnet determining the energy to within 50 keV. This magnet was calibrated using the (p,n) threshold in Al^{27} at 5.79 MeV. Beam currents of up to 0.1 μa were used in the experiments, focussed into a spot about 0.2 cm in diameter. Immediately in front of the target was a liquid nitrogen cold trap to prevent grease from O-rings contaminating the targets and the small amount of carbon blacking found on the targets after long runs showed that the trap was fairly successful.

3.2. 2. Targets. The targets were made at Aldermaston by directly depositing the separated isotopes from a mass separator on 0.003 inch high purity cobalt foil (subsection 3.1. 2.). Only an upper limit on the target thickness

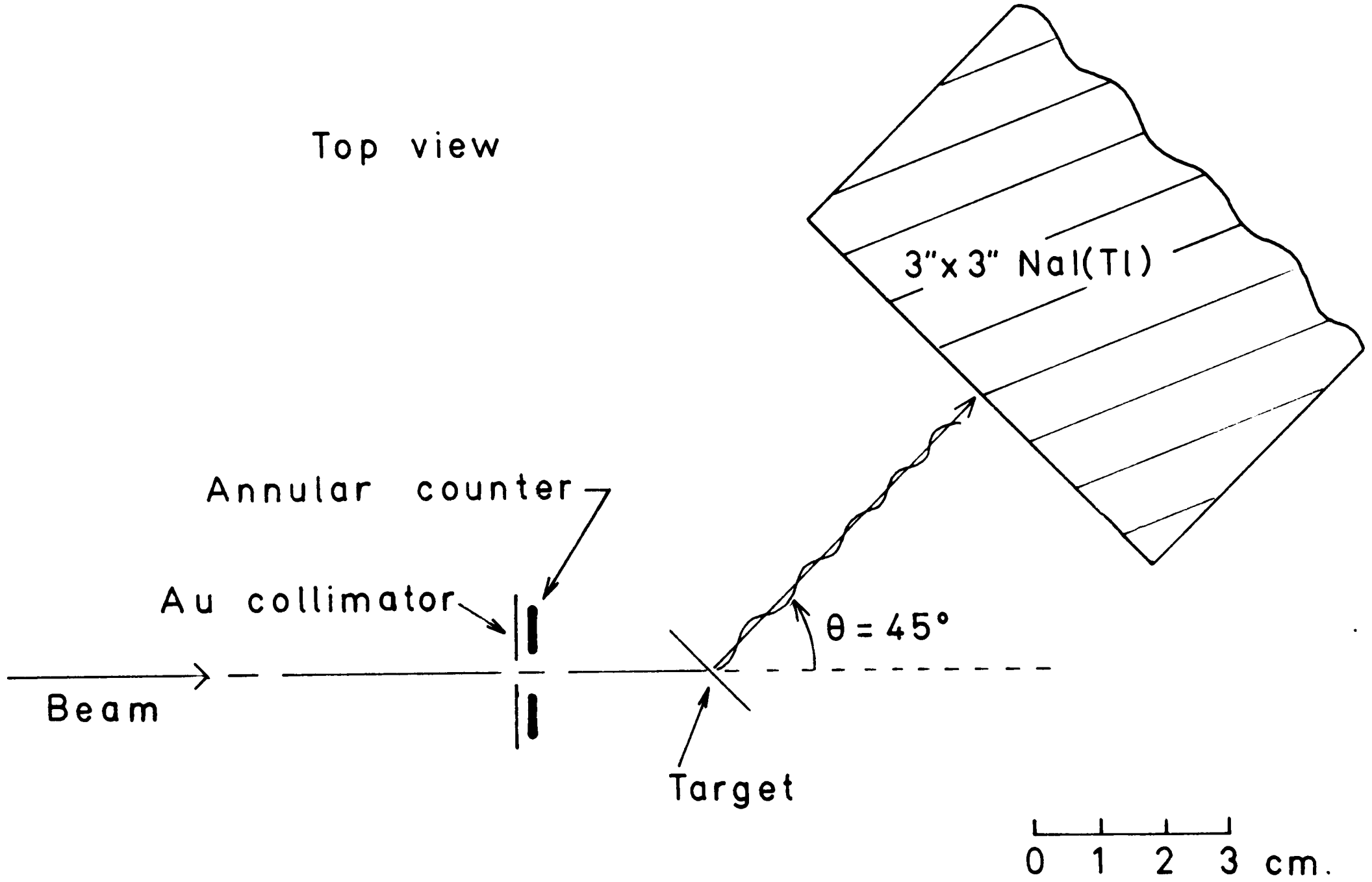
can be determined from the amount of charge collected from the separator, and in general the targets never exceeded 200 $\mu g/cm^2$. The area of the target spot was approximately 0.06 cm^2.

3.2. 3. Detectors. An annular Au-Si surface barrier detector was used to detect the backscattered O^{16} ions. The counters were made by the Special TechniquesGroup at Aldermaston of 1000-1500Ω-cm resistivity silicon with approximately 60 $\mu g/cm^2$ of gold on the surface. The gold annulus had an inside diameter of $\frac{5}{32}$ inch and an outside diameter of $\frac{5}{8}$ inch. A bias of - 20 to - 30 volts was normally applied to the gold annulus.

Gamma rays were detected in a 3 inch by 3 inch NaI(Tl) crystal coupled to an EMI 9578B photomultiplier tube. The best resolution obtained was 9% for the 661 keV gamma ray of Cs^{137} using the dynode chain described in subsection 3.2. 4 and taking the pulse from the second last dynode.

3.2. 4. The Experiment. Figure 3.3. shows the experimental arrangement used. The target chamber is a cylinder with an outside diameter of 4.0 inches with a $\frac{1}{16}$ inch thick brass wall. The semi-conductor detector was situated on a movable mount in order that its distance from the target

Fig. 3.3


Top view
3"x 3" NaI(Tl)
Annular counter
Au collimator
θ = 45°
Beam
Target
0 1 2 3 cm.

could be changed. Generally the counter was placed from 2.5 cm to 2.75 cm away from the target except for the Ce^{140} and Sm^{144} experiments where it was moved to a distance of 1.25 cm. A gold foil with a $^3/_{32}$ inch hole was placed behind the counter to prevent the incoming beam from hitting the counter.

The NaI(Tl) crystal was situated at 45^o to the incident beam direction and the face was positioned 6 cm from the target. The angle of 45^o was chosen because at this angle the angular distribution of gamma rays from a 2^+ state to a 0^+ state is a maximum. Thus, as well as achieving a maximum count rate, the results are insensitive to any minor misalignment of the target and crystal. The neutron and gamma ray background in the experimental room was found to be very low and consequently the crystal was not shielded.

The target was placed at 45^o so that the plane of the target was parallel to the face of the crystal. This arrangement minimizes gamma ray absorption by the target backing.

Figure 3.4 shows a block diagram of the electronic apparatus. Pulses from the semiconductor detector are fed into a charge-sensitive preamplifier to minimize pulse height changes during the experiments (Bla 61). If a

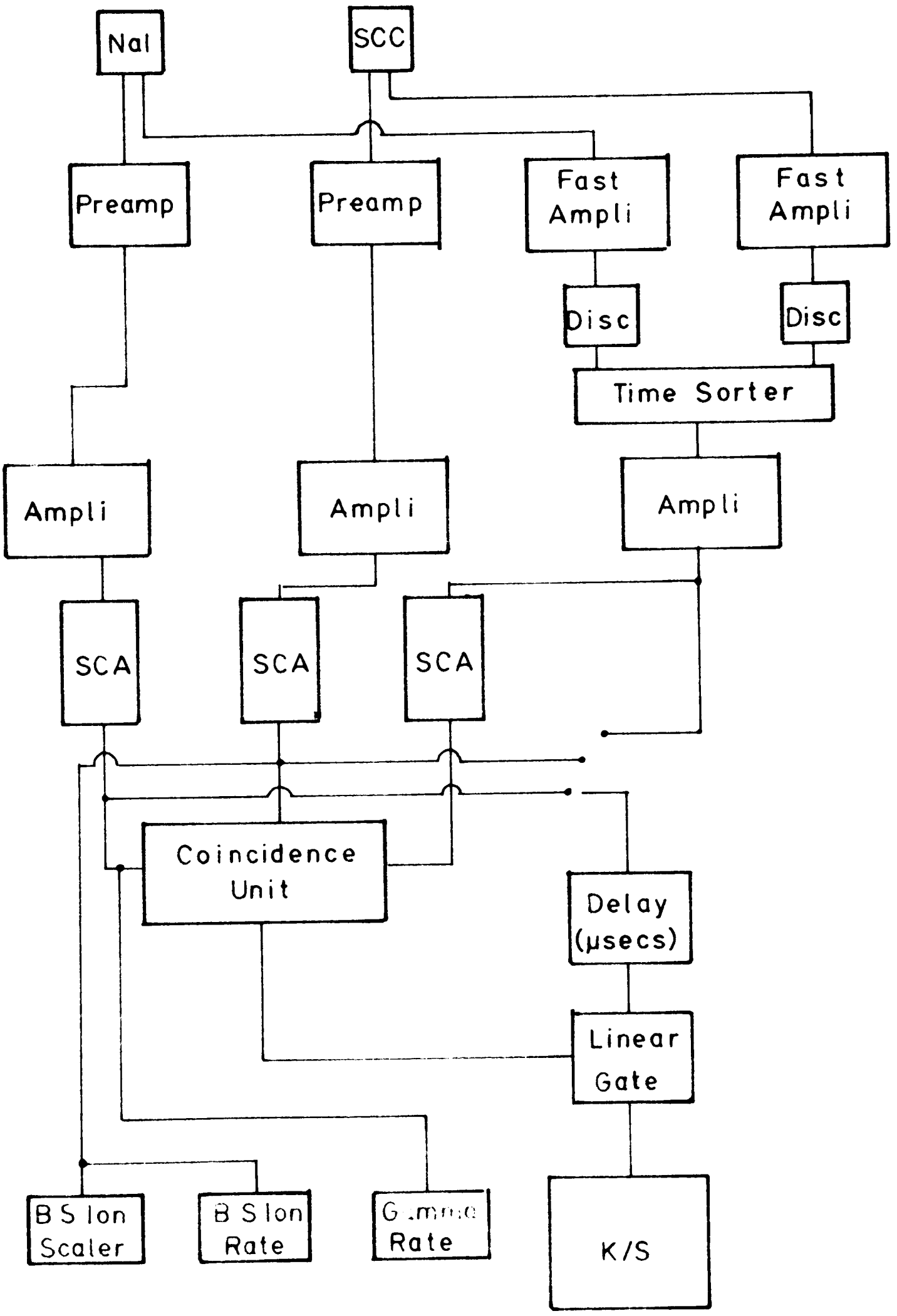

Nal
SCC
Preamp
Preamp
Fast Ampli
Fast Ampli
Disc
Disc
Time Sorter
Ampli
Ampli
Ampli
SCA
SCA
SCA
Coincidence Unit
Delay (μsecs)
Linear Gate
B S Ion Scaler
B S Ion Rate
Gamma Rate
K/S

Fig. 3.4

voltage preamplifier were used the change in counter bias, due to an increase in the voltage drop across the counter load resistance associated with the observed increase in detector leakage current during long experiments (occasionally from 3 μa - 10 μa in several hours), would result in a change in detector pulse height.

The pulses from the preamplifier, with rise times of the order of 10 nsec. are then fed into the slow and fast sides of the coincidence circuitry.

The problem of obtaining a linear pulse and a fast pulse from the NaI(Tl) crystal is not as straightforward because the rise times of these pulses is of the order of 30-40 nsec. at the photomultiplier anode. A dynode chain with equal resistors throughout (51 kΩ) except between cathode and first dynode (175 kΩ) was used. The linear pulse was taken from the second last dynode and the anode pulse was used for the fast side.

The dynode and anode pulses are fed into a system of amplifiers and the fast-slow coincidence circuit as shown in the figure. The dynode pulses are fed through linear amplifiers and into the input of a triple coincidence circuit. The pulses from the semiconductor detector are scaled and recorded after passing through a single-channel

analyser adjusted to select only the pulses corresponding to O^{16} ions scattered from the target isotope. This procedure is possible because the targets are thin to O^{16} ions (see Figure 4.2). These pulses are also fed into the coincidence unit. The anode pulses are passed through wide-band line amplifiers so that all the pulses of interest are limiting fairly hard, thus having fast and fairly equal rise times. These pulses along with semiconductor pulses are then fed into a time sorter (time-to-pulse height converter) and the delay in the semiconductor side is adjusted to give a maximum pulse height out. The time-sorted output is fed into the coincidence unit. A triple coincidence provides an output pulse which opens a gate circuit allowing the storage of any spectrum (gamma ray, O^{16} ions) in a multichannel pulse height analyser. Rate-meters record the gamma ray and backscattered ion rates. The resolving time of the triple coincidence circuit was usually about 35 nsec.

The discriminators in the coincidence unit have adjustable paralysis times. These were set to 5 μsec so that the number of lost coincidences could be calculated (subsection 4.2. 2).

In each experimental run a straight gamma ray spectrum,

a straight ion spectrum, and a coincident gamma ray spectrum were recorded. The number of backscattered ions detected was recorded with the coincident spectrum.

The methods of analysing the data are discussed in Section 4.2.

3.3. The "Reorientation" Effect: Cd^{114}, Sm^{148}, Sm^{150}.

The experimental problem of observing the "reorientation" effect is the problem of detecting a difference between the experimental Coulomb excitation and the first-order theoretical calculation of the order of 10% to 20%. One of the chief uncertainties which militate against detecting this difference is the imprecise knowledge of the reduced transition probability B(E2). These are generally known absolutely to an accuracy of about 10% and in many cases have been obtained from Coulomb excitation experiments with heavy ions from a comparison with the first-order perturbation calculations, and thus contain a contribution from the effect one is looking for.

One way to minimize this uncertainty is to compare the excitation probabilities for various projectiles (Dou 63). Ideally one chooses ions which are as different as possible, say protons and oxygen ions. Unfortunately the problem

of barrier penetration with protons, even at energies well below the Coulomb barrier, makes the choice of protons unfavourable (Byg 64). In the present work S^{32} and O^{16} ions were used to Coulomb excite Cd^{114}, Sm^{148} and Sm^{150}, and the excitation probability was determined by detecting gamma rays in coincidence with backscattered ions. Except for a few differences the experimental techniques were the same as described in Section 3.2.

3.3. 1. Sulphur Beams. Sulphur ions were produced from H_2S gas in a capacitive-coupled rf. ion source. Two other gases, SF_6 and SO_2, were also tried, but without success. The former gas produces intense fluorine beams, however, and the production of O_2^- ions was observed from the latter gas. It was found that sulphur deposited on the ion source and that thirty-six hours was the normal period before the anode needed cleaning.

The accelerated ions are passed through the 90^o analysing magnet as described in subsections 3.1. 1 and 3.2. 1. No beams corresponding to the acceleration of S^{34} ions were observed. Also, it was not possible to determine if the ions from the injector were really S^- or HS^-.

In preliminary studies of the sulphur beams charge

states from 5^+ to 8^+ were observed. Charge states 5^+ and 6^+ were the most prolific and charge 8^+ was down in yield by a factor of ten.

Great care must be exercised in setting the centre terminal voltage of the accelerator for choosing the desired charge state because of the prominence and proximity of "post-stripped" beams. These are ions which, after being accelerated in the second stage of the tandem accelerator with a charge q, lose an electron (or electrons) in the flight tube between the end of the accelerator and the bending magnet. It was found that for the bending magnet field set to select the charge state q lowering the centre terminal voltage by about 100 kV resulted in the magnetic analysis of charge q-2 accelerated ions, which had been "post-stripped" to charge q-1. The separation between the desired beam and the "post-stripped" beam decreased as the charge state increased. Fortunately the energies of these two beams are very different and the semiconductor counter detecting the backscattered ions can be used to discriminate against the lower energy beam.

The experimental results were collected during three sets of runs. Between the last two new High Voltage Engineering Corporation inclined field accelerator tubes

were installed in the tandem accelerator. Previously with the ordinary tubes the upper limit on the beam current had been fixed by centre terminal loading and with the new tubes beam currents of up to 0.3 μa of charge seven sulphur ions of 52 MeV were achieved without loading, an increase of a factor of five. In the latter run the beam energy was determined by calibrating the analysing magnet using the H^2 (O^{16},n) threshold at 14.55 MeV O^{16} energy.

3.3. 2. Targets. It is clearly very desirable to have as highly enriched a target as possible. Thin targets are an advantage in that the analysis of the results is easier, and in the case of thin targets, the thinner they are the less accurate need be the knowledge of the thickness.

The Cd^{114} target was made by the electrodeposition of 97% enriched isotope on 0.003" cobalt foil and a thickness of 62 μg/cm^2 was determined by weighing.

The $Sm^{148,150}$ targets were made as described in subsection 3.2. 2. To determine the thickness of the targets the shift in the spectrum of the backscattered ions from the cobalt backing produced by the target layer was measured during the experimental runs (Figure 3.5). In determining the thickness the energy loss of the ions in the targets

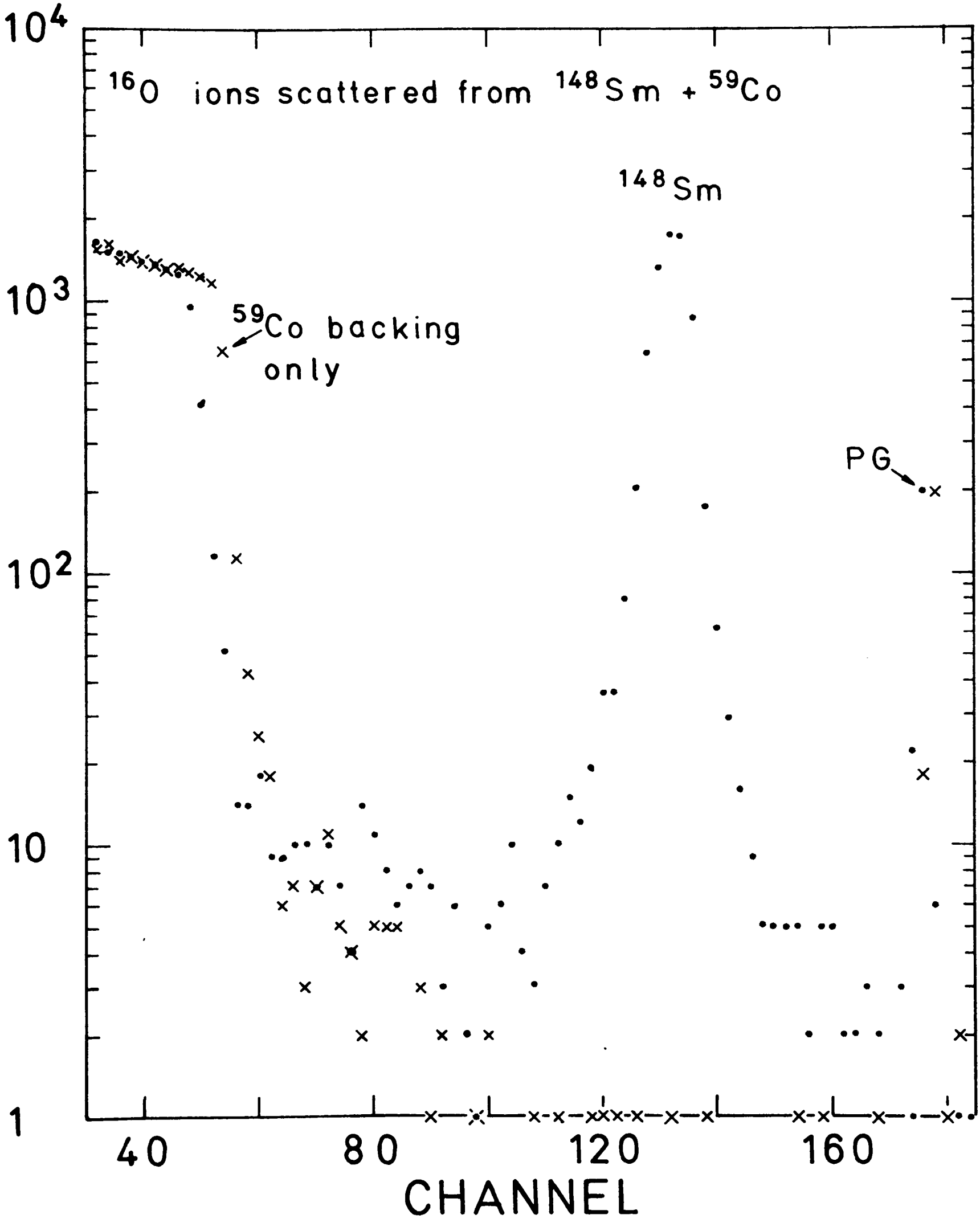

10^4
10^3
10^2
10
1
^{16}O ions scattered from ^{148}Sm + ^{59}Co
^{148}Sm
^{59}Co backing only
PG
40
80
120
160
CHANNEL

Fig. 3.5

was determined from the stopping powers of heavy ions measured by Booth and Grant (Boo 65). The thicknesses obtained during the first two runs were, for Sm^{150}, 38 $\mu g/cm^2$ (S^{32} ions), 44 $\mu g/cm^2$ and 30 $\mu g/cm^2$ (O^{16} ions); and for Sm^{148}, 85 $\mu g/cm^2$ and 115 $\mu g/cm^2$ (O^{16} ions). The Cd^{114} target thickness was also determined this way, and the results were 57 $\mu g/cm^2$ (S^{32} ions), 60 $\mu g/cm^2$ and 82 $\mu g/cm^2$ (O^{16} ions). During the measurements on $Sm^{148,150}$ it was noticed that the slope of the front edge of the backscattered spectrum from the cobalt backing alone was occasionally steeper than when the ions had scattered through the target layer. This can be attributed to non-uniformity of the target or to the beam partly missing the target.

In the third run a new Sm^{148} target with a much larger surface area ($\approx$ 0.15 cm^2) having a thickness of 73 $\mu g/cm^2$ (O^{16} ions) was used. A repeat of the thickness measurement of the Sm^{150} target gave 80 $\mu g/cm^2$. In both these cases the slopes of the front edges of the spectrum of ions backscattered from the cobalt were the same. The uncertainty in the target thickness, which affects the calculated excitation probability, will be discussed in subsection 4.3. 3.

3.3. 3. Detectors. The detectors used were as described in subsection 3.2. 3 except that in the third run a Nuclear Enterprise integrally mounted 3 inch by 3 inch NaI(Tl) crystal on an EMI 9531 photomultiplier tube was used. In all three runs a different dynode chain was used from that described in subsection 3.2. 4. The essential difference was that the last three resistors in the chain are 75 kΩ, 100 kΩ and 125 kΩ to prevent space charge saturation.

3.3. 4. The Experiment. With a few exceptions the experimental details are as in the previous section. One of the exceptions is the method of obtaining fast and linear pulses from the photomultiplier tube. Only pulses from the anode are used and they are fed into the primary winding of a small transformer with a 5:1 turns ratio. Rise times of the order of 50 nsec were achieved on pulses from the secondary winding. These pulses are amplified and limited to achieve faster rise times. The linear pulse is taken from the primary. A similar system was also incorporated into the semiconductor counter side.

Because the background gamma ray count rate was considerably higher when bombarding the targets with O^{16} ions than with S^{32} ions (by a factor of ten to twenty) a radioactive source with a gamma ray of energy higher than the desired gamma ray was placed near the NaI(Tl) crystal

during the S^{32} experiments in order to make the gamma detection rate in the crystal the same as in the O^{16} experiments. This procedure eliminates the uncertainties of lost coincidences due to dead times in the electronic apparatus.

A smaller thin walled spherical target chamber made of 0.015 inch copper with a 3 inch outside diameter was used, permitting the NaI(Tl) crystal face to be 4.5 cm from the target.

During the first two sets of runs the annular semiconductor detector was 2.70 cm. from the target and subtended a solid angle in the laboratory from 161.77° to 171.34°, giving a mean angle of 165.64°. In the third set of runs the counter was 3.2 cm. from the target, subtending a solid angle from 164.72° to 172.43° with a mean angle of 167.70°.

C H A P T E R 4

EXPERIMENTAL RESULTS

4.1. Ti^{50}, Cr^{52} and Fe^{54}.

This section presents the results of the magnetic analysis of O^{16} ions scattered from the targets of Ti^{50}, Cr^{52} and Fe^{54}.

4.1.1. Experimental Probabilities. The experimental probability for Coulomb excitation of the nuclear state is the ratio of the number of inelastically scattered O^{16} ions exciting the state to the number of elastically scattered ions. Figure 4.1 shows the momentum spectrum of charge six O^{16} ions scattered from the Fe^{54} target when bombarded by a 38.1 MeV charge five beam. The beam energies quoted in this section have been corrected for energy loss in the target using stopping powers measured by Porat and Ramavataran (Por 61). Because the targets are extremely thin a good approximation is to use an effective beam energy as the energy at which Coulomb excitation takes place. This effective energy is the beam

energy loss the energy loss in one-half the target thickness. The same energy loss correction for half the target of 60 keV has been applied to all targets. The nuclear emulsion was scanned in 0.25 mm. wide strips; each point on the inelastic peak in the figure represents the sum of ten adjacent scanned strips, whereas the points on the elastic peak represent every fifth scanned strip. The smooth curve has been fitted by eye to the elastic peak and then the curve fitted to the inelastic peak was obtained from the elastic, taking into account the change in dispersion of the spectrometer across the emulsion.

In determining the number of tracks in the inelastic group the background under it was assumed to be a linear interpolation of the background on both sides.

Table 4.1 lists all the results obtained for the three nuclei for various bombarding energies and charge states of the scattered ions. One important correction (subsection 4.1. 2) has been applied and the errors quoted contain both statistical and non-statistical uncertainties.

An interesting non-statistical error is the slight discrepancy in the number of tracks counted when the same inelastic group was scanned by different people. Usually

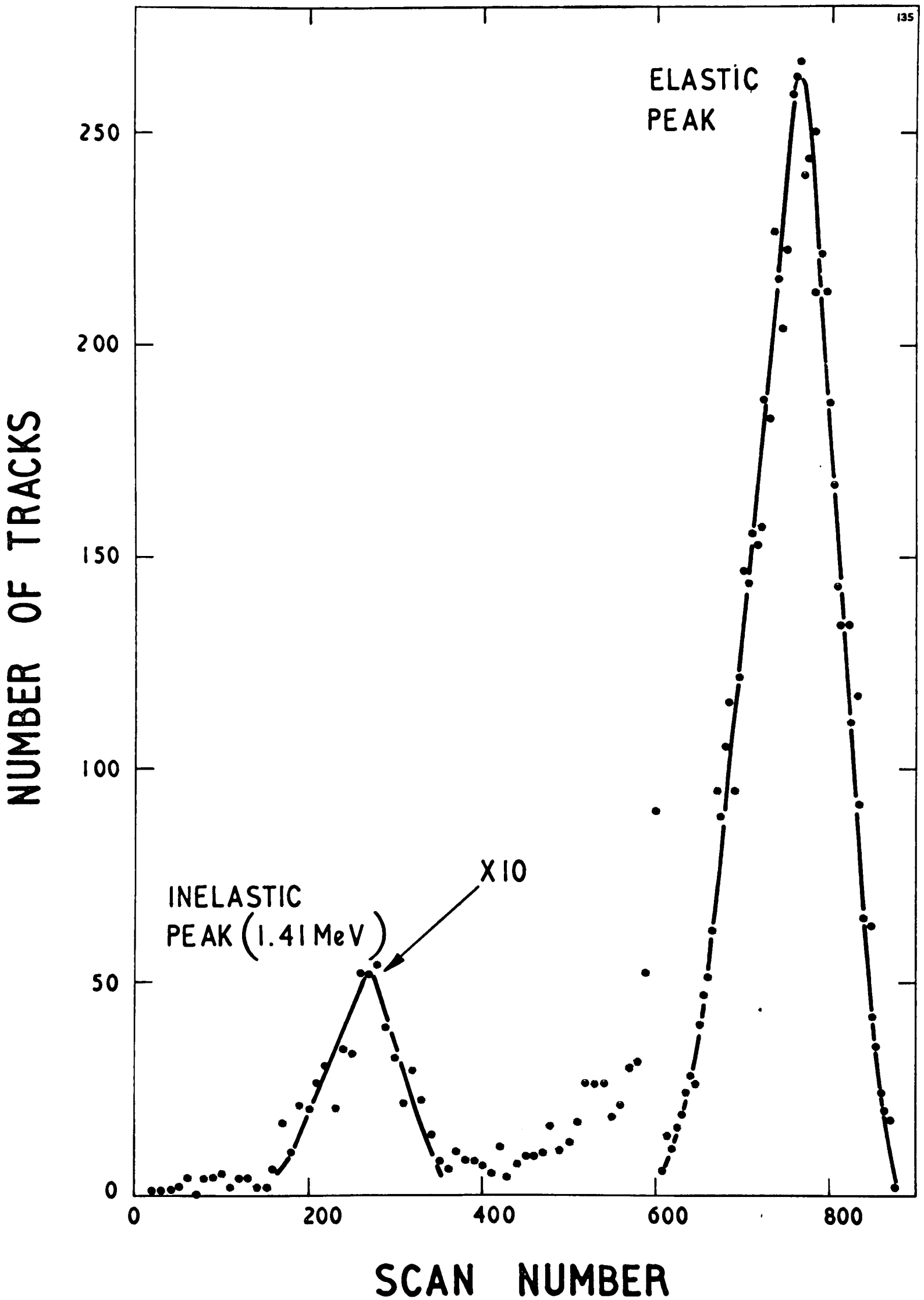

ELASTIC
PEAK
INELASTIC
PEAK (1.41 MeV)
X10
NUMBER OF TRACKS
SCAN NUMBER
0
50
100
150
200
250
0
200
400
600
800

Fig. 4.1

TABLE 4.1

Column 5 shows the excitation probability. The calculated probability in column 6 incorperates the single-particle transition probability shown in column 7, and column 8 gives the ratio of the experimental transition probability to the single-particle value.

1	2	3	4	5	6	7	8
Target	Energy of 2^+ State (MeV)	Bombarding O^{16} Energy (MeV)	Scattered O^{16} charge state	Experimental probability (%)	Calculated Probability	$B(E2)_{sp}$ $10^{-2}e^2b^2$	$\frac{B(E2)_{exp}}{B(E2)_{sp}}$
Ti^{50}	1.56	31.8	6^+	0.48 ± 0.06	0.098	0.547	4.9 ± 0.6
		32.8	6^+	0.49 ± 0.06	0.121		4.1 ± 0.5
Cr^{52}	1.43	33.8	6^+	1.03 ± 0.08	0.110	0.568	9.4 ± 0.7
		35.6	6^+	1.27 ± 0.07	0.152		8.3 ± 0.4
		35.6	7^+	1.21 ± 0.07	0.152		8.0 ± 0.5
Fe^{54}	1.41	35.6	6^+	0.98 ± 0.08	0.112	0.607	8.7 ± 0.7
		35.6	7^+	1.01 ± 0.08	0.112		9.0 ± 0.7
		38.1	6^+	1.32 ± 0.08	0.172		7.7 ± 0.5
		38.1	6^+	1.60 ± 0.24	0.172		9.3 ± 1.4
		40.7[a)]	6^+	1.23 ± 0.13	0.275		4.9 ± 0.5

a) This energy is above the Coulomb barrier.

the discrepancies disappeared with background subtraction, but not always. This difficulty was a result of the small number of tracks per scanned strip and of the shortness of the tracks ($\approx$ 12 μm) making identification tedious. From a comparison of the results of different scanners a personnel error of $\pm$5 counts for each inelastic group has been assigned. This is only significant for the Ti^{50} results and introduces there an error of 5%.

4.1. 2. Charge State Correction. In determining the experimental probability it is important to know whether or not the relative charge state population of the inelastically scattered ions differs from that of the elastically scattered ions. If the assumption that charge equilibrium has been reached is made, then Figure 3.2 suggests that at the emergent ion velocities of this experiment ($\approx$ 15.0 x 10^8 cm/sec) the experimental probability for exciting the first excited state is high by 6% when making measurements on the 6^+ charge state and low by 6% when making measurements on the 7^+ charge state. This is probably quite accurate for Cr^{52} and Fe^{54}, but because the velocity is somewhat lower for ions scattered from the Ti^{50} target, the charge state populations in this case may be near the

maximum of the 6^+ charge state curve and the correction smaller.

It is difficult to be certain that equilibrium has been reached for targets as thin as those used here. Steiger (Ste 63) finds that charge state equilibrium for heavy ions is practically attained for target thicknesses of 25 $\mu g/cm^2$. Almqvist et al (Alm 62) and Litherland et al (Lit 63) imply that equilibrium is achieved for even thinner targets ($\approx$ 8-13 $\mu g/cm^2$). Experimental evidence of Reynolds et al (Rey 55) and Hubbard and Laver (Hub 55) suggest that a similar thickness is sufficient to achieve equilibrium. However, Heckman et al (Hec 63) suggest that a thickness of 50 $\mu g/cm^2$ is required for equilibrium to be reached with oxygen ions. The results of the present work in Table 3.2 seems to indicate that for the rather special starting conditions of this experiment (special because only those ions which have been involved in a nuclear collision are detected) the charge state populations correspond quite closely to equilibrium conditions. Hence the correction to the experimental probability used is that derived from Zaidins' curves; i.e., $(-6\pm4)\%$ for the 6^+ charge state measurements and $(6\pm4)\%$ for the charge 7^+ measurements.

4.1. 3. Calculated Probabilities. In order to extract B(E2) values from the experimental probabilities the first-order theory excitation probability P of subsection 2.1. 7

$$P = \frac{d\sigma_{E2}(\theta_{E2})/d\Omega_{E2}}{d\sigma_{R}(\theta_{R})/d\Omega_{R}} \qquad (4.1)$$

was calculated. The calculations were carrried out at the effective O^{16} beam energy (subsection 4.1. 1); this approximation is certainly adequate for such thin targets because a numerical integration of the Coulomb excitation probabilities over the much thicker Sm targets showed that the approximation was well justified even in the latter case. The differential Coulomb excitation cross-sections $d\sigma_{E2}(\theta_{E2})/d\Omega$ were calculated in the semi-classical approximation ($\eta = \infty$) but were symmetrized according to the prescription of Alder et al (Ald 56)(subsection 4.1. 5). Biedenharn and Brussaard (Bru 63) have shown, however, that if one uses a different symmetrization procedure then the differential cross-section for E2 excitation calculated in the semi-classical approximation agrees very well with the exact quantum mechanical calculation down to $\eta_1 = 1.0$.

In the present experiments $\eta_i \simeq 20$ and the two symmetrization approaches lead to nearly the same result. From Alder et al. the symmetrized η is

$$\eta \rightarrow (\eta_i \eta_f)^{\frac{1}{2}} \simeq \eta_i (1-\rho)^{-\frac{1}{4}} \simeq \eta_i (1+\frac{\rho}{4}) \qquad (4.2)$$

for η_i large and ρ small. The Sommerfeld number η_f has the initial ion velocity v_i replaced by the final relative velocity v_f and

$$\rho = (1 + \frac{A_1}{A_2}) \frac{\Delta E}{E} \qquad (4.3)$$

where ΔE is the excitation energy and E is the bombarding energy. From Biedenharn and Brussaard the symmetrized η is

$$\eta \rightarrow \left\{ \frac{2(\eta_i^2+1)(\eta_f^2+1)}{(\eta_i^2+1)^{\frac{1}{2}} + (\eta_f+1)^{\frac{1}{2}}} \right\}^{\frac{1}{3}}$$

$$\simeq \eta_i (1-\rho)^{-\frac{1}{3}} \simeq \eta_i (1+\frac{\rho}{3}) \qquad (4.4)$$

Thus the fractional difference in the two methods of symmetrization is $\rho/12$. For a typical case, 35 MeV O^{16}

ions on Cr^{52}, ρ is 0.0535 and consequently it is perfectly adequate to use the symmetrization procedure of Alder et al. for the present calculations. The differential Rutherford cross-section $d\sigma_R/d\Omega_R$ are not symmetrized, however, but incorporate V_1.

The calculations take into account the fact that the centre-of-mass angle of inelastic scattering θ_{E2} and of elastic scattering θ_R are different. It was assumed that the centre-of-mass solid angles $d\Omega_{E2}$ and $d\Omega_E$ are the same because the correction for their difference amounts to only 0.3%.

The calculated probabilities listed in Table 4.1 also include the single-particle reduced transition strengths $B(E2)_{sp}$ given in the table (subsection 2.1. 4). Also listed are the enhancements, $B(E2)_{exp}/B(E2)_{sp}$, of the experimental B(E2) values over the single-particle values.

It will be noticed that the O^{16} energy of 40.7 MeV is above the Coulomb barrier for Fe^{54} (Figure 3.1) and that the enhancement of the B(E2) value in this case is considerably smaller than the enhancements at the lower bombarding energies. This curious result will be discussed in subsection 5.1. 7.

4.2. $Ce^{140,142}$, $Nd^{142-148}$, $Sm^{144,148,150}$, Nd^{143}.

This section presents the results of the B(E2) measurements on the even nuclei $Ce^{140,142}$, $Nd^{142-148}$, $Sm^{144,148,150}$ and on the odd nucleus Nd^{143}. The gamma ray energy from the first excited state of Sm^{144} has also been determined.

4.2.1. Experimental Probabilities. The probability for Coulomb exciting a nuclear state is the number of gamma rays emitted over 4π sr. divided by the number of coincident back-scattered ions detected in the semiconductor counter. Figure 4.2 shows a typical spectrum of backscattered oxygen ions. This particular example is that for 35.3 MeV oxygen ions on a thin Nd^{148} target deposited on a cobalt backing.

Figure 4.3. shows the direct spectrum of the gamma rays in the NaI(Tl) detector at 45° to the beam direction for the above case. Only the 300 keV gamma ray has been identified as coming from Nd^{148}. Figure 4.4 shows the gamma ray spectrum in coincidence with the ions scattered from the target isotope.

In determining the excitation probability only the number of gamma rays in the photopeak at one angle are

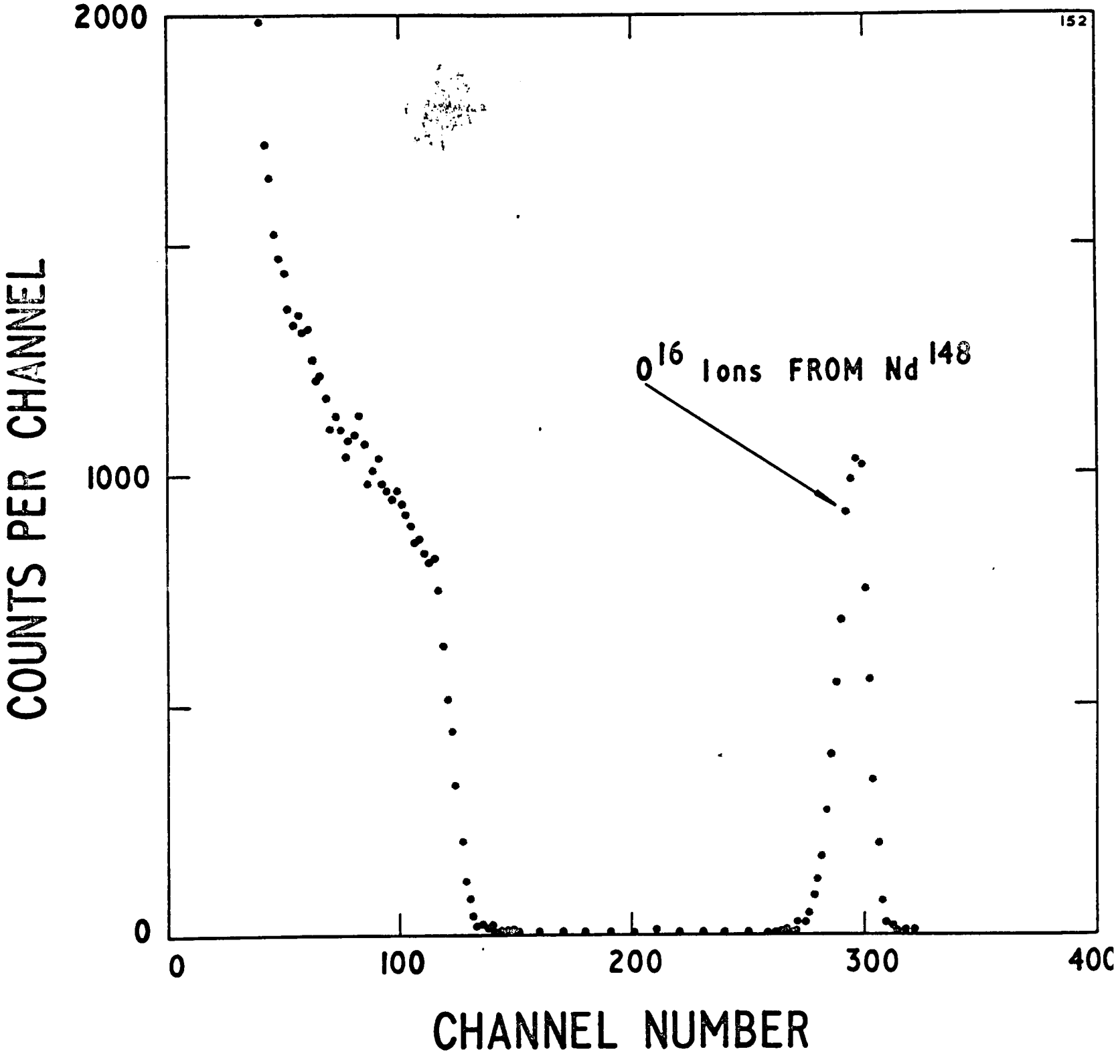

2000
1000
0
COUNTS PER CHANNEL
152
O^{16} Ions FROM Nd^{148}
0
100
200
300
400
CHANNEL NUMBER

Fig. 4.2

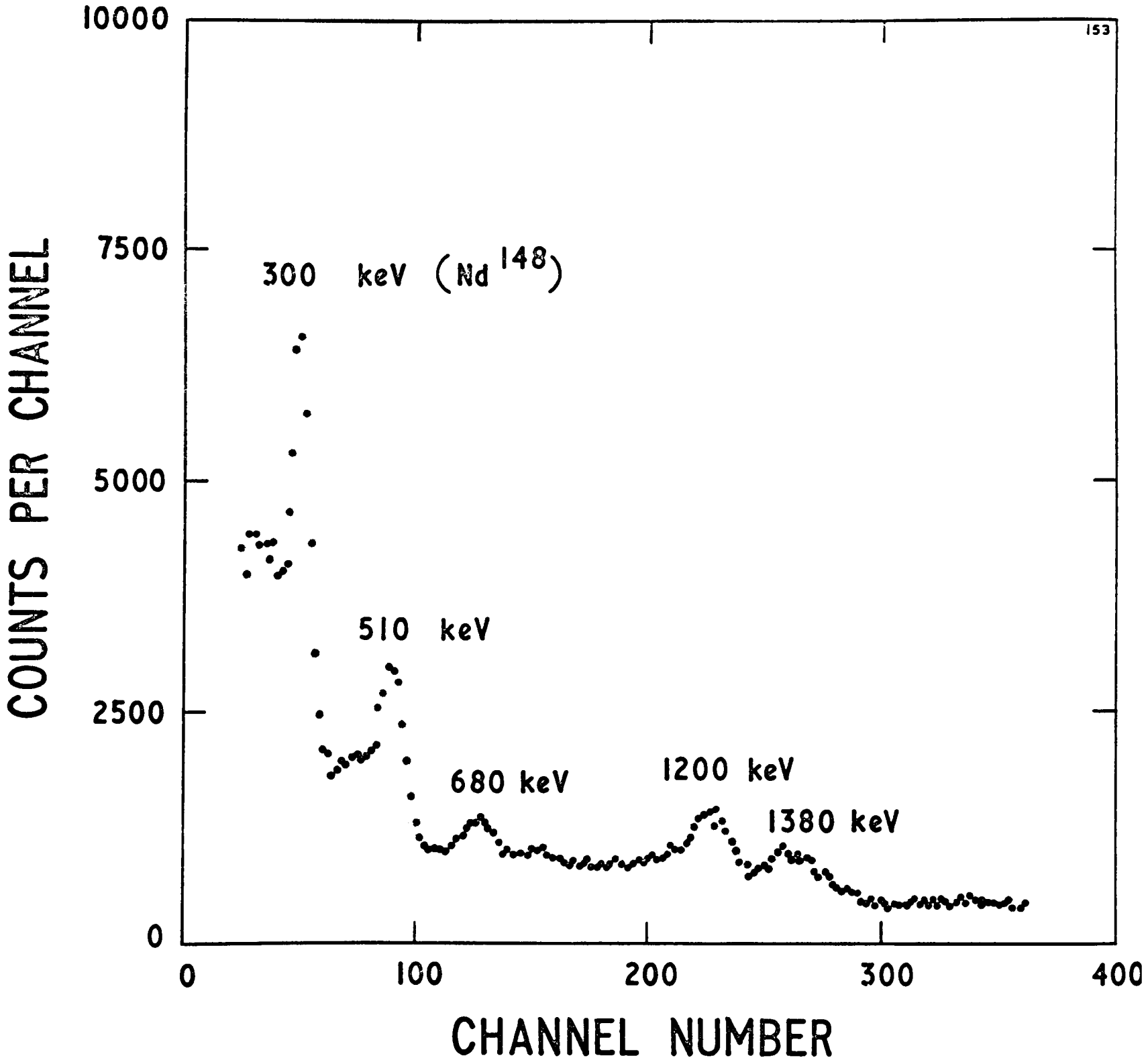

153
10000
7500
5000
2500
0
COUNTS PER CHANNEL
300 keV (Nd 148)
510 keV
680 keV
1200 keV
1380 keV
0
100
200
300
400
CHANNEL NUMBER

Fig. 4.3

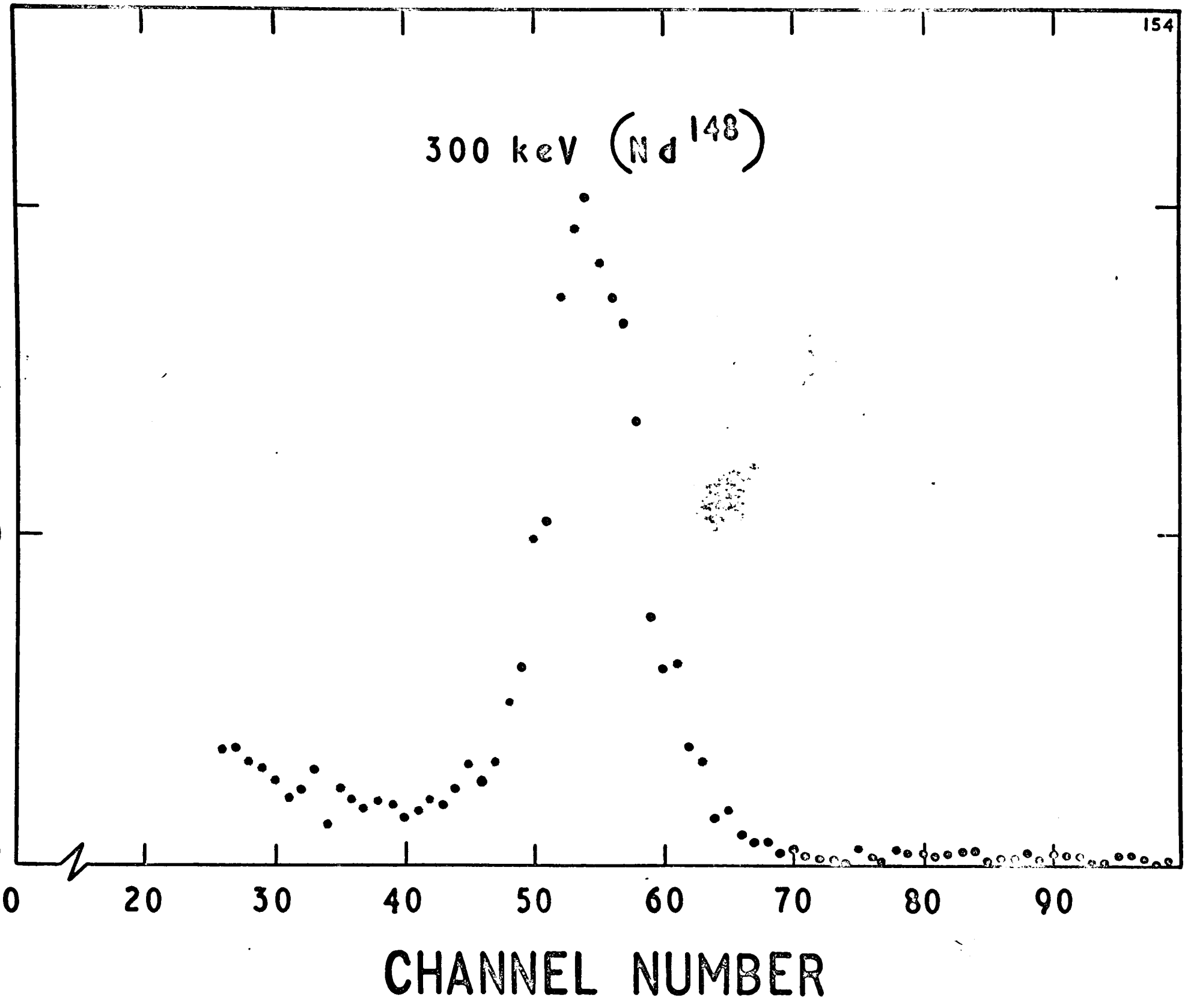

300 keV (Nd 148)
COUNTS PER CHANNEL
200
100
0
0
20
30
40
50
60
70
80
90
CHANNEL NUMBER

Fig. 4.4

detected. Consequently the expression for the experimental probability is

$$R = \frac{1}{N(I)} \left[\frac{N(\gamma)\, a}{e} \right] \frac{1}{W(\theta)} \qquad (4.5)$$

The factor $N(\gamma)$ is the number of gamma rays in the coincident photopeak. It includes corrections for random coincidences and lost coincidences due to dead times in the electronic apparatus. $N(I)$ is the number of backscattered ions counted. The factor "a" corrects $N(\gamma)$ for absorption of gamma rays by the target backing, the walls of the scattering chamber, and the covering of the NaI(Tl) crystal. The factor "e" corrects for both the intrinsic efficiency and the geometrical efficiency of the crystal for detecting gamma rays in the photopeak. $W(\theta)$ is an angular distribution correction and includes as well a geometrical factor accounting for the smearing of the angular distribution by the finite size of both the gamma ray and backscattered ion detectors.

A correction for internal conversion is taken into account when the reduced transition probabilities are determined.

4.2. 2. Determination of the Photopeak. In determining

the net number of gamma rays in the photopeak, the number of gamma rays from random coincidences was determined by a comparison of the background above the photopeak in the coincident spectrum with the same portion in the direct spectrum. The number of these random coincidences was generally very small, usually not exceeding 3% except in the case of the single-closed shell nuclei Ce^{140}, Nd^{142} and Sm^{144} and the odd nucleus Nd^{143} where it was about 30%.

Real coincidences may also be lost due to dead times in the electronic apparatus. Most of the lost coincidences occur in the discriminators of the triple coincidence circuit. However, these units can have preset paralysis times, and using this facility along with a knowledge of the gamma ray rate, an estimate of the losses is easily made. In general they were about 2-5% in the gamma ray discriminator. In one set of experiments, however, the multichannel analyser stored the direct spectrum simultaneously with the coincident spectrum and in this case there were additional losses in the analyser of 4-7%.

4.2.3. Absorption Correction. The absorption coefficients μ for gamma rays were obtained from the tables of Wapstra et al (Wap 59). The absorption coefficients for

brass and cobalt were taken to be the same and the absorption due to the 0.025 inch aluminium covering on the crystal was also included.

Table 4.2 lists the correction for absorption a used, defined by

$$a = \exp\left(\sum_i \frac{d_i}{\mu_i}\right) \qquad (4.6)$$

where d_i is the surface density of the absorber, μ_i is the mass absorption coefficient and the summation is over the different absorbing materials.

TABLE 4.2.

Nucleus	Gamma Ray Energy (MeV)	Absorption Correction a	Efficiency Correction e (h = 6 cm.)	Angular Distribution Correction W(θ)
Ce^{140}	1.596	1.076	0.0101	1.493
Ce^{142}	0.640	1.123	0.0240	1.560
Nd^{142}	1.570	1.080	0.0101	1.570
Nd^{144}	.695	1.120	0.0223	1.568
Nd^{146}	.460	1.147	0.0333	1.545
Nd^{148}	.300	1.190	0.0469	1.518
Sm^{144}	1.60	1.076	0.0101	1.493
Sm^{148}	.551	1.132	0.0273	1.557
Sm^{150}	.334	1.180	0.0432	1.526
Nd^{143}	.74	1.104	0.0212	1.0088

4.2. 4. Efficiency Correction. The number of gamma rays detected in the photopeak depend on both the intrinsic efficiency of a particular size of crystal for detecting the full energy of a gamma ray incident on the crystal face and also on the probability that the gamma ray will be incident on the crystal face. The tables of R.L. Heath (Hea 57) give the efficiencies for gamma ray detection by NaI(Tl) crystals of different sizes and shapes as a function of the distance from a point source of gamma rays. Table 4.2 lists the efficiency correction e. It has been found that it is possible to get efficiencies differing from Heath's values by less than 10% in the laboratory without using extraordinary care.

4.2. 5. The Angular Distribution of Gamma Rays. The angular distribution expression for gamma rays following Coulomb excitation detected in coincidence with ions scattered at 180°, given in subsection 2.1. 6, is modified by several important experimental facts. Firstly, the gamma ray detector has finite size which results in a smearing of the angular distribution anisotropy. For a cylindrically symmetric detector the form of the angular

distribution expression is not changed, but each term in it is multiplied by an attenuation factor Q_k (Ros 53). The Q_k depend on the size of the detector and its distance from the source of gamma rays, and also upon whether the whole spectrum or only the photopeak is included in the determination of the angular distribution. Yates (Yat 65) has calculated the attenuation factors for the $P_2(\cos\theta)$ and $P_4(\cos\theta)$ terms Q_2 and Q_4, for various sizes of NaI(Tl) detectors at a range of distances in the case when either the whole spectrum or only the photopeak is included in the determination of the angular distribution. The calculations agree very well with experimental results (Rei 65; Her 64).

The second factor which affects the angular distribution is that the annular semiconductor counter is not exactly at 180° to the beam direction. This allows magnetic substates M to be populated other than those populated in the case of 180° scattering where $\Delta M = 0$ only. If ΔM is identically zero for all angles of scattering then the particle parameters for all orbits will be the same. Because the Coulomb excitation process is known, the exact particle parameters can be calculated. Yates (Yat 61) has made these calculations in the coordinate

system where the z-axis is the symmetry axis of the hyperbolic orbit of the projectile. For a scattering angle of 160° the correction to the coefficient of $P_2(\cos\theta)$ is - 0.64% and to that of $P_4(\cos\theta)$ is 2.14% for a ξ of 0.4. This implies that $\Delta M = 0$ holds to a very good approximation near 180°. Elbek et al (Elb 64) also give formula attributed to Y. Yoshizawa for calculating the angular distribution of the gamma rays in the incident projectile coordinate system. In most of the present experiments the mean angle of the annular counter (that angle for which the area of the counter within is equal to the area without) in the centre-of-mass coordinate system was approximately 171°, except in the case of the experiments on Ce^{140} and Sm^{144} when the angle was 158°. Consequently the particle parameters for 180° scattering are used. The particle parameter for the $P_2(\cos\theta)$ term of the angular distribution is 2 and for the $P_4(\cos\theta)$ term is $-3/2$.

A third factor affecting the angular distribution is the finite size of the annular semiconductor counter which will tend to smear out the anisotropy of the distribution. With the assumption that $\Delta M = 0$ it can be shown that the problem of determining the geometrical co-

efficients for the annular counter involves calculating

$$J_k = \int_{\gamma_1}^{\gamma_2} P_k(\cos\beta)\sin\beta \, d\beta \qquad (4.7)$$

where γ_1 and γ_2 are the minimum and maximum angles of an "imaginary counter" in the centre-of-mass coordinate system of half the angular size of the real counter (Nos 53 and Ecc 62). This geometrical correction amounts to a reduction of the anisotropy of about 1.6% for most of the experimental runs and a reduction of 4.8% for the Ce^{140} and Sm^{144} runs.

Thus the final form of the angular distribution of the gamma rays deexciting a 2^+ state to a 0^+ ground state in coincidence with particles scattered near 180^o is

$$W(\theta) = 1 + \frac{5}{7} Q_2 \frac{J_2}{J_o} P_2(\cos\theta) - \frac{12}{7} Q_4 \frac{J_4}{J_o} P_4(\cos\theta) \qquad (4.8)$$

In the case of the odd nucleus Nd^{143} the angular distribution would be exactly the same except for the spin dependent gamma-gamma correlation coefficients $A_k^{(2)}$ (subsection 2.1. 6). The ground state of Nd^{143} is $\frac{7}{2}^-$ and the first excited state has recently been determined to be $\frac{3}{2}^-$

(Dar 65). The angular distribution is then

$$W(\theta) = 1 + \frac{2}{49} Q_2 \frac{J_2}{J_o} P_2 (\cos \theta) \qquad (4.9)$$

for particles scattered near 180^o.

Table 4.2. lists the angular distribution factors $W(\theta)$ used in the present experiments.

4.2. 6. Calculated Probabilities. The probability for Coulomb excitation was calculated as described in subsection 4.1. 3. Here there is even a stronger case for using the semiclassical theory for η is typically of the order of 50. The calculations were carried out at a mean bombarding energy E_{eff} as in subsection 4.1. 3 and a numerical integration of the excitation probability over the energy loss in the target showed that this approximation is valid to better than 0.05%. However an uncertainty in the target thickness will give a corresponding uncertainty in the calculated probability. A target thickness variation of 30% has been allowed and this results in an error of 2% in the calculated probability.

Similarly an integration of the probability over the solid angle subtended by the annular detector showed that

the use of a mean angle as defined in subsection 4.2. 5 in calculating the probabilities is valid to 0.05%. The error in assuming that the mean angle and the solid angles are the same for the inelastically scattered and elastically scattered ions is also very small.

The bombarding energies are well below the Coulomb barrier. Using the value of the radius parameter determinted from O^{16} scattering from Ti^{50}, Cr^{52} and Fe^{54}, $r_o = 1.76$ fm (see subsection 5.1. 6), the Coulomb barrier for O^{16} ions on Nd^{144} is 56.3 MeV. This estimate is probably low because the value of r_o used is almost certainly too large for nuclei in the mass 140 region.

4.2. 7. Results. The experimental and calculated probabilities for the even-even nuclei are given in Table 4.3, along with E_{eff}, the excitation energy ΔE and the $B(E2)_{sp}$ values which are included in the calculated probabilities. The experimental reduced transition probabilities $\varepsilon B(E2)$ are listed as if they had been multiplied by the fraction of decays by way of gamma ray emission ε, defined as

$$\varepsilon = \frac{1}{1 + \alpha} \qquad (4.10)$$

TABLE 4.3

Target	ΔE Excitation Energy (MeV)	E_{eff} Bombarding O^{16} Energy (MeV)	Experimental Probability %	Calculated Probability %	B_{sp} ($e^2b^2 \times 10^{-2}$)	$\epsilon B(E2)_{exp}$ (e^2b^2)
Ce^{140}	1.596	44.29	0.24 ± 0.034	1.98×10^{-2}	2.159	0.27 ± 0.037
Ce^{142}	0.640	35.88	1.35 ± 0.050	7.31×10^{-2}	2.200	0.41 ± 0.015
		39.24	2.34 ± 0.097	1.22×10^{-1}		0.42 ± 0.017
		39.24	2.41 ± 0.12	1.22×10^{-1}		0.44 ± 0.022
Nd^{142}	1.570	43.81	0.29 ± 0.048	1.38×10^{-2}	2.200	0.47 ± 0.076
		43.81	0.25 ± 0.040	1.38×10^{-2}		0.40 ± 0.064
Nd^{144}	0.695	35.27	0.87 ± 0.040	4.48×10^{-2}	2.242	0.43 ± 0.020
		38.56	1.59 ± 0.071	7.99×10^{-2}		0.45 ± 0.020
Nd^{146}	0.460	35.27	2.85 ± 0.062	1.00×10^{-1}	2.283	0.65 ± 0.014
		38.56	4.44 ± 0.107	1.57×10^{-1}		0.65 ± 0.016
		39.24	4.72 ± 0.139	1.70×10^{-1}		0.63 ± 0.019
Nd^{148}	0.300	35.27	6.26 ± 0.160	1.62×10^{-1}	2.325	0.90 ± 0.023
		38.56	9.42 ± 0.264	2.31×10^{-1}		0.95 ± 0.027
Sm^{144}	1.60	44.29	0.13 ± 0.020	1.18×10^{-2}	2.242	0.25 ± 0.038
Sm^{148}	0.551	35.85	2.09 ± 0.066	6.88×10^{-2}	2.325	0.71 ± 0.022
		39.21	3.39 ± 0.133	1.13×10^{-2}		0.70 ± 0.027
Sm^{150}	0.334	31.09	3.58 ± 0.136	7.32×10^{-2}	2.367	1.16 ± 0.044
		39.21	9.65 ± 0.378	2.03×10^{-1}		1.12 ± 0.044

where α is the internal conversion coefficient for the decay, because only gamma rays are detected. The errors are statistical only.

A 740 keV gamma ray was observed from the Nd^{143} target. This energy agrees with the energy obtained for the first excited state in recent (d,p) stripping reaction studies which also show that this state has spin and parity $\frac{3^-}{2}$ (Dar 65). Table 4.4 gives the experimental probability for exciting the 740 keV state and the calculated probabilities using the Weisskopf single-particle value B_W for the reduced transition strength (subsection 2.1. 4) which is one-fifth $B(E2)_{sp}$ used for the even nuclei. Also given in the table is the experimental upward reduced transition strength $B(E2; \frac{7}{2} \rightarrow \frac{3}{2})$ and its enhancement over B_W.

4.3. "Reorientation Effect" Cd^{114}, Sm^{148}, Sm^{150}.

4.3. 1. Experimental Probabilities. The problems relating to and the techniques used in the analysis of the back-scattered ion-gamma ray coincidence results are discussed in the preceding section. However, because the experimental quantity determined is the ratio of the probability for excitation by S^{32} ions to that for O^{16} ions, P_s/P_O, and because the experimental geometry is kept fixed many of the

T A B L E 4.4

Target	ΔE Excitation Energy (MeV)	E_{eff} Bombarding O^{16} Energy (MeV)	Experimental Probability %	Calculated Probability (includes B_w) %	B_w e^2b^2	$B(E2;\frac{7}{2} \rightarrow \frac{3}{2})$ e^2b^2	$B(E2;\frac{7}{2} \rightarrow \frac{3}{2})$
$Nd^{143}(\frac{7}{2}-)$	$0.740(\frac{3}{2}-)$	43.59	0.306 ± 0.082	2.89×10^{-2}	4.46×10^{-3}	$(4.72 \pm 1.27) \times 10^{-2}$	11

corrections described before cancel out and many of the others are considerably less important. In particular corrections for the efficiency of the gamma ray counter (one of the major uncertainties), for absorption of gamma rays and for internal conversion cancel out and errors due to lost coincidences are nearly zero because the gamma ray rate in the NaI(Tl) crystal is kept constant by using an artificial source of gamma rays (subsection 3.3. 4).

The number of random coincidences in the photopeak is somewhat higher than for the experimental conditions described in the previous section because the bombarding energy has been kept low to minimize the effects of multiple Coulomb excitation. In the first two sets of runs the number of random coincidences in the photopeak was about 6% of the total photopeak in the case of Cd^{114}, 2% in the case of Sm^{150} and 15% in the case of Sm^{148}. In the third run the number of randoms was 5% for Sm^{150} and 10% for Sm^{148}.

The angular distribution corrections $W(\theta)$ are slightly different for S^{32} and O^{16} ion excitation because of the slight difference in solid angle subtended by the semi-conductor counter in the centre-of-mass coordinate system. The correction to the experimental probability ratio for

this effect never exceeds 1%.

4.3.2. Cadmium Target. The Cd^{114} target contains 1.73% Cd^{113}, 0.69% Cd^{112}, 0.14% Cd^{111} and 0.25% Cd^{116} and many of these isotopes have gamma ray transitions very close in energy to that of the 2^+ to 0^+ transition in Cd^{114}. It can be shown by using Equations 4.1 and 4.5 that the effect of the impurity isotopes (at least the even mass ones) on the probability ratio cancels out to second order provided the parameter ξ is the same for both S^{32} and O^{16} excitation. Although this is only approximately true in the present experiments (see Table 4.5) the correction is still negligible because of the small percentage of the impurity isotopes. For example, in the case of 51.9 MeV S^{32} ions and 27.5 MeV O^{16} ions the correction to the probability ratio due to the presence of the Cd^{112} isotope is only $(2.6 \times 10^{-2})\%$. The above considerations strictly apply to cases of direct excitation but it is expected that the correction for multiple excitation to the 582 keV $5/2^+$ state via the $3/2^+$ state in Cd^{113} is similarly negligible at the present bombarding energies.

4.3.3. Experimental Results. Table 4.5 lists the experimentally determined ratio $\frac{R_s}{R_o}$ of the number of gamma rays detected in the photopeak at 45° to the incident beam

LEGEND FOR TABLE 4.5

Col. 4.	$E_{eff.}$	The heavy ion bombarding energy, corrected for energy loss in the target
Col. 5.	t	The target thickness
Col. 6.	E	The excited state energy
Col. 8.	$\frac{n_s}{n_0}$	The experimental probability ratio
Col. 9.	$\frac{P_s}{P_0}$	The theoretical probability ratio calculated in first-order perturbation theory
Col. 10.	$\Delta^{(1)}$	The interference correction term to the first-order probability for a quadrupole moment of 1 b.
Col. 11.	Q	The experimental quadrupole moments of the 2^+ states.
Col. 12.	$\overline{Q}$	The average quadrupole moments. The errors quoted are either determined from the individual errors or from the deviation of the individual measurements from the mean, which ever is larger
Col. 13.	$\overline{B(E2)}$	The average experimental B(E2) value

TABLE 4.5

Nucleus	Run	Beam	E_{eff} (MeV)	Δt (μgm cm^2)	E (MeV)	ξ	$\frac{R_s}{R_o}$	$\frac{P_s}{P_o}$	$\Delta(1)$ (b^{-1})	Q (b)	$\overline{Q}$ (b)	$\overline{B(E2)}$ (e^2b^2)
Cd^{114}	1	S^{7+}	51.06	66	0.558	0.680	1.123±0.043	1.194±0.007	0.253	-0.48±0.33	-0.51±0.23	0.48
		O^{5+}	27.27			0.551			0.150			
	2	S^{7+}	51.06			0.680	1.130±0.042	1.194±0.007	0.253	-0.53±0.33		
		O^{5+}	27.27			0.551			0.150			
Sm^{148}	2	S^{7+}	50.92	102	0.551	0.840	1.156±0.050	1.187±0.012	0.190	-0.32±0.51		
		O^{5+}	27.23			0.697			0.111			
	3	S^{7+}	53.32	73*		0.782	1.665±0.035	1.856±0.008	0.196	-1.07±0.20	-0.79±0.34	0.79
		O^{5+}	27.06			0.704			0.111			
		S^{7+}	52.96				1.868±0.065	1.841±0.008	0.195	+0.18±0.43		
		O^{5+}	26.89						0.111			
Sm^{150}	1	S^{7+}	51.28	37	0.334	0.492	1.490±0.036	1.653±0.004	0.136	-1.60±0.35		
		O^{5+}	27.35			0.410			0.0776			
	2	S^{7+}	51.28			0.492	1.477±0.036	1.653±0.004	0.136	-1.50±0.33	-1.41±0.23	1.44
		O^{5+}	27.35			0.410			0.0776			
	3	S^{6+}	41.82	80		0.670	3.334±0.080	3.562±0.017	0.125	-1.05±0.38		
		O^{4+}	19.57			0.682			0.0680			

* a different target.

direction per backscattered ion, where

$$R = \frac{N(\gamma)}{N(I)} , \qquad (4.11)$$

for S^{32} (R_s) and O^{16} (R_o) Coulomb excitation. This ratio includes the angular distribution correction mentioned in subsection 4.3. 1.

4.3. 4. Calculated Probabilities. The theoretical Coulomb excitation probabilities P have been calculated in the first instance using first-order perturbation theory because the experimental excitation probability is very small (less than 3% even in the case of Sm^{150}). The calculations were carried out for a mean scattering angle which makes the area of the semiconductor detector within that angle equal to the area without and for an effective bombarding energy E_{eff} which is the beam energy less one-half the energy loss in the target. Numerical integration over the solid angle of the annular detector and over the energy range in the target showed these approximations were accurate to better than 0.05%.

As described in the previous sections the symmetrized form of the differential excitation cross-section in the semi-classical approximation has been used. The symmetrized semi-classical approximation is certainly accurate enough for the present calculations because the Sommerfeld number

is greater than 50 in all cases when using O^{16} ions and greater than 90 in all cases when using S^{32} ions. Corrections for different inelastic and elastic scattering angles and solid angles (centre-of-mass system) have been estimated not to exceed 0.1% and have consequently been neglected.

The main source of error in calculating the excitation probabilities P arises from uncertainty in E_{eff} due principally to uncertainties about the target thickness. Here again, however, comparing the excitation probability for two different ions greatly reduces this factor.

It can be shown that the fractional change in the ratio P_s/P_o for a small change in target thickness Δt is

$$\frac{\Delta \frac{P_s}{P_o}}{\frac{P_s}{P_o}} = \pm \Delta t \cdot \left\{ \frac{1}{E_o} \left(\frac{m+2}{2}\right) \left(\frac{dE}{dx}\right)_o - \frac{1}{E_s} \left(\frac{n+2}{2}\right) \left(\frac{dE}{dx}\right)_s \right\} \qquad (4.12)$$

where E is the bombarding energy of the ion (s for sulphur, O for oxygen) and $\frac{dE}{dx}$ is the stopping power in the target for the ion of energy E. The principal assumption of the derivation is that the Coulomb excitation differential cross-section can be expressed as

$$d\sigma_{E2} \quad \alpha \quad E^i, \qquad (4.13)$$

$$\text{where } i = \begin{cases} m \text{ for } O^{16} \text{ ions} \\ n \text{ for } S^{32} \text{ ions,} \end{cases}$$

in a range of energies about E.

As an example, the case of 27.5 MeV O^{16} ions and 52 MeV S^{32} ions on Cd^{114}, where m = 4.4 and n = 5.3, a 20% uncertainty in the target thickness of 94 $\mu g/cm^2$ at 45° to the beam direction results in a 0.5% uncertainty in $\frac{P_s}{P_o}$.

The errors on $\frac{P_s}{P_o}$ are listed in Table 4.5 for a 20% uncertainty in target thickness. This uncertainty has been estimated from the reproducibility with which the target thicknesses have been determined.

4.3. 5. Quadrupole Moments; Perturbation Theory. Using second order perturbation theory the quadrupole moment of the 2^+ state Q can be calculated from

$$\frac{R_s}{R_o} = \frac{P_s}{P_o} \frac{(1 + \Delta_s^{(1)} Q)}{(1 + \Delta_o^{(1)} Q)} \qquad (4.14)$$

where $\Delta^{(1)} Q$ is the correction to the first order theory from interference between first and second order processes (subsection 2.1. 9). The quantities $\Delta^{(1)}$ calculated for a mean scattering angle at an energy E_{eff} are listed in Table 4.5 (Dou 65). The values of Q obtained from this

analysis are also presented in the table along with the B(E2) values obtained (by applying the corrections discussed in Section 4.2). The error on the B(E2) values is about 10%.

4.3. 6. Quadrupole Moments; Schrodinger Equation Solution.

As discussed in subsection 2.1. 9 the usefulness of the perturbation approach depends on the insignificance of terms of the order of $d\sigma^{(2)}$. Recently numerical techniques of solving the Schrodinger equation for Coulomb excitation have become available (subsection 2.1. 11) and this provides an opportunity to test the accuracy of the perturbation approach.

Because the probability of excitation is extremely low in the present experiments only a few levels need to be included in the numerical solution of the Schrodinger equation, and the effect of varying the number of levels can easily be tested. As well as requiring the energies of the levels the transition matrix elements between levels and the static matrix elements of the levels must be known. Only electric quadrupole excitation is considered. Fortunately the important levels are the ones for which the transition matrix elements are most easily measured. These matrix elements can also be varied to test the sensitivity of the solutions to both their magnitude and sign. In general, only the

static quadrupole moment of the first excited 2^+ state is kept different from zero in a calculation to determine the excitation probability of the first excited state. The contribution of the static moments of the higher states in this case is likely to be an order of magnitude down on the contribution from the transition strengths between the states and, as will become evident, can thus be neglected. Of course the transition strength from the ground state to the first excited state is the most important parameter but by comparing the excitation probability for two different ions the effect of this transition strength on the determination of the quadrupole moment of the first excited state is rendered fairly unimportant.

Figure 4.5 displays a comparison of the probability ratio $\frac{P_s}{P_o}$ for 51.28 MeV S^{32} ions and 27.35 MeV O^{16} ions as a function of the quadrupole moment Q of the 2^+ state calculated by perturbation theory and by solving the Schrodinger equation. The dashed curve is the perturbation calculation which includes only the interference term $d\sigma^{(1,2)}$. The solid curve gives a three level Schrodinger equation calculation for 180° scattering which includes the ground state, first excited 2^+ state and first excited 4^+ state (Smi 65). The level scheme and upward B(E2) values of Sm^{150} are given

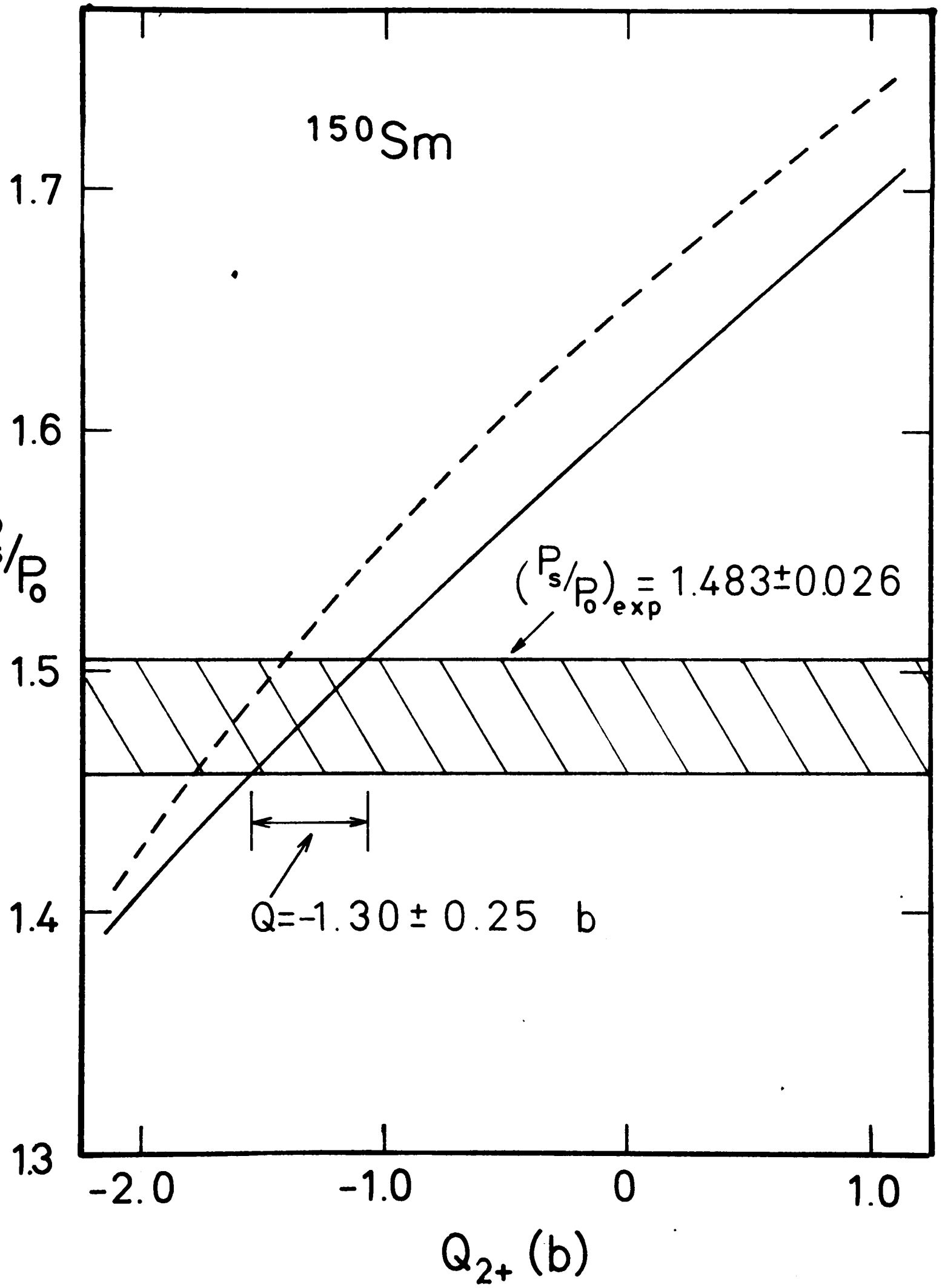

^{150}Sm
1.7
1.6
1.5
1.4
1.3
P_s/P_o
$(P_s/P_o)_{exp} = 1.483 \pm 0.026$
Q=-1.30 ± 0.25 b
-2.0
-1.0
0
1.0
Q_{2+} (b)

Fig. 4.5

in Figure 4.6. (Ken 64; Yos 64). The effect on $\frac{P_s}{P_o}$ of including the 0^{1+} state and 2^{1+} state in a five level calculation was determined to be less than 0.5% at a Q of -1b. A change in the B(E2; $0^+ \rightarrow 2^+$) value of 4.5% changes $\frac{P_s}{P_o}$ by less than 0.34%.

Figure 4.5 reveals two interesting features. One is the similarity in shape of the two curves which suggests that high order effects tend to cancel the contribution from $d\sigma^{(2)}$. If $d\sigma^{(2)}$ (which depends on Q^2) is added to the perturbation calculation a parabolic shape results (the sign of $d\sigma^{(2)}$ is positive). The other feature is the discrepancy of about 2.9% between the two calculations at Q = 0, a discrepancy which persists if only a two level calculation is carried out. There are some obvious sources of this discrepancy. One is that the Schrodinger equation calculation is calculated for 180° scattering and not for the exact laboratory scattering angle of 166°. A three level calculation at Q = -1b for the correct angle raised $\frac{P_s}{P_o}$ by 0.67%. On the other hand perturbation theory neglects higher order contributions arising from more than one transition between ground and first excited state, and also the perturbation theory amplitudes are not properly normalized (the ground state is always assumed to be completely populated). The

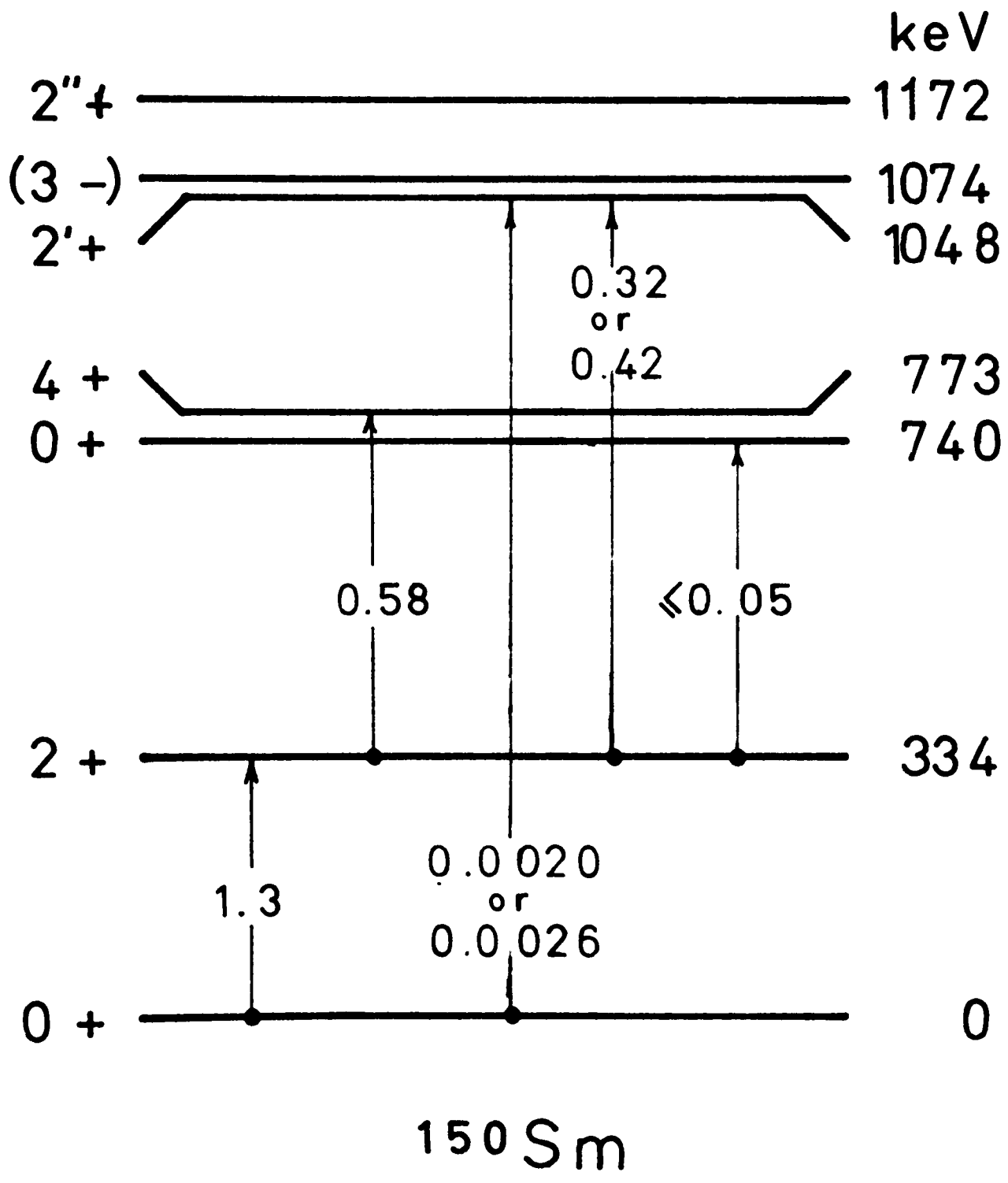

keV
2"+
1172
(3 −)
1074
2'+
1048
0.32
or
0.42
4 +
773
0 +
740
0.58
⩽0.05
2 +
334
0.0020
or
0.0026
1.3
0 +
0
150Sm

Fig. 4.6

properly normalized probability of exciting the 2^+ state is

$$P_{norm}(2^+) = \frac{P(2^+)}{1 + P(2^+)} \qquad (4.15)$$

where $P(2^+)$ is the ordinarily calculated probability. This correction results in a lowering of the perturbation calculation of $\frac{P_s}{P_o}$ by up to 1%. Another factor which is not so easy to assess is the effect of the energy loss of the projectile on the results of the Schrodinger equation calculations. Some idea of the correction can probably be obtained, however, by calculating the change in the perturbation cross-section $d\sigma_{E2}$ (Equation 2.20) with the use of a symmetrized a^{-2} factor. This estimation suggests that the Schrodinger equation calculation of $\frac{P_s}{P_o}$ may be low by 0.6% for Sm^{150} and by as much as 1% for the other nuclei. When all these corrections have been taken into account (including an estimate of third-order excitation using perturbation theory) there appears to remain approximately a 1% discrepancy between the two methods of calculation. There is, of course, the possibility of numerical uncertainties which may account for this discrepancy; in particular integration errors may arise in the Schrodinger equation calculation. However,

until this discrepancy is cleared up both sets of results will be presented.

When solving the Schrodinger equation the signs of the transition matrix elements may in some cases be important (just as the sign of the quadrupole moment is important). General considerations show, however, that provided E4 excitation can be neglected only a $2'^{+}$ state can contribute transition matrix elements whose signs may affect the excitation probability of the first 2^{+} state.

Table 4.6 presents the final results obtained by solving the Schrodinger equation for the number of levels listed.

TABLE 4.6

Quadrupole Moments of the first 2^{+} levels obtained by solving the Schrodinger Equation.

Nucleus	ΔE (MeV)	Number of Levels	Q(b) Present Work	Other	Ref
Cd^{114}	0.558	2	-0.26 ± 0.24		
				-0.7 ± 0.2	(deB 65)
				-0.6 ± 0.2	(Ste 65)
Sm^{148}	0.551	4	-0.76 ± 0.42		
Sm^{150}	0.334	3	-1.10 ± 0.23		

The energy spectra used are shown in Figures 4.6, 4.7 and 4.8. Also included in the Table are the results obtained by de Boer et al (deB 65) and Stelson et al (Ste 65) for Cd^{114} who both used a 7- level Schrodinger equation calculation in analyzing these results. In the case of Sm^{148} the levels which have been used are the 0^+, 2^+, 4^+ and $2'^+$ levels. All the calculations were done for 180^o scattering. The values of Q obtained should be compared with the perturbation results presented in the second last column of Table 4.5.

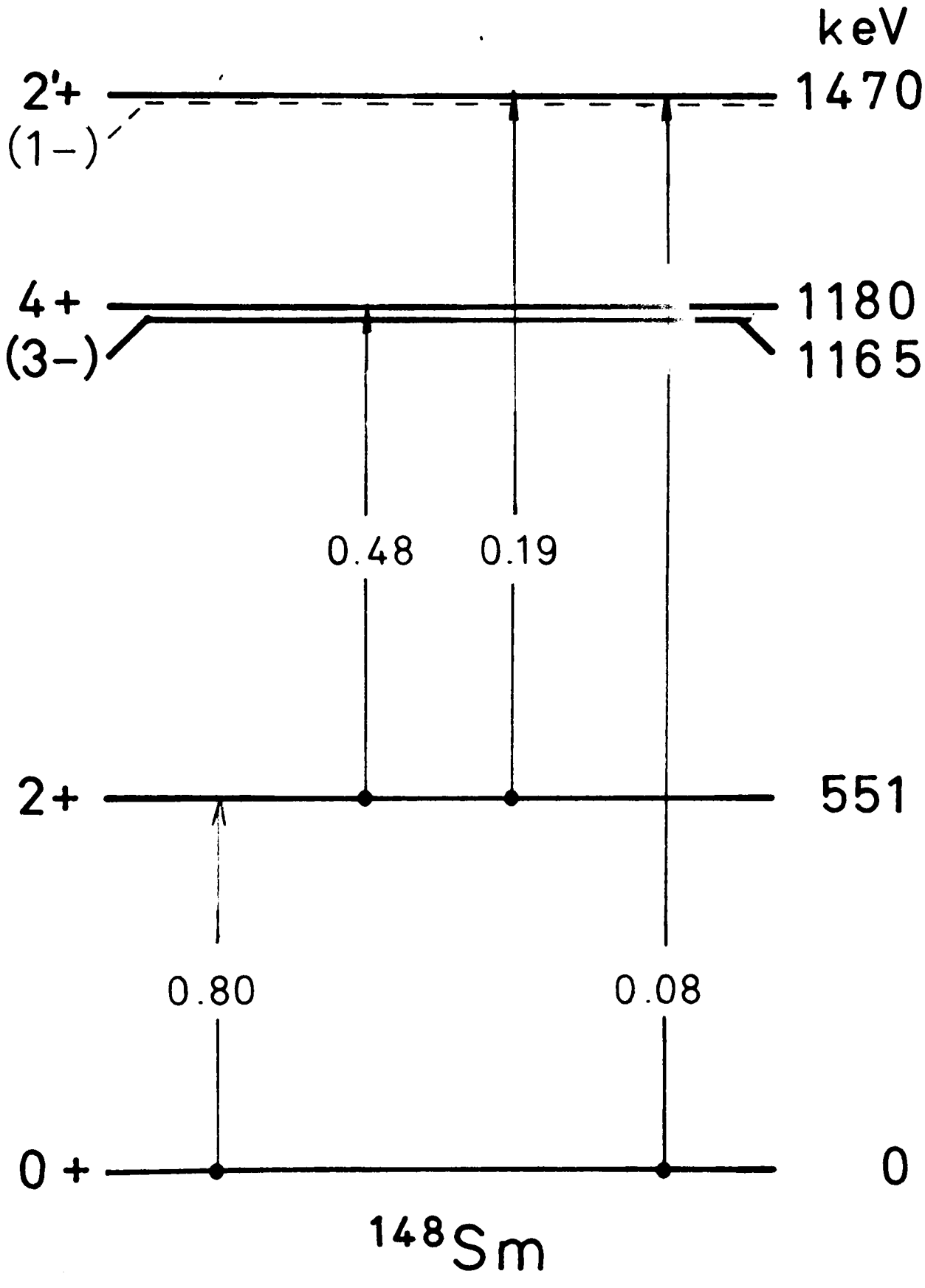


Fig. 4.7

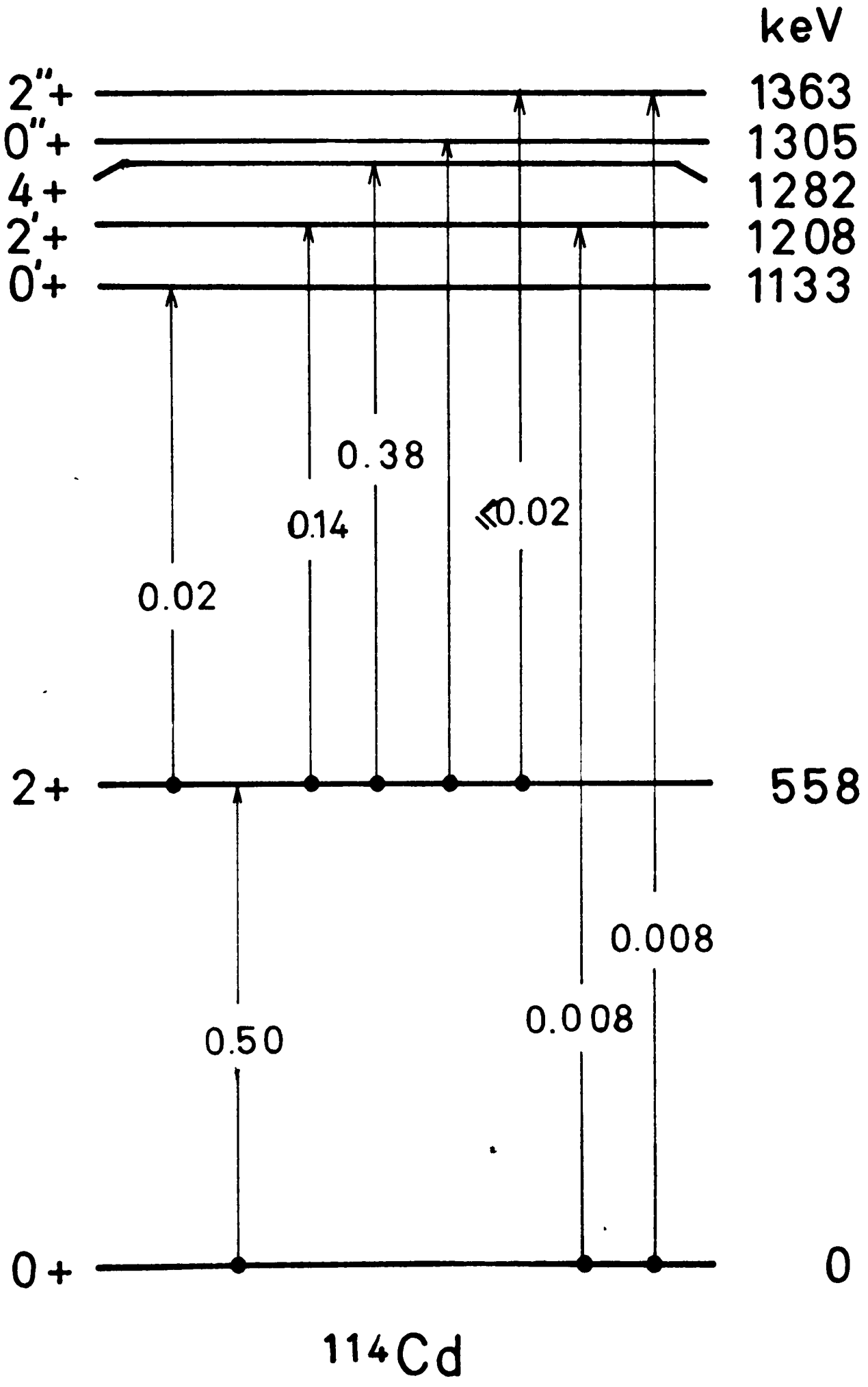

keV
2''+
0''+
4+
2'+
0'+
1363
1305
1282
1208
1133
0.38
0.14
<0.02
0.02
2+
558
0.008
0.008
0.50
0+
0
114Cd

Fig. 4.8

C H A P T E R 5

DISCUSSION OF RESULTS

In this chapter the electric quadrupole transition strengths and the excited state quadrupole moments determined in the present work are discussed. In the first section the transition strengths are compared principally with calculations of the pairing plus quadrupole force theory although for the N = 28 nuclei a comparison with the pure configuration approach to the shell model is also made. The systematics of the transition strengths in the nuclei in the mass - 140 region are also examined and they display some striking characteristics. A very brief discussion of the correct parameter r_o to be used in the traditional Coulomb barrier formula (Section 2.1) and of the effect on inelastic scattering of being above the Coulomb barrier is presented.

The quadrupole moments of Cd^{114}, Sm^{148} and Sm^{150} are discussed in the second section. In order to get a feeling for their magnitude they are compared to calculations based on both the permanently deformed model and the phonon model. In their simplest form both of these models are shown to

be unsatisfactory and the effect of some modifications to these models ~~to result~~ is somewhat better agreement with the quadrupole moments. However, these modified models are not quite so successful in explaining some of the other low energy properties of these nuclei. The predictions of the pairing plus quadrupole force theory in the random phase approximation are also briefly mentioned.

5.1. Electric Quadrupole Transition Strengths.

5.1. 1. Final B(E2) Values. The final B(E2) values for the ground to first excited state transition in the nuclei studied in this work are presented in Tables 5.1, 5.2 and 4.4.

Table 5.1 presents the results for Ti^{50}, Cr^{52} and Fe^{54} along with the results of other experiments. In the present result for Fe^{54} the experimental value obtained at 40.7 MeV O^{16} bombarding energy (Table 4.1) has not been included because the bombarding energy was above the Coulomb barrier.

The final B(E2) values for the even nuclei $Ce^{140,142}$, $Nd^{142-148}$ and $Sm^{144,148,150}$ are presented in Table 5.2 along with other experimental results for Nd^{150}, Sm^{152} and Sm^{154}. The present results include a correction for internal conversion using the coefficients α listed in the table (Gol 61).

TABLE 5.1

The final averaged transition probabilities together with those obtained in other experiments.

Nucleus	$\frac{B(E2)_{exp}}{B(E2)_{sp}}$	$B(E2;\ 0^+ \rightarrow 2^+)\ e^2b^2$		
		Present Experiment	Other Experiments	Ref.
Ti^{50}	4.4 ± 0.4	0.024 ± 0.002	0.04	(Vas 62)
Cr^{52}	8.4 ± 0.3	0.048 ± 0.002	0.0515 ± 0.0042*	(Bel 65)
			0.062	(Lem 60)
			0.06 ± 0.015	(Ada 60)
			0.08 ± 0.02	(Ofe 59)
Fe^{54}	8.3 ± 0.4	0.051 ± 0.002	0.0535 ± 0.0026	(Bel 62)

x This result was published subsequent to the present result.

TABLE 5.2

Nucleus	Excitation Energy ΔE (MeV)	α	Present Experiment	$B(E2)_{exp}(e^2b^2)$ Other Experiments						$\frac{B(E2)_{exp}}{B(E2)_{sp}}$
				Nat 60	Elb 60	Sun 55; Bir 59	Sha 58	Yos 64	Other References	
Ce^{140}	1.596		0.27±0.04	0.31(±200%)					0.36±0.04 (Ofe 59a)	12.5
Ce^{142}	0.640		0.42±0.01	0.59(±200%)						19.1
Nd^{142}	1.570		0.42±0.05	0.34(±200%)						19.1
Nd^{144}	0.695		0.44±0.02	0.44(±200%)						19.6
Nd^{146}	0.460		0.65±0.01							28.5
Nd^{148}	0.300	0.04	0.96±0.02							41.3
Nd^{150}	0.131	0.84				2.6±0.1			2.67±0.10 (Bje 63)	112.8
Sm^{144}	1.60		0.25±0.04							11.2
Sm^{148}	0.560		0.79±0.02		0.89±0.10			0.72*		30.1
Sm^{150}	0.334	0.04	1.34±0.06		1.32±0.06			1.41*		50.3
Sm^{152}	0.122	1.18			3.40±0.15	3.4±0.1	3.20±0.36		4.1±0.10 (She 60)	141
Sm^{154}	0.082	4.93			4.61±0.20	4.7±0.4	3.45±0.4		4.1±0.4 (Gol 61)	188

* These results were published subsequent to the present results.

The errors in the present results should be understood as relative errors for comparing the results among themselves. To obtain an absolute error an error of 10% to account for the uncertainties in the gamma ray efficiency correction should be added in quadrature.

The B(E2) values of Sm^{148} and Sm^{150} have been corrected for the "reorientation" effect. Table 5.3 lists the corrections $\Delta^{(1)}$ Q obtained from perturbation theory to be applied as

$$B(E2)_{correct} = \frac{B(E2)_{exp}}{(1 + \Delta^{(1)} Q)} \qquad (5.1)$$

as well as the corrected B(E2) values, employing a quadrupole moment which is the average of the perturbation theory and Schrodinger equation results of Section 4.3. The results of Yoshizawa et al (Yos 64) giving B(E2) values of 0.64 e^2b^2 and 1.24 e^2b^2 for Sm^{148} and Sm^{150} respectively have also been corrected for the reorientation effect because they have used heavy ion Coulomb excitation in their experiments. The results of Elbeck et al (Elb 60) do not require "reorientation" effect corrections because they make measurements of inelastic scattering of protons and deuterons for which the effect is negligible.

TABLE 5.3

B(E2) Values of Sm^{148} and Sm^{150} corrected for the reorientation effect.

Nucleus	Q b	E_{eff} MeV	$\Delta^{(1)}$ b^{-1}	B(E2)correct e^2b^2	Ref.
Sm^{148}	-0.78	35.85	0.126	0.788	
		39.21	0.132	0.781	
		43.5	0.136	0.72	(Yos 64)
Sm^{150}	-1.3	31.09	0.082	1.35	
		39.21	0.088	1.32	
		43.5	0.09	1.41	(Yos 64)

The agreement of the presently determined B(E2) values for $Ce^{140,142}$ and $Nd^{142,144}$ with those of Nathan and Popov (Nat 60) may be fortuitous because the absolute error on their results may be as large as a factor of two. The only substantial disagreements in B(E2) values are amongst the values for $Sm^{152,154}$ obtained by Elbeck et al (Elb 60), Sharp and Buechner (Sha 58) and Sheline et al (She 60) who all used similar experimental methods. However, the B(E2)

values obtained from lifetime measurements (Bir 59; Sun 55) are in good agreement with the results of Elbek et al (Elb 60) and of Bjerregard et al (Bje 63) for Nd^{150} and these latter values will be used in discussing the systematics of the B(E2) values.

Table 4.4 presents the B(E2) value for the upward transition in Nd^{143}. This value will be discussed briefly in subection 5.1. 3.

5.1. 2. Pairing Force Calculations. Early calculations by Kisslinger and Sorensen (Kis 60) and MacDonald (Mac 63) failed to account for the trend of B(E2) values in the even Ni isotopes (Z = 28). Experimentally the lighter isotopes showed transition strengths much more enhanced than was expected on the basis of the pairing plus quadrupole force calculations. MacDonald suggested that possibly the neutrons in the closed shell at N = 28 which were neglected in the calculations contributed to enhancing the B(E2) values preferentially in the lighter Ni isotopes. This consideration prompted the study of the B(E2) values of the N = 28 nuclei Ti^{50}, Cr^{52} and Fe^{54} where unlike the Ni case, the last filled core shell ($s_{\frac{1}{2}}$, $d_{3/2}$ protons) has opposite parity to the levels which the valence protons are presumed to be filling (primarily $f_{7/2}$). It was hoped in consequence that

the calculations of the B(E2) values would be insignificantly affected by the core states and that they would be a good test of the pairing plus quadrupole force calculations.

Table 5.4 and Figure 5.1 compare the B(E2; $0^+ \longrightarrow 2^+$) enhancements over the single-particle values obtained in the present work with two calculations by MacDonald (Mac 63) in the random phase approximation (RPA). An effective

TABLE 5.4

Comparison of Experimental and Theoretical B(E2) Enhancements.

Nucleus	Experiment $\frac{B(E2;\ 0^+ \longrightarrow 2^+)}{B_{sp}\ (E2)}$	RPA		Pure Configuration.
		Constant X	Emperical $\hbar\omega$ of Ti^{50}	
Ti^{50}	4.4	3.5	5.3	6.3
Cr^{52}	8.4	8.4	8.4	8.4
Fe^{54}	8.3	10.2	10.2	6.3

charge of 1.27e for protons has been chosen to make the theoretical calculation for Cr^{52} agree with the experimental

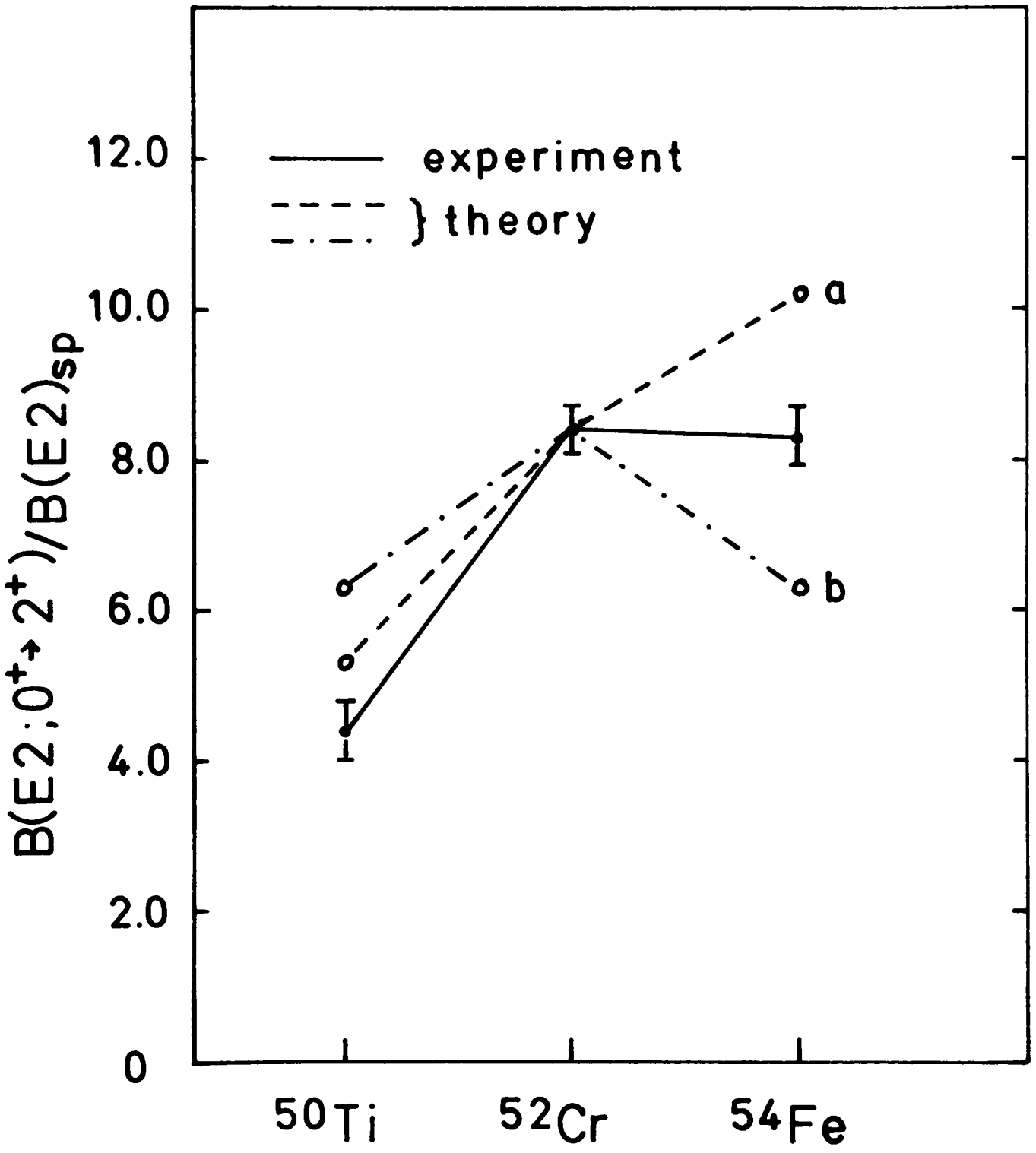

12.0
10.0
8.0
6.0
4.0
2.0
0
experiment
} theory
a
b
B(E2;0+→2+)/B(E2)sp
50Ti
52Cr
54Fe

Fig. 5.1

value. The four single-particle levels $d_{3/2}$, $f_{7/2}$, $p_{3/2}$ and $f_{5/2}$ with energies as given by Kisslinger and Sorensen (Kis 60) are used. The theoretical calculation labelled "constant X" is a calculation which uses a quadrupole force strength giving reasonably accurate energies for the 2^+ state in Cr^{52} and Fe^{54} but puts the 2^+ level in Ti^{50} at 1.85 MeV. The other calculation has the quadrupole force strength adjusted in the Ti^{50} calculation to give a 2^+ energy of 1.56 MeV. In the figure the points labelled "a" are from this latter calculation.

Also presented in Table 5.4 and Figure 5.1 for comparison are the results of a pure $(f_{7/2})^n$ configuration calculation which has had considerable success in predicting many of the energy levels, dipole moments and spectroscopic factors of nuclei in the 1 $f_{7/2}$ shell (Law 57; Tal 58, 60, 62; deS 63; McC 64). In this calculation some energies and matrix elements determined from the experimental data of one of the nuclei in the region are used as parameters to calculate the low energy properties of the other nuclei assuming that the valence nucleons in the $f_{7/2}$ states are responsible for these properties. In this model the relation between B(E2) values is (Equation 28.25, deS 63).

$$\frac{B(E2;0^+ \rightarrow 2^+)_n}{B_{sp}(E2)_n} = \frac{n(2j-n+1)}{2(2j-1)} \qquad \frac{B(E2;\ 0^+ \rightarrow 2^+)_n}{B_{sp}\ (E2)_{n=2}} = 2 \qquad (5.2)$$

where $B_{sp}(E2)_n$ is the single-particle B(E2) value for the nucleus with n (even) valence nucleons in the j-shell. (Comparing the enhancements of the B(E2) values goes some way to removing the dependence of the B(E2) values on the radial wavefunctions of the valence nucleons). The values in the table and the points labelled "b" in the figure are these calculations normalized to the Cr^{52} value.

The mass - 140 region is an interesting region because isotopes of Nd and Sm extend from a single-closed shell at N = 28 to the fully-deformed nuclei Sm^{152} and Sm^{154} and possibly Nd^{150}. Table 5.5 and Figure 5.2 present a comparison of the experimental transition strengths for $Ce^{140,142}$, $Nd^{142-146}$ and $Sm^{144-150}$ with the theroetical calculations of Kisslinger and Sorensen (Kis 63). In these calculations

TABLE 5.5.

Nucleus	$B(E2, 0^+ \rightarrow 2^+)$ values (e^2b^2)		
	Experimental	Theoretical	
		R P A	Q P I
Ce^{140}	0.27	0.392	0.284
Ce^{142}	0.42	0.828	
Nd^{142}	0.42	0.361	0.358
Nd^{144}	0.44	0.908	
Nd^{146}	0.65	2.101	
Sm^{144}	0.25		0.458
Sm^{148}	0.79	2.189	
Sm^{150}	1.34	4.0 *	

* A different force constant. See text.

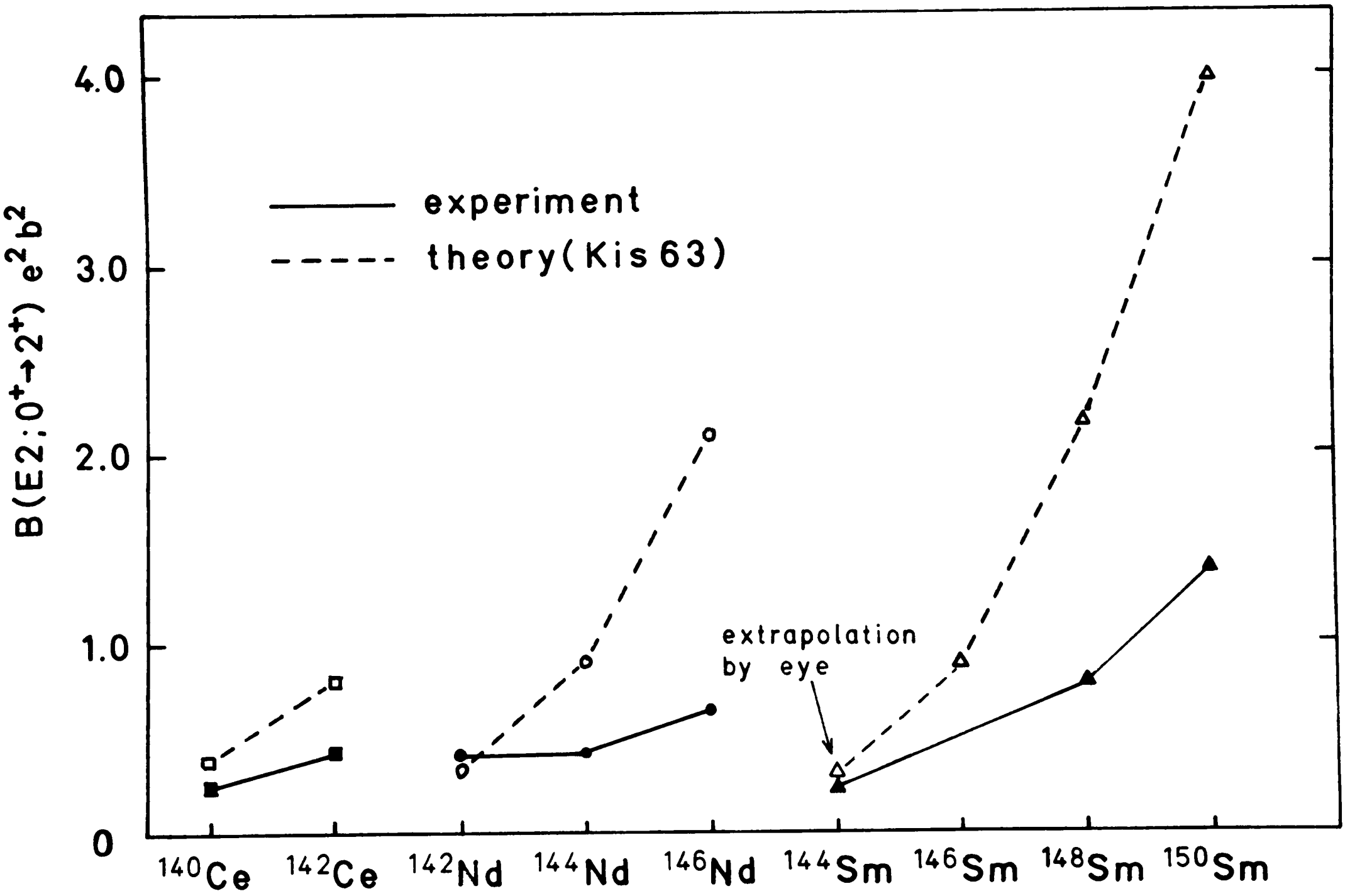

B(E2;0⁺→2⁺) e²b²
4.0
3.0
2.0
1.0
0
experiment
theory(Kis 63)
extrapolation
by eye
140Ce
142Ce
142Nd
144Nd
146Nd
144Sm
146Sm
148Sm
150Sm

Fig. 5.2

an effective charge of 2e for protons and e for neutrons is used. The same force constants are used throughout (with the appropriate A-dependence) except in Sm^{150} where the quadrupole force strength has been varied because the model otherwise predicts the first excited state of Sm^{150} much too low in energy.

Also included in the table are the results of Rho (Rho 65) labelled QPI, who uses a more general type of residual force than the pairing force and diagonalizes the interaction between states of pairs of quasi-particles (Section 2.2). An effective charge of 2e for protons is used and the calculations presented here also include an estimate (using perturbation theory) of ground state correlation effects.

It can be seen from the tables and figures that the B(E2) values for the single-closed shell nuclei are quite well explained by the pairing plus quadrupole force theory although in the N = 28 isotones the results of the pure configuration calculation perhaps suggest that too many configurations have been mixed in by the pairing force, over-enhancing the B(E2) value of Fe^{54}. On the other hand for nuclei removed from the single-closed shell by four or even two particles this model grossly overestimates the B(E2) values.

5.1. 3. B(E2) Value of Nd^{143}. The upward transition strength of Nd^{143} presented in Table 4.4 implies a downward B(E2; $\frac{3}{2}^- \rightarrow \frac{7}{2}^-$) value of $(9.4 \pm 2.6) \times 10^{-2}$ e^2b^2. Unfortunately the B(E2) value of Nd^{143} has not been calculated in the pairing plus quadrupole force model (see (Sor 64) for B(E2) values of other spherical odd-mass nuclei) nor have excited state wavefunctions been calculated by Kisslinger and Sorenson. However, in a nuclear model in which the ground state and the low energy states of an odd nucleus are interpreted as a shell-model particle ($j = \frac{7}{2}$ for Nd^{143}) weakly coupled to the ground state and first excited 2^+ state of the even core the downward B(E2) value for the odd nucleus should equal the downward B(E2) value of the core (Nat 65; Elb 64). Experimentally the B(E2; $2^+ \rightarrow 0^+$) value of Nd^{142} is $(8.4 \pm 1.0) \times 10^{-2}$ e^2b^2 which agrees very well with the value in Nd^{143} and means that, on the basis of the B(E2) values, this weak-coupling picture is not ruled out.

5.1. 4. Systematics of B(E2) Values. As discussed in Section 5.1. 2 the Nd-Sm region is a transitional region in which the lighter isotopes are single-closed shell nuclei, presumably spherical and the heavier isotopes for example Sm^{154}, are premanently deformed displaying well-developed

rotational structure. It might be hoped then that the B(E2) values would reflect the change in structure. A first glance at the enhancements of the transition strengths over the single-particle estimate $\frac{B(E2)_{exp}}{B(E2)_{sp}}$, listed in Table 5.2, seems to confirm this conjecture. However, the A-dependence of the $\frac{B(E2)_{exp}}{B(E2)_{sp}}$ ratios is misleading because it reflects the A-dependence of the energy of the 2^+ state. In fact both the rotational model of a spheroidal nucleus and the irrotational flow model for small oscillations about a spherical shape predict that

$$B(E2) \quad \alpha \quad \frac{Z^2}{E_{2+} \cdot A^{1/3}} \qquad (5.3)$$

although the constant of proportionality differs by over a factor of two in the two cases (Gro 62).

Figure 5.3 displays the product $E_{2+} \cdot B(E2)$ as a function of neutron number N. The dependence on Z^2 is qualitatively correct but nothing can be said about the A-dependence. There is no evidence of a discontinuity (except possibly at the closed shell for Ce^{140} and Nd^{142}) implied by the different constants of proportionality in Equation 5.3. for the rotational or vibrational model whereas the two-neutron binding energy shows a marked change for $N > 88$ and this

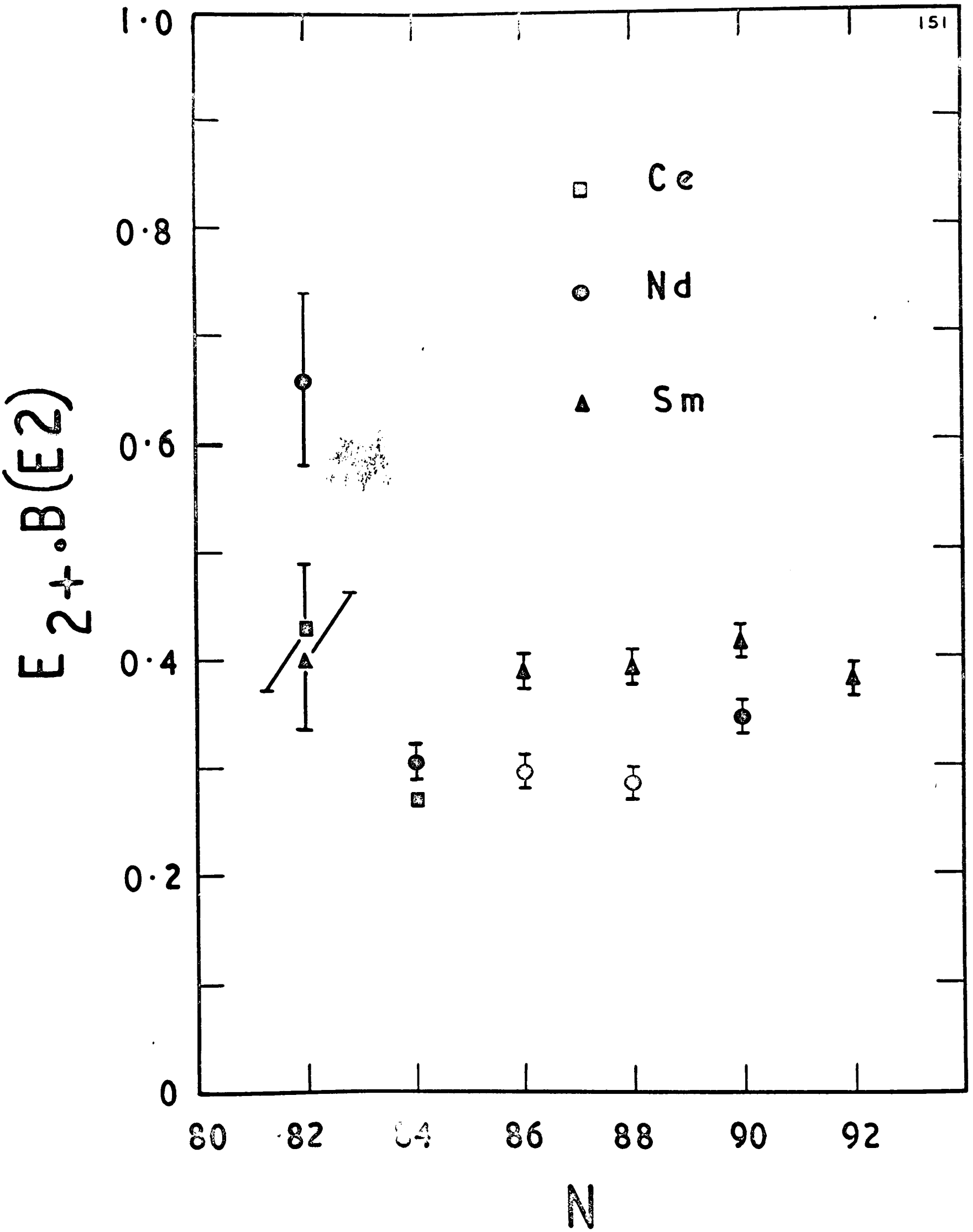


Fig. 5.3

has been interpreted as marking the onset of deformation (Duc 64; Tra 64). (A classical calculation by Pauling (Pau 65) also leads to the conclusion that prolate deformation begins at $N \geq 90$). Perhaps it should not be expected that the electric quadrupole transition strengths to the first excited state would reveal a change of shape; alternatively, it may be that no marked change of shape is taking place in this region. Certainly the quadrupole moments determined for Sm^{148} and Sm^{150} (Section 5.2) do not rule out the possibility that these nuclei are deformed.

5.1. 5. Summary. The pairing plus quadrupole force theory is seen to be moderately successful in predicting the B(E2) value to the first excited state of the single-closed shell nuclei studied here although a rather different effective charge for protons has been required in the N = 82 nuclei from that used in the N = 28 nuclei suggesting possibly somewhat more contribution from the core in the N = 82 nuclei. The theory seriously overestimates the B(E2) values in nuclei away from the single-closed shell in the mass 140-150 transitional region, however.

The pure configuration to the shell model is not very successful in predicting the B(E2) values for the N = 28 nuclei studied.

The product $E_{2+} \cdot B(E2)$ is remarkably constant throughout the transitional region, particularly for the Sm isotopes, and does not show a change for $N > 88$ where the systematics of two neutron separation energies have been interpreted as revealing the onset of deformation.

5.1. 6. The Nuclear Radius Parameter. The traditional formula for the Coulomb barrier energy presented in Section 2.1. assumes that the nucleus can be effectively represented as a uniformly charged sphere of radius $r_o A^{1/3}$. Because this assumption is an over-simplification it is not obvious what is a safe value of r_o to be used. However, the results of Figure 3.1 provide a measure of r_o appropriate for calculating the Coulomb barrier energy. If the energy in the centre-of-mass coordinate system E_{cm} at which the Rutherford Law for scattering at a centre-of-mass angle θ breaks down, shown in Figure 3.1, is interpreted as being the energy at which the two nuclear spheres just touch each other, i.e., when the closest distance of approach R_{min}

$$R_{min} = \frac{Z_1 Z_2 e^2}{2 E_{cm}} \left(1 + \operatorname{cosec} \frac{\theta}{2}\right) \qquad (5.4)$$

is equal to the sum of the projectile and target nucleus

radii then a value of r_o = 1.76 fm is obtained. Thus to get reasonably accurate estimates of the Coulomb barrier energy for planning Coulomb excitation experiments with heavy ions it is necessary to use a value of r_o considerably larger than that which gives the half-density radius of a nucleus as determined by electron scattering.

5.1. 7. Inelastic Scattering above Coulomb Barrier. The B(E2) value for Fe^{54} obtained at a bombarding energy of 40.7 MeV is significantly lower than the average result (quoted in Table 5.1) obtained at lower energies. Figure 3.1, which shows that 40.7 MeV is above the Coulomb barrier, also shows that the scattering at 90° becomes appreciably less relative to 30° scattering as the barrier energy is exceeded. Thus it appears that for some reason nuclear reactions deplete the heavy ion inelastic cross-section more than the elastic cross-section at energies just above the Coulomb barrier.

5.2. Electric Quadrupole Moments of Excited States.

Until just recently nothing was known about the quadrupole moments in even nuclei apart from rotational nuclei where the intrinsic deformation of the nucleus was inferred

from the B(E2) value to the first excited state. Because the ground state spin of the even nucleus is zero the ground state has no quadrupole moment and consequently the quadrupole moment of an excited state must be obtained to get some idea of the nuclear shape. However, the excited states are much too short-lived to be studied by atomic spectroscopic methods. These latter methods have been used to determine the ground state and a few isomeric state quadrupole moments in a number of odd nuclei (Ful 65). These quadrupole moments are very uncertain, however, because of the necessity of calculating the inhomogeneous electric field at the nucleus to interpret the experimental measurements. For odd nuclei near closed shells the quadrupole moments seem to have the sign implied by the single particle calculation; that is, for a closed shell plus a nucleon they are negative and for a closed shell plus a hole they are positive (Boh 53). Between closed shells, at least in the medium weight region, they are positive and large suggesting a collective origin and implying a prolate shape to the nucleus. However, the uncertainties of particle-surface coupling militate against obtaining very much detailed nuclear information from quadrupole moments of the odd nuclei.

The even nuclei away from closed shells have the advantage in that the low energy states are felt to be described completely in terms of collective parameters and consequently a determination of the excited state quadrupole moments should give information about some of these parameters. This section discusses the quadrupole moments of the first excited 2^+ states in Cd^{114}, Sm^{148} and Sm^{150} measured in the present work.

5.2.1. Quadrupole Moments: Cd^{114}, Sm^{148}, Sm^{150}. In order to get a feeling for the magnitude of the excited state quadrupole moments a comparison of the experimental moments of the first 2^+ state in Cd^{114}, Sm^{148} and Sm^{150} with the predictions of some simple models is made in Table 5.6. The

TABLE 5.6.

Nucleus	$B(E2)$ e^2b^2	Q_{exp} b	$Q_{s.p.}$ b	Q_{rot} b	Q_{phonon} b	Q_{RPA} b
Cd^{114}	0.52	-0.39(± 0.24)	-0.15	-0.66	0	-0.118
Sm^{148}	0.80	-0.78(± 0.38)	-0.14	-0.82	0	-0.082
Sm^{150}	1.38	-1.26(± 0.23)	-0.14	-1.06	0	-0.138

experimental value listed, Q_{exp} is the mean of the perturbation and Schrodinger equation results. The single-particle

estimate for a proton, Q_{sp}, is substantially smaller than the experimental values and suggests that the experimentally observed quadrupole moments arise from collective motion in the nuclei.

Nuclei with large permanent deformations have associated large quadrupole moments. If a deformation parameter β is defined as (Ald 56)

$$\beta = \frac{4}{3} \left(\frac{\pi}{5}\right)^{\frac{1}{2}} \frac{\Delta R}{R_o} \qquad (5.5)$$

where R_o is the mean nuclear radius and ΔR is the difference between the major and minor semiaxis of a spheroid then the intrinsic quadrupole moment of the spheroidal nucleus is related to β by

$$Q_o = \frac{3}{\sqrt{5\pi}} Z R_o^2 \beta \qquad (5.6)$$

In the symmetric rotator model the electric quadrupole transition strength is related to Q_o by (Ald 56)

$$B(E2; J_i \rightarrow J_f) = \frac{5}{16\pi} e^2 Q_o^2 \langle J_i \; 2 \; K \; 0 \mid J_f \; K \rangle^2 \qquad (5.7)$$

where $\langle J_i \; 2 \; K \; 0 \mid J_f \; K \rangle$ is a Clebsh-Gordon coefficient and K is the projection of the spin on a body-fixed quantization axis. The quadrupole moment measured in the present work

is the quadrupole moment of the nucleus in the state of spin 2, and in the rotational model the quadrupole moment Q_{rot} of a state of spin J is related to the intrinsic quadrupole moment by

$$Q_{rot} = Q_o \cdot \frac{3K^2 - J(J+1)}{(J+1)(2J+3)} \qquad (5.8)$$

Table 5.6 presents the predictions of the rotational model Q_{rot} determined from the B(E2) values listed which are averages of the results of the present work with those from references (Elb 60; McG 65; and deB 65). (For some purposes it is more convenient to know the reduced matrix elements for the transitions and static moments. The matrix elements are related to the B(E2) value and the quadrupole moment Q by

$$\langle 0 \| m(E2) \| 2 \rangle = \sqrt{B(E2;\ 0 \rightarrow 2)}$$

and

$$\langle 2 \| m(E2) \| 2 \rangle = \frac{5}{4\sqrt{\pi}} \left(\frac{7}{2}\right)^{\frac{1}{2}} Q = 1.32\ Q$$

The rotational model predicts that

$$M = \frac{\langle 2 \| m(E2) \| 2 \rangle}{\langle 0 \| m(E2) \| 2 \rangle} = -1.20 \quad \text{(prolate).} \qquad).$$

With the possible exception of Cd^{114} the experimental

quadrupole moments are of rotational size and the sign of Q implies that if the nuclei are deformed their structure is prolate. At first glance this seems to suggest that these nuclei may be permanently deformed but the low energy levels of these nuclei do not display other characteristics of a symmetric rotator, in particular the J(J+1) energy level spacing of a rotational band. (See Figures 4.6, 4.7, and 4.8). On the contrary Cd^{114} displays one of the best harmonic energy spectra known but the predictions of the quadrupole moment in the phonon model Q_{phonon} in which the excited states of an even nucleus are described as quadrupole surface vibrations of a spherical shape (Boh 52, 53) in the harmonic approximation result in zero quadrupole moment. Thus the experimental quadrupole moments are a real embarrassment to the phonon model; although one does not expect the phonon model to give detailed quantitative agreement with the properties of the nucleus it predicts qualitatively correctly the energy level and transition rate properties of nuclei such as Cd^{114} but is qualitatively in disagreement with the excited state quadrupole moments.

It appears then that a satisfactory nuclear collective model must provide for large excited state quadrupole moments (near rotational size) and approximately vibrational energy

spectra (or at least spectra which are considerably different from the prediction of the symmetric rotator). There are two ways in which this problem has been interpreted; the one has been to generalize the rotational model and the other to modify the vibrational model to include anharmonic effects.

5.2. 2. The Asymmetric Rotor Model. Davydov and Filippov (Dav 58) have generalized the rotational model to include asymmetric rotors. This model will not be treated in detail here but only those properties relevant to the present work will be mentioned.

In this model there are two parameters specifying the deformation, β (subsection 5.2. 1) and γ, an asymmetry parameter. For $\gamma = 0^{o}$, the model produces the properties of the symmetric rotor model. At the other extreme of $\gamma = 30^{o}$ the model generates a spectrum which has marked similarities with the vibrational model; there is a second 2^{+} state at twice the energy of the first 2^{+} state and there is a 4^{+} level somewhat higher. Ratios of reduced transition strengths can be determined solely as a function of γ, which can be determined experimentally from the ratio of the second excited 2^{+} state energy to the first excited 2^{+} state

energy $\frac{E_{2'}}{E_2}$. The quadrupole moment Q of the first excited 2^+ state can also be determined as a function of γ and Q_o,

$$Q = - Q_o \frac{6 \cos(3\gamma)}{7\sqrt{9-8 \sin^2(3\gamma)}} \qquad (5.9)$$

where Q_o is given by Equation 5.6. The relation connecting Q_o and $B(E2; 0^+ \rightarrow 2^+)$ is now however

$$Q_o = 4\sqrt{\frac{\pi}{5}} \sqrt{\frac{B(E2; 0^+ \rightarrow 2^+)}{b\,(2 \rightarrow 0)}} \qquad (5.10)$$

where

$$b(2 \rightarrow 0) = \frac{1}{8} \left[1 + \frac{3 - 2 \sin^2(3\gamma)}{\sqrt{9-8 \sin^2(3\gamma)}} \right] \qquad (5.11)$$

Table 5.7 lists the calculated quadrupole moments Q_{DF} using the values of γ obtained from the energy ratio $\frac{E_{2'}}{E_2}$. Also in-

TABLE 5.7.

Nucleus	$\frac{E_{2'}}{E_2}$	γ	Q_{DF}	a_1^2	Q_{anh}	Q_{exp}
Cd^{114}	2.17	26.7°	-0.33	0.9	$\pm$ 0.45	-0.39
Sm^{148}	2.67	23.5°	-0.63	0.85	$\pm$ 0.70	-0.78
Sm^{150}	3.14	21.8°	-0.90	0.86	$\pm$ 0.87	-1.26

cluded in the table are the quadrupole moments Q_{anh} calculated using a modified phonon model (subsection 5.2. 3).

Table 5.8 presents a comparison of two ratios of B(E2) values

$$R_1 = \frac{B(E2;\ 2^+ \rightarrow 2'^+)}{B(E2;\ 0^+ \rightarrow 2^+)} \qquad (5.12)$$

and

$$R_2 = \frac{B(E2;\ 0^+ \rightarrow 2'^+)}{B(E2;\ 2^+ \rightarrow 2'^+)} \qquad (5.13)$$

for the asymmetric rotor model (DF), the phonon model, and the modified phonon model (Anh. Ph); subsection 5.2. 3).

TABLE 5.8.

Nucleus	R_1			R_2			
	Exp't	D.F	Phonon	Exp't	D.F	Phonon	Anh.Ph.
Cd^{114}	0.29	0.224	0.4	0.057	0.10	0	0.391
Sm^{148}	0.22	0.146	0.4	0.42	0.40	0	0.766
Sm^{150}	0.23 or 0.30	0.107	0.4	0.006	0.65	0	0.676

(The ratio R_1 has been used as a parameter in the modified phonon model and is consequently not listed for this model.)

The asymmetric rotor model is moderately successful in

predicting Q and R_1. However, the model is not so successful in predicting R_2 and the energies of the 4^+ states; in Cd^{114} the 4^+ state should be much higher than the $2'^+$ state and in the Sm isotopes it should be nearly degenerate with the $2'^+$ level. A more serious objection in the case of Cd^{114} is the lack of a collective 0^+ level near the $2'^+$ state. This latter objection can probably be overcome by coupling vibrations to the rotations (Dav 60).

5.2. 3. Modified Phonon Model. The alternative approach to the permanently deformed model is to consider the effect of anharmonic terms in the phonon wavefunctions of the excited states. To retain the usefulness of the phonon model it should be possible to achieve quite large quadrupole moments with only a small admixture of these anharmonic terms.

To test phenomenologically whether this approach can reasonably predict satisfactory quadrupole moments the wavefunctions of the first and second 2^+ states $\psi(2)$ and $\psi(2')$ are written as linear combinations of one- and two - phonon states $|1\rangle$ and $|2\rangle$ (Gre 61; Tam 65)

$$\begin{aligned} (2) &= a_1 |1\rangle + a_2 |2\rangle \\ (2') &= -a_2 |1\rangle + a_1 |2\rangle \end{aligned} \qquad (5.14)$$

with $a_1^2 + a_2^2 = 1$. The ratios R1 and R_2 then become

$$R_1 = \frac{2\,(1 - 2a_1^2)^2}{5\,a_1^2} \tag{5.15}$$

and

$$R_2 = \frac{5\,(1 - a_1^2)}{2\,(2a_1^2 - 1)^2} \tag{5.16}$$

In analogy with deformed models an effective root-mean-square deformation $(\overline{B}^2)^{\frac{1}{2}}$ can be defined so that

$$B(E2;\ 0^+ \rightarrow 2^+) = \frac{9}{16\pi^2}\ e^2\ Z^2\ R_o^4\ \overline{B}^2 \tag{5.17}$$

The quadrupole moment of the 2^+ state is

$$Q = \frac{12}{5}\left[\frac{1}{7\pi}\right]^{\frac{1}{2}}\ a_1\ a_2\ Z\ R_o^2\ (\overline{B}^2)^{\frac{1}{2}} \tag{5.18}$$

and thus

$$Q = \frac{16}{5}\left[\frac{\pi}{7}\right]^{\frac{1}{2}}\ a_1\ a_2 \sqrt{B(E2;\ 0^+ \rightarrow 2^+)}\ \ b \tag{5.19}$$

where $B(E2;\ 0^+ \rightarrow 2^+)$ is in units of e^2b^2. Following Tamura and Udagawa (Tam 65) the values of a_1 are determined from the experimental ratio R_1 (Table 5.8) and are presented in Table 5.7 along with the associated quadrupole moments Q_{anh}. The sign of Q is undetermined because no explicit form of

the perturbing interaction which mixes one- and two-phonon states has been assumed. Table 5.7 shows that with a relatively small admixture of two-phonon state in the first 2^+ state fairly large quadrupole moments can be obtained, in agreement with the experimental results. However, the same amount of admixture over-enhances R_2 (Table 5.8).

A surprising feature is that approximately the same amount of two-phonon admixture into the one-phonon state accounts for both R_1 and Q in all three nuclei and yet the energy spectra of Sm^{148} and Sm^{150} is remarkably different from that of Cd^{114}. However it is probably too much to expect that such a simple approach in which the dominant perturbing interaction terms are not explicitly specified should yield quantitatively correctly all the low energy properties of these nuclei. In particular an interaction which couples states differing by two phonons may affect the energy positions without changing Q or R_1 very much and this interaction may be rather different for Cd^{114} and the Sm isotopes.

This discussion shows that it may still be possible to describe the low energy excited states as resulting from surface vibrations of an essentially spherical nucleus in spite of their large quadrupole moments. Some phenomenological models have been devised to mix in anharmonic terms and

in particular the Raz model (Raz 59; Mac 63a) can produce large quadrupole moments (of the same magnitude as the asymmetric rotor model) but apparently having the wrong sign (Mac 65a). (For the predictions of a large number of models with reference to the quadrupole moment of Cd^{114} see (Tam 65).) Unfortunately these models necessarily require a large number of free parameters diminishing their usefulness. Probably a better approach would be to explain the properties of these nuclei with a microscopic theory such as the pairing plus quadrupole force theory. The pairing plus quadrupole force theory as it has been formulated by Kisslinger and Sorenson in the random phase approximation is not much better than the phenomenological harmonic oscillator model in predicting the large quadrupole moments observed, as the column Q_{RPA} in Table 5.6 shows (Sor 65). The reason for the failure is apparent; the random phase approximation is tailored to produce an harmonic vibrational spectrum and is essentially a microscopic description of the quadrupole phonon model. Tamura and Udegawa (Tam 65) have employed a "higher" random phase approximation (Lan 64) with which they can produce the correct magnitude and sign of the Cd^{114} quadrupole moment. Although this appears encouraging unfortunately the validity of the random phase approximation as applied to nuclei is an open question

(Lan 64; Rho 65) and it may be premature to put too much faith in the higher order calculations.

On the other hand, if the proper explanation of these quadrupole moments requires that the nuclei be intrinsically deformed then this would conflict with the suggestion that deformation sets in for N > 88 (Duc 64; Tra 64; Pau 65).

5.3. Conclusions.

Several new experimental techniques have been developed and employed in this work to extend the usefulness of Coulomb excitation for learning about nuclear properties.

The method of magnetic analysis of heavy ions has been shown to provide a very accurate method of obtaining electric quadrupole transition strengths, particularly to high first excited states, and with the availability of better data on charge states and the advent of position-sensitive semiconductor counters it may serve as a very useful alternative to more traditional methods in some circumstances. In particular it was the only feasible method for measuring the very low excitation probabilities to the first excited states in Ti^{50}, Cr^{52} and Fe^{54}.

The usefulness of heavier ions such as O^{16} and S^{32} with high energies in obtaining more detailed knowledge of nuclear

properties, in particular excited state quadrupole moments, has been demonstrated but this experimental field is still in its infancy. With higher energy heavy ion accelerators and more accurate numerical methods of calculating Coulomb excitation amplitudes becoming available it should be possible to obtain transition and static moments up to quite high excited states in nuclei in regions of the periodic table which are at present poorly understood theoretically.

The electric quadrupole transition strengths B(E2) from the ground state to first excited state in Ti^{50}, Cr^{52}, Fe^{54}, $Ce^{140,142}$, $Nd^{142,143,144,146,148}$ and $Sm^{144,148,150}$ have been determined in the present work. These B(E2) values are not entirely satisfactorily explained within the present framework of the pairing plus quadrupole force theory especially when both types of nucleons are occupying the unfilled shells. As the nuclei become further from the closed shell the theory enhances the B(E2) values too much with a corresponding too rapid depression of the 2^+ state in the even nuclei. Another unfortunate feature of the theory is the rather large effective charges required for the proton and neutron in the mass 140 region to get some agreement between the predicted and theoretical B(E2) values. Some work is being done at present to include more shell model states

with a resultant lowering of the effective charges (Sor 65).

The B(E2) values of the N = 28 nuclei Ti^{50}, Cr^{52} and Fe^{54} do not agree very well with the predictions of the pure configuration approach to the shell model. In the mass - 140 region the B(E2) values do not reflect a change in deformation at N = 90 which is implied by changes in the two-neutron separation energy in this region. In fact the systematics of the B(E2) values show that the increase in the B(E2) value as the deformed region is approached mirrors remarkably closely the decrease in the 2^+ state energy.

The electric quadrupole moments of the first excited 2^+ states in Cd^{114}, Sm^{148} and Sm^{150} have been determined using the reorientation effect. All of them are fairly large suggesting a collective origin and are negative. In the course of analysing the results it was found that there is an unexplained discrepancy between the values obtained from perturbation theory and from the Schrodinger equation method.

The phonon model and the microscopic approach to the phonon model, the random phase approximation applied to the pairing plus quadrupole force theory, fail to predict these large quadrupole moments and require modifications which mix in certain anharmonic terms. These modifications to

date are made in a rather ad hoc manner and raise the whole question of the usefulness of the models in their present form.

The asymmetric rotor model achieves quite good agreement with experiment with a minimum of arbitrary parameters but it has been criticized on other grounds, one being that calculations using pairing forces suggest that permanently asymmetric nuclei are highly unlikely (Bar 65).

Certainly the hope is that a microscopic approach perhaps incorporating residual forces such as pairing forces which will explain the low energy properties of "spherical" nuclei will become available and will be tractable to calculation.

REFERENCES

Ada 60 B.M. Adams, D. Eccleshall, M.J.L. Yates, in Proc. Second Conf. on Reactions between Complex Nuclei; (1960), ed. A. Zucker et al. (John Wiley, New York, 1960, p. 95.

Ald 56 K. Alder, A. Bohr, T. Huus, B. Mottelson, A. Winther, Revs. Mod. Phys., 28, (1956), 432.

Ald 60 K. Alder and A. Winther, Mat. Fys. Medd. Dan. Vid. Selsk., 32, No.8. (1960).

Ald 62 K. Alder and A. Winther, Nuclear Physics, 37, (1962), 194.

Alm 62 E. Almqvist, C. Broude, M.A. Clark, J.A. Kuehner, A.E. Litherland, Can. J. Phys., 40, (1962), 954.

Bar 60 M. Baranger, Phys. Rev., 120, (1960), 957.

Bar 65 M. Baranger and K. Kumar, Nuclear Physics 62, (1965), 113.

Bay 64 B. Bayman, in Nuclear Structure and Electromagnatic Interactions. ed. N. MacDonald (Oliver and Boyd, Edinburgh, 1964), p. 19.

Bel 59 S.T. Belyaev, Mat. Fys. Medd. Dan. Vid. Selsk, 31, No.11, (1959).

Bel 62 J. Bellicard and P. Barreau, Nuclear Physics, 36, (1962), 476.

Bel 64 J. Bellicard, P. Barreau, D. Blum, Nuclear Physics, 60, (1964),319.

Bie 53 L.C. Biedenharn and M.E. Rose, Revs. Mod. Phys., 25, (1953), 729.

Bie 65 L.C. Biedenharn and P.J. Brussaard, Coulomb Excitation (Clarendon Press, Oxford, 1965).

Bir 59 M. Birk, G. Goldring, Y. Wolson. Phys. Rev. 116, (1959), 730.

Bje 63 J. Bjerregard, B. Elbeek, O. Hansen, P. Salling, Nuclear Physics, 44, (1963), 280.

Bla 61 J.L. Blankenship and C.J. Borkouski, I.R.E., Trans. N S 8 (1961), 17.

Bog 58 N.N. Bogolinbov, Nuovo Cimento, 7, (1958), 794.

Boh 52 A. Bohr, Mat. Fys. Medd. Dan. Vid. Selsk, 26, No. 14, (1952).

Boh 53 A. Bohr and B.R. Mottelson, Mat. Fys. Medd. Dan. Vid. Selsk., 27, No. 16, (1953).

Boh 58 A. Bohr, B.R. Mottelson, D. Pines, Phys. Rev., 110. (1958), 936.

Boo 65 W. Booth and I.S. Grant., Nuclear Physics, 63, (1965), 99.

Bre 56 G. Breit, R.L. Gluckstern, J.E. Russell, Phys. Rev., 103, (1956), 727.

Bru 63 P.J. Brussaard and L.C. Biedenharn, in Proc. Third Conf. on Reactions between Complex Nuclei (1963); ed. A. Ghiorso et al. (University of California Press, Berkeley, 1963), p. 311.

Byg 64 W.D. Bygrave, D. Eccleshall, M.J.L. Yates, Nuclear Physics., 53, (1964), 385.

Coh 61 A.V. Cohen, J.A. Cookson, J.L. Wankling, Nucl. Instr., 10, (1961), 84.

Coo 64 J.A. Cookson and J.L. Wankling, Nucl. Instr. 30, (1964), 99.

Dar 64 W. Darcey, unpublished thesis (Oxford, 1964).

Dar 65 W. Darcey and A. Jeans, private communication (1965).

Dav 58 A.S. Davydov and G.F. Filippov, Nuclear Physics, 8, (1958), 237.

Dav 60 A.S. Davydov and A.A. Chaban, Nuclear Physics., 20, (1960), 499.

deB 65 J. de Boer, R.G. Stokstad, G.D. Symons, A. Winther, Phys. Rev. Letts., 14, (1965), 564.

deS 63 A. de Shalit and I. Talmi, Nuclear Shell Theory, (Academic Press, New York, 1963).

Dou 63 A.C. Douglas, W. Bygrave, D. Eccleshall, M.J.L. Yates, in Proc. Third Conf. on Reactions between Complex Nuclei (1963)., ed. A. Ghiorso et al. (University of California Press, Berkeley, 1960) p. 274.

Dou 65 A.C. Douglas, private communication, to be published (1965).

Duc 64 H.E. Duckworth, R.C. Barber, B.G. Hogg, J.D. MacDougall, W. McLatchie, P. Van Rookhuyzen, in Comptes Rendus du Congres International de Physique Nucleaire, Paris 1964, ed. Mme. P. Gugenberger (Editions du Centre National de la Recherche Scientifique, 1965) Vol. II, p. 557.

Ecc 62 D. Eccleshall, B.M. Hinds, M.J.L. Yates, Nuclear Physics., 32, (1962), 190.

Eic 64 J. Eichler, Phys. Rev., 133, (1964), B 1162.

Elb 60 B. Elbek, M.C. Olesen, O. Skilbreid, Nuclear Physics, 19, (1960), 523.

Elb 64 B. Elbek, H.E. Gove, B. Herskind, Mat. Fys. Medd. Dan. Vid. Selsk., 34, No.9. (1964).

Fer 55 M. Ferentz and N. Rosensweig, Table of F Coefficients, Argonne National Laboratory Report, ANL-5324 (1955).

Ful 65 G.H. Fuller and V.W. Cohen, Nuclear Moments, Appendix I to Nuclear Data Sheets (1965).

Gol 61 G. Goldring and Z. Vager, Nuclear Physics, 26, (1961), 250.

Gol 65 G. Goldring and U. Smilansky, Phys. Lett, 16, (1965), 151.

Gre 61 D.P. Grechukhin, Nuclear Physics., 24, (1961), 576.

Gro 62 L. Gredsins, Phys. Lett., 2, (1962), 88.

Hax 49 O. Haxel, J.H.D. Jensen, H.E. Suess, Phys. Rev, 75, (1949), 1766.

Hea 57 R.L. Heath, Scintillation Spectrometry Gamma Ray Spectrum Catalogue, A.E.C. Research and Development Report IDO - 16408 (1957).

Hec 63 H.H. Heckman, E.L. Hubbard, W.G. Simon, Phys. Rev., 129, (1963), 1240.

Her 64 B. Herskind and Y. Yoshizawa, Nucl. Instr. 27, (1964), 104.

Hub 55 E.L. Hubbard and E.J. Lever, Phys. Rev. 98 (1955), 1814.

Ken 64 R.A. Kenefick and R.K. Sheline, Phys. Rev. 133, (1964), B 25.

Kis 60 L.S. Kisslinger and R.A. Sorenson. Mat. Fys. Medd. Dan. Vid. Selsk., 32, No.9. (1960).

Kis 63 L.S. Kisslinger and R.A. Sorensen, Revs. Mod. Phys. 35, (1963), 853.

Lam 64 A.M. Lane, Nuclear Theory, (W.A. Benjamin, New York, 1964).

Law 57 R.D. Lawson and J.L. Uretsky, Phys. Rev. 106, (1957), 1369.

Lem 60 I. Kh. Lemberg, in Proc. Second Conf. on Reactions between Complex Nuclei (1960), ed. A. Zucker et al. (John Wiley, New York, 1960), p. 112.

Lin 63 D.L. Lin and J.F. Marso, in Proc. Third Conf. on Reactions between Complex Nuclei (1963), ed. A. Ghiorso et al (University of California Press, Berkeley, 1963), p. 267.

Lit 63 A.E. Litherland, E. Almqvist, B.H. Andrews, C. Broude, J.A. Kuehner, Bull. Am. Phys. Soc., 8. (1963), 75.

Mac 63 N. MacDonald, private communication (1963).

Mac 63a N. MacDonald, Nuclear Physics, 48, (1963), 500.

Mac 64 N. MacDonald, Phys. Lett., 10, (1964), 334.

Mac 65 N. MacDonald and A.C. Douglas, prive communication (1965).

Mac 65a N. MacDonald, private communication (1965).

Mar 56 H. Margenau and G.M. Murphy, The Mathematics of Physics and Chemistry (Van Nostrand, 1956), p. 100.

May 48 M.G. Mayer, Phys. Rev. 74, (1948), 235.

May 49 M.G. Mayer, Phys. Rev. 75, (1949) 1969.

May 50 M.G. Mayer, Phys. Rev. 78, (1949) 16.

McC 64 J.D. McCullen, B.F. Bayman, L. Zamick, Phys. Rev. 134, (1964), B 515.

McG 65 F.K. McGowan, R.L. Robinson, P.H. Stelson, J.L.C. Ford, Nuclear Physics, 66 (1965), 97.

Nat 60 O. Nathan and V.I. Popov, Nuclear Physics, 21, (1960), 631.

Nat 65 O. Nathan and S.G. Nilsson, in Alpha-,Beta-, and Gamma-Ray Spectroscopy, ed. K. Siegbahn (North Holland, 1965), p. 601.

Ofe 59 S. Ofer and A. Schwarzschild, Phys. Rev. Lett. 3, (1959), 384.

Ofe 59a S. Ofer and A. Schwarzschild, Phys. Rev. 116 (1959), 725.

Pau 65. L. Pauling, Phys. Rev. Lett, 15, (1965), 868.

Por 61 D.I. Porat and K. Ramavataran, Proc. Phys. Soc. 77, (1961), 97; Proc. Phys. Soc. 78, (1961), 1135.

Ram 59 K. Ramavataran and D.I. Porat, Nucl. Instr. 4, (1959), 239.

Ras 59 B.J. Ras, Phys. Rev. 114, (1959), 1116.

Rei 65 P.W. Reich and J.H. Douglas, Nucl. Instr. 35, (1965), 67.

Rey 55 H.L. Reynolds, L.D. Wyly, A. Zucker, Phys. Rev. 98, (1955), 1825.

Rho 65 M. Rho, Nuclear Physics, 65, (1965), 497.

Ros 53 M.E. Rose, Phys. Rev., 91, (1953), 610.

Sha 58 R.D. Sharp and W.W. Buechner, Phys. Rev. 109, (1958), 1698.

She 60 R.K. Sheline, H.L. Nielson, A. Sperduto, Nuclear Physics, 16, (1960), 518.

Smi 65 U. Smilansky, Calculation of Coulomb Excitation Probabilities for Heavy Ions, Internal Report, Weizmann Institute of Science, Rehovoth, (1965), and private communication.

Sor 64 R.A. Sorenson, Phys. Rev., 133, (1964), 281.

Sor 65 R.A. Sorenson and R.A. Uher, private communication from R.A. Sorenson, (1965).

Ste 63 N.H. Steiger, in Proc. Third Conf. on Reactions between Complex Nuclei (1963), ed. A. Ghiorso et al. (University of California Press, Berkeley 1963), p. 407.

Ste 65 P.H. Stelson, W.T. Milner, J.L.C. Ford, F.K. McGowan, R.L. Robinson, Bull. Am. Phys. Soc.II, 10, (1965), 427.

Sun 55 A.W. Sunyar, Phys. Rev. 98, (1955), 653.

Tal 58 I. Talmi, in Proc. of the Rehovoth Conference on Nuclear Structure (North Holland, Amsterdam, 1958).

Tal 60 I. Talmi and I. Unna, Am. Rev. Nucl. Sci. 10, (1960), 353.

Tal 62 I. Talmi, Revs. Mod. Phys. 34, (1962), 704.

Tam 65 T. Tamura and T. Udagawa, Phys. Rev. Lett, 15, (1965), 765.

Tot 63 K.S. Toth and E. Newman, in Proc. Third Conf. on Reactions between Complex Nuclei (1963), ed. A. Ghiorso et al (University of California Press, Berkeley 1963), p. 114.

Tra 64 L.E.H. Trainor, in Comptes Rendus du Congres International de Physique Nucleaire, Paris, (1964) National de la Recherche Scientifique, 1965), Vol. II, p. 548.

Val 58 J.G. Valatin, Nuovo Cimento, 7, (1958), 843.

Vas 63 V.D. Vasil'ev, K.I. Erokhina, I. Kh. Lemberg, Izv. Akad. Nank. SSSR (ser fiz) 26, (1962), 999.

Wap 59 A.H. Wapstra, G.J. Nijgh, R. Van Lieshout, Nuclear Spectroscopy Tables (North-Holland, Amsterdam, 1959), p. 66.

Yat 61 M.J.L. Yates, Angular Distribution Coefficients for Deexcitation Gamma Rays Following Coulomb Excitation by Particles Scattered in an assigned Orbit (1961), private communication.

Yat 65 M.J.L. Yates, in Alpha-,Beta-, and Gamma-Ray Spectroscopy, ed. K. Siegbahn (North-Holland, Amsterdam, 1965), p. 1691.

Yos 64 Y. Yoshizawa, B. Elbek, B. Herskind, R.J. Keddy, M.C. Olesen, Bull. Am. Phys. Soc. 9, (1964), 497.

Zai 64 C.S. Zaidins, (1964), private communication.